

# A First Order Model of a Variable Camber Wing for a Civil Passenger Aircraft

Tristan Martindale

A dissertation submitted to the Faculty of Engineering and the Built Environment,  
University of the Witwatersrand, Johannesburg, in fulfilment of the requirements  
for the degree of Master of Science in Engineering.

Johannesburg, December 2011

## Declaration

I declare that this dissertation is my own, unaided work, except where otherwise acknowledged. It is being submitted for the degree of Master of Science in Engineering in the University of the Witwatersrand, Johannesburg. It has not been submitted before for any degree or examination at any other university.

Signed this \_\_\_\_ day of \_\_\_\_\_ 20\_\_\_\_

---

Tristan Martindale.

# Abstract

This work presents the development, implementation and analysis of a first order model of a variable camber wing. An aerodynamic model of a homogeneous wing employing variable camber actuation was developed based on the vortex lattice method and was applied to the approach and landing phases (low speed, steady state, high angle of attack) of a civil transport aircraft. The aerodynamic model was shown to predict the lift curve well up to the stall angle of attack of  $18^\circ$ . A novel way of varying the camber across the wing span was presented which uses a parameter defining the NACA 5 series camber line to provide a means of smoothly changing the camber at a specific span location combined with a linear variation of the parameter along the span. This provided a model of a homogeneous wing capable of smooth continuous changes in shape. The lift distribution along the span of the variable camber wing clearly demonstrated smoothness with none of the discontinuities caused by conventional ailerons. The camber control effectiveness was shown to be 44% less than that of conventional ailerons which is partly attributed to the linear variation in camber along the span. It was shown that the variable camber has even less coupling with the longitudinal aerodynamics than do conventional ailerons and that the coupling with both yaw and side force appears smaller. A strip theory model was developed based on the typical section in aeroelasticity with two degrees of freedom: heave and twist. It was assumed that the camber actuation mechanism holds the wing perfectly rigid once the desired camber is reached. The discrete model was verified against a continuous cantilever beam. The discrete model of the Citation V wing was found to have natural bending and torsion frequencies of approximately  $8\text{ Hz}$  and  $5\text{ Hz}$  respectively which lie in the expected range for light civil passenger jets. The stability of the system in response to aircraft angle of attack and variable camber inputs was evaluated both with and without the presence of aerodynamic damping in the model. The stability of the system was found to depend on the amount of aerodynamic damping present.

*To my dearest wife*

***Janita***

*without whom this would not have been possible.*

## Acknowledgements

I would like to thank my supervisors: Dr Craig Law and Dr Jimoh Pedro for their help and guidance.

I would like to thank Shawn Sampson, the senior publications administrator at Cessna for providing the Citation 560 flight and operating manuals.

I would like to thank my loving wife, Janita, for sharing me with my books for so long and for giving up so much so that I might find the time to complete this work.

## Published Work

Aspects of this thesis have been published in the following reference:

- T. Martindale, C. Law and J. Pedro, “A Vortex Lattice Aerodynamic Model for Active Camber Controlled Wings,” in *“Proceedings of the 7th South African Conference on Computational and Applied Mechanics”*, Pretoria, January 2010

# Contents

<b>Declaration</b>	<b>i</b>
<b>Abstract</b>	<b>ii</b>
<b>Acknowledgements</b>	<b>iv</b>
<b>Published Work</b>	<b>v</b>
<b>Contents</b>	<b>vi</b>
<b>List of Figures</b>	<b>x</b>
<b>List of Tables</b>	<b>xiv</b>
<b>List of Symbols</b>	<b>xvi</b>
<b>List of Acronyms</b>	<b>xxi</b>
<b>1 Introduction</b>	<b>1</b>
1.1 Motivation . . . . .	6
1.2 Objectives . . . . .	7
1.3 Dissertation Layout . . . . .	7
<b>2 Methodology</b>	<b>9</b>

2.1	Modelling . . . . .	9
2.2	Verification and Validation . . . . .	12
2.3	Application . . . . .	14
<b>3</b>	<b>Mathematical Model</b>	<b>16</b>
3.1	System Definitions . . . . .	16
3.2	Aerodynamics . . . . .	18
3.2.1	Vortex Lattice Method . . . . .	20
3.2.2	Airfoil Camber Actuation . . . . .	21
3.2.3	Spanwise Camber Variation . . . . .	26
3.3	Wing Structure . . . . .	27
3.4	State Space . . . . .	31
<b>4</b>	<b>Verification and Validation</b>	<b>33</b>
4.1	Aerodynamic Model . . . . .	33
4.1.1	Lift Distribution . . . . .	34
4.1.2	Discretization . . . . .	36
4.1.3	Longitudinal Aerodynamics . . . . .	37
4.1.4	Lateral Aerodynamics . . . . .	40
4.2	Structural Model . . . . .	42
4.2.1	Reference Cantilever Beam . . . . .	43
4.2.2	Static Deflections and Initial Conditions . . . . .	45
4.2.3	Mode Shape and Natural Frequency . . . . .	49
4.2.4	Free Response . . . . .	51



<b>5</b>	<b>Application</b>	<b>55</b>
5.1	Wing Structural Model . . . . .	55
5.1.1	Static Deflections and Initial Conditions . . . . .	55
5.1.2	Mode Shape and Natural Frequency . . . . .	56
5.1.3	Free Response . . . . .	58
5.2	Variable Camber Aerodynamics . . . . .	61
5.2.1	Lift Distribution with Camber Deflection . . . . .	62
5.2.2	Roll Authority . . . . .	63
5.2.3	Aircraft Aerodynamics . . . . .	65
5.3	Aeroelastic Wing . . . . .	68
<b>6</b>	<b>Conclusions</b>	<b>74</b>
6.1	Mathematical Model . . . . .	75
6.2	Verification and Validation . . . . .	76
6.3	Application . . . . .	78
6.4	Conclusions . . . . .	80
6.5	Recommendations for Future Work . . . . .	82
	<b>REFERENCES</b>	<b>84</b>
<b>A</b>	<b>Three View</b>	<b>87</b>
<b>B</b>	<b>Strip Properties</b>	<b>89</b>
<b>C</b>	<b>Aircraft Geometry</b>	<b>93</b>

<b>D</b>	<b>Weight and Balance</b>	<b>95</b>
<b>E</b>	<b>Aerodynamics</b>	<b>97</b>
E.1	Longitudinal Aerodynamics . . . . .	97
E.2	Lateral Aerodynamics . . . . .	99
<b>F</b>	<b>The RCAM Problem</b>	<b>101</b>
<b>G</b>	<b>Longitudinal Results</b>	<b>103</b>

## List of Figures

3.1	Discretization of the wing span into $n$ chordwise strips . . . . .	17
3.2	Definition of the wing and body coordinate systems . . . . .	17
3.3	Numbering scheme used by Tornado to reference individual wing panels	20
3.4	Camber line and cross-section profile of a NACA23012 airfoil with maximum thickness of 12% and maximum camber at $p = 15\%$ of $c$ .	22
3.5	Effect of $p$ on the camber line shape with $m$ and $k$ fixed at the values shown in Table 3.2 . . . . .	23
3.6	Effect of $m$ on the camber line shape with $p$ and $k$ fixed at the values shown in Table 3.2 . . . . .	24
3.7	Effect of $k$ on the camber line shape with $p$ and $m$ fixed at the values shown in Table 3.2 . . . . .	25
3.8	Linear variation of camber actuation along the wing span . . . . .	27
3.9	Model of the typical section in aeroelasticity . . . . .	28
4.1	Lift distribution along the wing span, calculated at the steady, trimmed flight state of $h = 1000\text{ m}$ , $V = 58\text{ m/s}$ , $\alpha = 10.39^\circ$ . . . . .	35
4.2	Error between the lift coefficient predicted by the discrete model in Tornado and the manufacturer's data; plotted as separate curves for variation in the number of panels along the chord and the span . . .	36
4.3	Wing lift coefficient as a function of $\alpha$ for the flexible model imple- mented in Tornado compared to both the manufacturer's data and published wind tunnel test results for the NACA23012 airfoil . . . .	38

4.4	Wing pitching moment coefficient as a function of $\alpha$ for the flexible model implemented in Tornado compared to both the manufacturer's data and published wind tunnel test results for the NACA23012 airfoil	39
4.5	Deflection of a cantilever beam in bending with a point force $F$ applied to the free end . . . . .	44
4.6	Twist of a cantilever beam in torsion with a moment $M$ applied to the free end . . . . .	45
4.7	Static deflection of the discrete cantilever beam compared to a continuous cantilever beam when a point force of 1000 $N$ is applied to the free end . . . . .	46
4.8	Static twist of the discrete cantilever beam compared to a continuous cantilever beam when a moment of 1000 $Nm$ is applied to the free end	48
4.9	First four bending mode shapes and natural frequencies of the reference uniform cantilever beam model (Equations (3.12) and (4.4)) parameterized as per Table 4.4 . . . . .	50
4.10	First four torsion mode shapes and natural frequencies of the reference uniform cantilever beam model (Equations (4.6) and (4.7)) parameterized as per Table 4.4 . . . . .	51
4.11	Comparison between the bending responses of the reference and discrete cantilever beam models (with and without the presence of cross-coupling terms in the mass matrix) in response to an initial bending deflection . . . . .	52
4.12	Comparison between the twist responses of the reference and discrete cantilever beam models (with and without the presence of cross-coupling terms in the mass matrix) in response to an initial twist deflection . . . . .	53
5.1	Static deflection of the half wing compared to the discrete uniform cantilever beam when a force of 1000 $N$ is applied to the free end . .	56
5.2	Static twist of the half wing compared to the discrete uniform cantilever beam when a moment of 1000 $Nm$ is applied to the free end .	57

5.3	Comparison between the bending responses and natural frequencies of the wing and discrete cantilever beam models in response to an initial bending deflection . . . . .	59
5.4	Comparison between the twist responses and natural frequencies of the wing and discrete cantilever beam models in response to an initial twist deflection . . . . .	60
5.5	Comparison between the effects of aileron deflection and variable camber actuation on the lift distribution along the wing span, calculated at the steady flight state of $h = 1000\text{ m}$ , $V = 58\text{ m/s}$ , $\alpha = 10.39^\circ$ . . . . .	62
5.6	Comparison between the effects of aileron deflection and variable camber actuation on the aircraft rolling moment coefficient $C_\ell$ . . . . .	64
5.7	Comparison between the effects of aileron deflection and variable camber actuation on the aircraft yawing moment coefficient $C_n$ . . . . .	66
5.8	Comparison between the effects of aileron deflection and variable camber actuation on the aircraft side force coefficient $C_Y$ . . . . .	67
5.9	Phase space plot of the undamped frequency response of the aeroelastic model to an external stepped pitch input ( $\alpha$ ), clearly showing the unstable pitch and plunge frequency peaks at 6 Hz and 31 Hz . . . . .	69
5.10	Phase space plot of the aerodynamically damped frequency response of the aeroelastic model to an external stepped pitch input ( $\alpha$ ), clearly showing the stable pitch and plunge frequency peak at 59 Hz . . . . .	70
5.11	Phase space plot of the undamped frequency response of the aeroelastic model to a stepped control input ( $\delta_c$ ), clearly showing the unstable pitch and plunge frequency peaks at 6 Hz and 31 Hz . . . . .	71
5.12	Phase space plot of the aerodynamically damped frequency response of the aeroelastic model to a stepped control input ( $\delta_c$ ), clearly showing the stable pitch and plunge frequency peak at 60 Hz . . . . .	72
A.1	Side view of the Cessna Citation V geometry showing important dimensions and reference points (indicated by dotted circles) . . . . .	87

A.2	Top view of Cessna Citation V geometry showing important dimensions and reference points (indicated by dotted circles) . . . . .	88
B.1	Geometry of an airfoil cross section showing the elastic axis and relevant dimensions . . . . .	89
D.1	Side view of the Cessna Citation V showing dimensions used for weight and balance calculations . . . . .	95
E.1	Aircraft geometry (side view) used for calculation of the aircraft longitudinal aerodynamic coefficients . . . . .	97
E.2	Aircraft geometry (top view) used for calculation of the aircraft lateral aerodynamic coefficients . . . . .	99
E.3	Aircraft geometry (front view) used for calculation of the aircraft lateral aerodynamic coefficients . . . . .	99
F.1	RCAM approach and landing trajectory . . . . .	101
G.1	Comparison between the effects of aileron deflection and variable camber actuation on the aircraft lift coefficient $C_L$ . . . . .	103
G.2	Comparison between the effects of aileron deflection and variable camber actuation on the aircraft induced drag coefficient $C_{D_i}$ . . . . .	104
G.3	Comparison between the effects of aileron deflection and variable camber actuation on the aircraft pitching moment coefficient $C_m$ . . . . .	105

## List of Tables

3.1	First order dimensional derivatives . . . . .	19
3.2	Parameters defining the NACA 23012 airfoil . . . . .	22
4.1	Definition of the flight state for verification and validation . . . . .	34
4.2	Longitudinal aerodynamic results . . . . .	40
4.3	Lateral aerodynamic results . . . . .	41
4.4	Parameters defining the cantilever beam . . . . .	43
5.1	Comparison of mass and stiffness parameters . . . . .	58
5.2	Effect of aileron and camber deflection on the airfoil maximum camber	61
5.3	Lift curve slope for each wing strip . . . . .	68
5.4	Parameters calculated using the Citation V wing . . . . .	70
B.1	Geometric properties for each wing strip . . . . .	91
B.2	Inertial properties for each wing strip . . . . .	92
C.1	Parameters defining the wing geometry . . . . .	93
C.2	Parameters defining the horizontal tail geometry . . . . .	93
C.3	Parameters defining the vertical tail geometry . . . . .	94
D.1	Aircraft weight and balance parameters . . . . .	96

F.1	Definition of the RCAM trajectory segments . . . . .	102
-----	--	-----



## List of Symbols

$a$	distance from quarter chord to elastic axis
$A$	cross-sectional area
$\mathbf{A}$	system matrix
$A_n$	constant in cantilever beam bending free response equation
$\mathbf{B}$	control matrix
$B_n$	constant in cantilever beam bending free response equation
$c$	chord
$\mathbf{C}$	output matrix
$\bar{c}$	mean aerodynamic chord
$\mathbf{C}_{aero}$	aerodynamic damping matrix
$C_D$	drag coefficient
$C_L$	lift coefficient
$C_\ell$	rolling moment coefficient
$C_m$	pitching moment coefficient
$C_n$	yawing moment coefficient / constant in cantilever beam torsion free response equation
$C_Y$	side force coefficient
$D$	drag

$D_n$	constant in cantilever beam torsion free response equation
$E$	Young's Modulus
$\mathbf{f}_a$	aerodynamic force vector
$F$	force
$g$	gravitational acceleration
$G$	Shear Modulus
$h$	altitude
$H$	normalized torsion mode shape of the cantilever beam
$i$	index
$I$	area moment of inertia
$I_{yy}$	mass moment of inertia about the elastic axis
$I_\theta$	generalized mass for torsional mode
$j$	index
$J$	polar moment of inertia
$k$	constant defining wing camber / constant relating induced drag coefficient to lift coefficient
$k_{left}$	constant defining left wing camber
$k_{right}$	constant defining right wing camber
$k_w$	airfoil linear structural stiffness parallel to the $z_W$ axis
$k_\theta$	airfoil torsional structural stiffness about the elastic axis
$\mathbf{K}_{aero}$	aerodynamic stiffness matrix
$\ell$	beam length / rolling moment
$L$	lift / Lagrangian

$m$	aircraft mass / mass / pitching moment / constant defining wing camber
$\mathbf{m}_a$	aerodynamic moment vector
$M$	moment / generalized mass for bending mode
$M_{aa}$	moment about the aerodynamic axis (aerodynamic center)
$M_{ea}$	moment about the elastic axis
$\hat{\mathbf{M}}$	inverse generalized mass matrix
$n$	yawing moment
$p$	roll rate / atmospheric pressure / constant defining position of maximum airfoil thickness
$q$	dynamic pressure / pitch rate / generalized coordinate
$Q$	generalized force
$r$	yaw rate / distance from elastic axis to collocation point
$s$	wing semi-span
$S$	total static mass moment about the elastic axis
$S_{ea}$	static mass moment per unit span about the elastic axis
$\mathbf{S}_j$	slope vector of partition $n$
$S_w$	wing reference area
$t$	time / thickness
$T$	kinetic energy
$u$	external input / speed in direction of $x_B$
$U$	strain energy
$\mathbf{v}$	translational velocity vector
$V$	true air speed

$w$	deflection of cantilever beam parallel to the $z_W$ axis
$W$	normalized bending mode shape of the cantilever beam
$\delta W$	work done by external aerodynamic forces and moments
$x$	x position
$\mathbf{x}$	state vector
$y$	y position
$Y$	side force
$z$	z position
$\alpha$	angle of attack
$\beta$	angle of side slip
$\gamma$	constant defining torsion mode shapes of the cantilever beam
$\delta_a$	aileron deflection
$\delta_c$	camber deflection
$\delta_e$	elevator deflection
$\delta_k$	constant defining wing camber as a function of semi-span position
$\delta_r$	rudder deflection
$\Delta$	variable used to modify airfoil camber line
$\zeta$	constant defining bending mode shapes of the cantilever beam
$\hat{\theta}$	wing strip local angle of rotation about the elastic axis
$\kappa$	constant defining bending mode shapes of the cantilever beam
$\rho$	atmospheric density / density of material

$\sigma$	standard deviation
$\omega$	aircraft angular velocity vector
$\omega_n$	natural frequency

## List of Acronyms

**AAW** active aeroelastic wing

**AC** aerodynamic centre

**AFW** active flexible wing

**AoA** angle of attack

**APO** adaptive performance optimization

**CFD** computational fluid dynamics

**CG** centre of gravity

**EA** elastic axis

**FAA** Federal Aviation Administration

**FEM** finite element methods

**GARTEUR** Group for Aeronautical Research and Technology in Europe

**MAC** mean aerodynamic chord

**MAW** mission adaptive wing

**MACW** mission adaptive compliant wing

**MOI** moment of inertia

**NACA** National Advisory Committee for Aeronautics

**NASA** National Aeronautics and Space Administration

**RCAM** research civil aircraft model

**UCAV** unmanned combat aerial vehicle

**VLM** vortex lattice method

# 1 Introduction

The concept of morphing wings was originally introduced by the Wright Brothers on the first aircraft that ever flew; the Wright Flyer. The Wright Flyer used mechanical linkages which were controlled by the pilot to change the shape of the left and right wings, thereby changing the lift distribution and providing directional control authority. This system was very limited because the pilot was essentially the whole control system. Measurement and feedback of the aircraft state was limited by human perception and response time. Actuation of the mechanical controls to change the shape of the wing was limited by the strength of the human pilot and the design of the mechanical linkage. Hetrick et al., (2007) point out that although morphing structures are usually termed “flexible”, the flexibility is controlled and is of no use if the shape cannot be rigidly maintained when it reaches its desired position.

The Wright Brothers did not understand many of the fundamental aerodynamic and flight dynamic concepts which are taken for granted today (Culick, 2001). The most important concepts they did not understand were the effect of the location of the neutral point and the existence of the three primary lateral modes: roll subsidence, spiral and Dutch roll. Unlike most of their predecessors and contemporaries who focused on designing statically stable aircraft, the Wrights were primarily concerned with maneuverability and control even to the point where they favoured an unstable aircraft which they could control over a stable aircraft which they could not. In order to simplify the pilots workload, the rudder and warp controls were connected and the Wrights flew the aircraft with coupled roll and yaw control until September 1905. One of the significant problems faced by the Wrights was the stalling of the inner wing in a turn due to its slower speed and higher angle of attack. After many crashes caused by this phenomenon, they finally realised towards the end of 1905 that the response to the lateral control was so slow that most of the time they could not recover to straight and level flight. Once they had realised this, they corrected it by lowering the nose in a turn to maintain their speed but it demonstrates the lack of roll authority available to them.

It is due to the initial failures of flexible wings that ailerons have become the conventional control surfaces with which roll authority is achieved. Ailerons are hinged portions of the wing trailing edge which, when deflected in opposite directions on the left and right wings, cause a lift differential and hence a resultant rolling moment about the aircraft's centre of gravity. Flexibility of the wing is undesirable because it causes adverse aeroelastic effects. However, aircraft designers are looking for a way to use this flexibility to their advantage. There has been a large amount of work done in the field of aeroelasticity, with the general aim of minimizing and avoiding the undesirable effects of flexibility in an aircraft structure (Mukhopadhyay, 2003). Static aeroelastic effects such as wing twisting, and dynamic effects such as flutter are well understood and control systems have been designed to compensate for these phenomena.

Modern conventional wing design yields a wing and control surfaces which are optimized for a single flight phase (usually cruise). Being able to optimize wing shape in flight and thereby decrease drag and increase fuel efficiency was the primary motivation behind the development of morphing wing concepts by the US Air Force and National Aeronautics and Space Administration (NASA) in the 1980s (Powers et al., 1992). Design studies were carried out to develop a smooth, variable camber, supercritical wing and resulted in the mission adaptive wing (MAW) which was tested on a F-111 aircraft in the mid 1980s. "A MAW is defined as a wing having the ability to actively modify airfoil camber, spanwise camber distribution, and wing sweep in flight, while maintaining a smooth and continuous airfoil surface" (Gilbert, 1981). The MAW used fully enclosed leading and trailing edge variable camber surfaces and an active control system to provide high levels of aerodynamic efficiency over a range of subsonic, transonic and supersonic flight conditions. The MAW concept could provide optimization of lift to drag ratio during all flight phases, integrated aileron action, spanwise control of the aerodynamic centre in order to minimize manoeuvre loads, an increase in lift without changing the angle of attack and high frequency actuation of the shape change allowing gust load alleviation. The MAW leading edge had a range of motion between  $5^\circ$  up and  $30^\circ$  down, the middle section of the airfoil was rigid and the trailing edge could move between  $7.5^\circ$  up and  $25^\circ$  down. In addition to this, the wing could twist  $3.281^\circ/m$  of span and a further  $5^\circ$  of motion was reserved for roll control at the trailing edge. Double curvature shapes could be produced and straight line twist deflections were found to be adequate. Unfortunately the rigid mechanical links and fibre glass wing panels used to implement the morphing wing were complex and heavy which meant that very little was gained over conventional wing design techniques.



According to Kota et al., (2006), when the results from the MAW program became available, German researchers affiliated with Airbus delved into flexible wing technology but this time with a view to applying it to transport aircraft. Unfortunately, they too were thwarted by the structural mass required to implement morphing wing concepts. Martins and Catalano (2003) published a theoretical study investigating the use of a variable camber wing for drag optimization of transport aircraft. They performed an optimization exercise based upon optimizing the aircraft range by reducing the viscous drag. The wing model consisted of an idealized model of two-dimensional airfoil aerodynamics where the airfoil was made up of rigid leading and trailing edges joined to two flexible sections which in turn were joined by a load carrying rigid section. Their results were based on numerical simulations only and predicted that actuating the leading and trailing edge together could increase the range by up to 24.6% as opposed to actuating only the trailing edge which resulted in a predicted range increase of 7.03%.

The active aeroelastic wing (AAW) flight research program run by NASA and Boeing began in 1996 and concluded in 2005 (NASA-DFRC, M Curry (ed.)). AAW technology integrated aerodynamics, active controls and structural aeroelastic behaviour to optimize wing and aircraft performance. According to Pendleton et al., (2000), AAW technology could be applied to high performance aircraft operating in a broad range of subsonic, transonic and supersonic conditions. The program replaced the wings of the F/A-18 fighter aircraft with the more flexible pre-production wings. The aim was to attempt to use leading and trailing edge control surfaces to warp the more flexible wing and achieve control in a similar manner to the original Wright Flyer. It was estimated that as much as a 25% reduction in the weight of the wing was achievable (Wilson, 2002). The active flexible wing (AFW) program undertaken by Boeing, the U.S. Air force and NASA demonstrated successful rapid roll manoeuvring utilizing a variable camber concept.

The practical application of configuration optimization in real time was explored by Gilyard et al., (1999) at the NASA Dryden Flight Research Centre as part of the adaptive performance optimization (APO) program. They conducted flight tests using an L-1011 transport aircraft and demonstrated the capability to determine the minimum drag configuration in real time. The APO program did not directly modify the aircraft wing but instead aimed to optimize the configuration of existing variable geometry devices (inboard and outboard ailerons, flaps, horizontal stabilizer and elevator) in order to minimize the total aircraft drag. The drag-minimization algorithm they devised uses optimal control theory and feedback from in-flight measurements of the aircraft motion and air data information to calculate the drag and

modify the geometry to achieve performance improvements. Gilyard et al., (1999) showed approximately a 1% reduction in aircraft drag when the real-time optimization algorithm was employed. They also concluded that, when using existing control surfaces to effect changes in camber, the outboard aileron represents only a small portion of the control potential that the wing trailing edge may have.

FlexSys have designed a “distributed compliant mechanism” capable of morphing a load bearing structure to different shapes or positions (Kota et al., 2006). Two important characteristics of this mechanism are that it is capable of maintaining maximum stiffness to withstand external pressure and optimal “compliance” in order to achieve controlled elastic deflection. Further research is being targeted at minimizing the force required to morph the surfaces throughout the flight envelope. The FlexSys mission adaptive compliant wing (MACW) has flexible leading and trailing edges while the middle section of the airfoil is rigid. The variable camber trailing edge occurs from 70% of the chord and is driven by two embedded electric servo motors. The trailing edge is capable of moving  $\pm 10^\circ$  at rates up to  $30^\circ/s$  while carrying an aerodynamic load. The morphed trailing edge maintains a balanced pressure distribution along the whole airfoil upper surface while eliminating suction peaks around the leading edge and preventing abrupt changes in surface slope at the entry to the pressure recovery region. The structural design of a variable camber trailing edge for a medium range aircraft dictates weight and critical flutter speed restrictions which are comparable to conventional flap systems.

MACW prototypes have been manufactured using aircraft grade aluminium and research is under way to use fully composite structures instead which would provide significant weight reductions as well as increasing strength and deflection range (Hetrick et al., 2007). FlexSys have developed and successfully applied adaptive structure design algorithms modelling aerodynamic loads, actuator forces and displacements, morphing shape error, system weight, buckling forces and material fatigue to a natural laminar flow airfoil. The MACW underwent 27 hours of flight testing in 2006 during which the model was successfully demonstrated at full scale dynamic pressure and Mach and reduced scale Reynolds number. Flight test results predict 33% less actuation force and 17% less peak actuation power compared to conventional flaps during a maximum g pull-up manoeuvre. FlexSys have also achieved a linearly varying change in camber along the wing span and have used simulation to prove that the structure can safely withstand aerodynamic loading, wing flex, and flap twist without exceeding material strain or fatigue limits.

Gern et al., (2002) presented a model used to compare roll performance and actuation power requirements of a morphing wing to a conventional wing with trailing

edge flaps and ailerons. The overall goal of the program was to determine the minimum control energy required to increase the manoeuvrability and performance of a flapless unmanned combat aerial vehicle. Gern et al., (2002) used a linearised compressible (via the Prandtl-Glauert compressibility correction) vortex lattice method to calculate aerodynamic loads and the work done by aerodynamic forces. The structural and aerodynamic models were validated using MSC/NASTRAN. In order to compare the results with normal ailerons they calibrated the morphing wing to produce the same rolling moment at the same actuation rate ( $90^\circ/s$  for a high performance fighter). Their results predicted that higher roll performance as well as the elimination of roll reversal can be achieved by twisting the outboard section of the wing. Simply changing the camber of the wing yielded a lower speed for roll reversal than a conventional aileron due to out of plane bending causing an increased washout at the wing tip. The amount of actuation power required was found to be heavily dependent on the dynamic pressure with the amount of power required to morph the wing decreasing as the dynamic pressure increases. This is due to the large structural deformations required to create sufficient rolling moment at low dynamic pressures. Their actuation scheme used 48 actuators distributed across the wing surface and they hypothesised that such a scheme would provide sufficient robustness and redundancy to account for actuator failures without the need for independent backup systems for each actuator as would be required for conventional systems. Gern et al., (2002) suggested that optimal performance may be obtained through the use of complex flight control laws which blend twist and camber actuation according to the flight conditions.

Johnston et al., (2003) presented a theoretical analysis of the energy requirements of morphing aircraft using aerodynamic and strain energy functions applied to adaptive wing shapes. They specified an adaptive camber line by appending a term modifying the trailing edge of a NACA 4 digit airfoil and allowing the airfoil to achieve commanded changes in lift and pitching moment coefficients independent of angle of attack. Their results predicted that morphing aircraft have the capability to outperform conventional aircraft in terms of required flight control energy.

Patel et al., (2005) applied Prandtl-Glauert lifting line theory in a vortex lattice method to calculate the lift, drag and pitching moments of a homogeneous morphing wing. In order to control the wing they implemented an input/output mapping of the coupled twisting sections, i.e. they utilized sensors to map the effect of the twist of one section of their wing on all the other sections. The input/output mapping is a static technique of predicting the wing shape when a specific control actuation is applied. Such a technique does not account for the dynamics of a real flight situation

where the aerodynamic forces change with the wing shape. Patel et al., (2005) used magnetic sensors to generate their input/output mappings in a wind tunnel. Their viability for real-time sensing and control was not established.

In order to investigate the behaviour of the overall system a set of representative test flight states are required. Having chosen a suitable test aircraft, it is appropriate to choose a set of test cases that have been applied to existing aircraft design. In 1997 the Group for Aeronautical Research and Technology in Europe (GARTEUR) published results from action group FM(AG08) which described the various control system design techniques currently in use in industry as applied to the design and optimization of the control algorithms for the research civil aircraft model (RCAM) during final approach and landing (FM(AG08), 1997a). The design problem is described in detail by FM(AG08) (FM(AG08), 1997b) and sections of the described flight trajectory are suitable for use in this work. In addition, the RCAM problem defines a set of control system design criteria and it can be assumed that it will be possible to design a control system that will meet these criteria. Therefore this work can assume that the system will never exceed the maximum allowed deviations described in the RCAM problem. In addition, the RCAM trajectory allows us to consider the air as incompressible because of the low speed and small changes with time.

## 1.1 Motivation

It is evident that most of the research to date has only modified the leading and trailing edges of the wing. Even Johnston et al., (2003) who come the closest to the methodology presented in this work only morph the trailing edge. Previous research has concentrated on drag optimization and gust load alleviation as well as investigations into the actuation power requirements of morphing wing technologies. Gern et al., (2002) have carried out related research before but they applied it to unmanned combat aerial vehicle (UCAV)s and did not investigate control system design methodologies. The FlexSys MACW (Hetrick et al., 2007) shows a lot of promise but it is still under development, uses only flexible leading and trailing edges and has not fully investigated the application of the technology to achieve practical roll control.

The design of a homogeneous wing with active camber roll control is a step towards a practical implementation of morphing wing technology and therefore an engineering model of a fully flexible homogeneous wing with variable camber actuation is the

focus of this research.

With modern technology (in terms of actuators and sensors), fly-by-wire systems and modern control techniques, it has become much more feasible to implement a flexible wing on a modern passenger aircraft. In order to begin bridging the gap between theoretical wing morphing concepts and practical application of the technology to real aircraft the optimal control of a real world aircraft needs to be investigated. In order to carry out such an investigation, a model of the system needs to be developed.

## 1.2 Objectives

This research presents a novel approach to modelling the variable camber wing and changing the camber of the whole airfoil instead of just portions of the leading and trailing edges.

The objectives of this research are:

1. To develop and validate a first-order aerodynamic model of a flexible wing with variable camber actuation.
2. To develop and verify a first-order structural model of a flexible wing with variable camber actuation.
3. To explore the predicted aero- and structural dynamics of a variable camber wing.

## 1.3 Dissertation Layout

Chapter 1 has provided an introduction to the work including a review of the background literature, a description of the motivation for the research and a set of objectives.

Chapter 2 presents the methodology of the investigation and covers the system modelling, its validation and the application to a real world problem considering the wing of the Cessna Citation V.

Chapter 3 develops the mathematical model of the system using static aerodynamic coefficients generated using a vortex lattice method (VLM) code and an aeroelastic

wing model based on strip theory. In the final section, the aeroelastic model is formulated in state-space form.

Chapter 4 presents the verification and validation of the aerodynamic model and verification of the aeroelastic model.

Chapter 5 presents the results obtained from simulations of the flexible wing aerodynamic and aeroelastic behaviour including detailed discussion and analysis.

Chapter 6 draws conclusions and makes recommendations for future work.

## 2 Methodology

The purpose of this investigation is to develop first-order aerodynamic and aeroelastic models of a camber controlled wing that would ultimately be used to demonstrate the feasibility of providing roll authority to a civil passenger aircraft. The extent of the verification and validation is limited to static and dynamic behavior that can be compared to a conventional rigid wing.

The wing will have integrated actuators capable of changing the camber in order to produce control forces and moments and, unlike the F/A-18 wing of the AAW program (Pendleton et al., 2000), will not have any conventional control surfaces. This work focuses on developing, verifying and validating the mathematical models against published data and does not investigate any methods that might be used to implement such a system. Approach and landing are the flight phases where the roll authority required is high but the air speed is low and therefore the control surfaces are at their least effective. These phases are the most demanding for a variable camber system and have been selected as the best at which to verify and validate the model.

The methodology is formulated in such a way that it can be readily extended to a complete aircraft model usable for control system design. In addition, further validation against experimental or computational fluid dynamics (CFD) data can be carried out in order to improve the range of applicability of the model.

### 2.1 Modelling

System dynamics are typically non-linear and, in the case of a complex, coupled system like the variable camber wing, difficult to model. Engineers usually start by developing a generic, non-linear mathematical description of the system and then proceed to simplify and ultimately linearise the system to make it easy to solve. The variable camber wing is a complex system and has aeroelastic coupling effects

that come into play. In order to investigate the system dynamics, a first order model will be developed in order to evaluate whether or not it is worth pursuing more detailed and complete representations. This work focuses on modelling the first order system dynamics with the aim of developing a variable camber actuation method and associated model. The model will be compared to known results from a rigid aircraft with conventional ailerons. The variable camber aerodynamics as well as the aeroelastic results cannot be validated against published data because at the time of this research no such data existed in the public domain. Therefore the results will be evaluated objectively by comparing them to published data where it is available and subjectively by extrapolating hypothesis that may explain the observed results. The modelling, verification and validation process used in this work is as follows:

1. Develop and validate an aircraft aerodynamic model.
2. Extend the aerodynamic model with a camber actuation methodology.
3. Develop and verify an aeroelastic model of the half wing.
4. Evaluate the camber actuation aerodynamics.
5. Evaluate the dynamics present in the aeroelastic model.

At low speeds and accelerations, the aerodynamics can be assumed to be quasi-steady, i.e. the instantaneous aerodynamic characteristics of the aircraft motion are assumed to be equal to those of the same aircraft moving with constant linear and angular velocities. When a wing changes its shape, the primary effect is to change the lift distribution. Secondary effects include changing the position of the aerodynamic centre and hence the pitching moment, changing the drag and changing the downwash. VLMs provide reliable means of modelling inviscid, incompressible flow over a wing and hence the linear region of the lift and pitching moment curves. Availability of a functional vortex lattice code called Tornado (Melin, 2000) drove the selection of the VLM for use in this work. VLMs model inviscid, incompressible flow over a wing by replacing the mean camber line with a vortex sheet and enforcing the boundary condition that no flow can occur perpendicular to the vortex sheet. VLMs are inherently steady-state and cannot predict dynamic (time-dependent) derivatives. In addition, the change in drag cannot be modelled accurately by the potential flow theory on which VLMs are based. The camber controlled wing is aerodynamically similar in function to conventional ailerons; they both change the spanwise lift distribution along the wing. Strip aerodynamic and structural data for a civil passenger aircraft was obtained from Tuzcu, (2001) who published discretized



data for the Cessna Citation V in his doctoral thesis. This data was adapted and is presented in Appendices A and B along with data from the Cessna Citation V operation and flight manuals which is presented in Appendices C, D, E and F. The wing, horizontal and vertical tails and engines were modelled as lifting surfaces.

In order to develop a camber actuation mechanism it is necessary to develop a model describing the wing camber and containing an actuation variable that allows it to be changed. The airfoils used on the wing of the Citation V are the Cessna 5501 at the root and the Cessna 5504 at the tip (Cessna Aircraft Company, 1989). These are proprietary airfoils for which the data is not freely available in the public domain. However, the NACA 23012 airfoil has the closest shape to that used on the Citation V (Lednicer ) and the aerodynamic characteristics are close enough that for the purposes of this investigation they will not affect the dynamic response of the system. In addition, the mathematical model of the camber line of the NACA family of airfoils is analytical (although, non-linear) and it provides an excellent means to implement actuation using the available parameters. Actuation using these variables has the added advantage that the aerodynamics will remain within the same family of airfoils which are well documented by Abbott and von Doenhoff, (1959).

For a first-order investigation it is unnecessary to use discrete element methods to develop an aeroelastic model and strip theory will suffice (Bismarck-Nasr, 1999). Strip theory assumes that the flow over each strip is two-dimensional and does not interact with the flow over any other strips, that the rotation angles are small and that the dynamics are quasi-steady. In addition, the camber control mechanism can be assumed to be rigid, i.e. there is no variation in the camber due to wing loading, meaning that no elastic degrees of freedom are added by the variable camber itself (Hetrick et al., 2007). A strip theory model based on the typical section in aeroelasticity that models the wing dynamics in terms of heave and twist as presented by Bismarck-Nasr, (1999) is therefore sufficient. It can also be assumed that changes in the position of the strip aerodynamic centre (AC), centre of gravity (CG) and elastic axis (EA) positions as a function of control deflection are negligible due to the low speed and assumption of small rotation angles. This provides a discretized model of the wing including local structural and aerodynamic effects that is derived from Lagrange's Equation. Structural damping is very difficult to model and therefore, for the purposes of this initial investigation, it can be omitted from the model and is stated as a limitation, leaving only aerodynamic damping. Note also that as long as the angle of twist remains small (less than  $15^\circ$ ), the effect of the drag is negligible because its contributions to both bending and twisting are multiplied by its trigonometric sine (Etkin and Reid, 1996).

## 2.2 Verification and Validation

In order to verify the mathematical model, it is necessary to confirm that the implementation accurately represents the underlying mathematical model (NAFEMS and ASME, 2006). The model is implemented in MATLAB because Tornado is MATLAB code. In addition, MATLAB is widely used in the aerospace industry and provides powerful tools for solving and analysing the behaviour of differential equations.

In order to validate the mathematical model, it is necessary to show how well the model represents the real world for the application considered in this work (NAFEMS and ASME, 2006). No data exists for much of the system being developed here and therefore only validation of the results pertaining to the rigid wing aerodynamics can be obtained by comparing them to the data published by Tuzcu (2001)..

In order to confirm that the modifications made to the Tornado code in order to implement the variable camber actuation mechanism are implemented correctly, as well as that the discrete model of the Citation V correctly represents the aircraft geometry, the aerodynamic model is verified and validated as follows:

1. The lift distribution is evaluated along the wing span and compared to the published data. An ideal lift distribution is elliptical (Anderson, 2001) and the actual lift distribution is expected to exhibit a similar shape except at locations close to the fuselage. The lift coefficient must also lie within acceptable bounds defined by the maximum lift coefficient of the airfoil.
2. The wing discretization is evaluated to confirm that the error between the calculated and published lift distributions converges to a minimum as the number of panels along both the span and chord is increased.
3. The longitudinal aerodynamics for the whole aircraft is evaluated and compared to the published data.
4. The lateral aerodynamics for the whole aircraft is evaluated and compared to the published data.

The aeroelastic model is verified as follows:

1. A continuous model of a uniform cantilever beam is developed and parametrized with a stiffness calculated at the wing mean aerodynamic chord (MAC).

2. The discrete aeroelastic model is parametrized as a uniform cantilever beam with a stiffness corresponding to the wing MAC.
3. The static deflection of the discrete cantilever beam is compared to the continuous cantilever beam.
4. The first four modes of the continuous cantilever beam are calculated and analysed.
5. The uncoupled and coupled free responses of the discrete cantilever beam are plotted and compared to the continuous cantilever beam.
6. The frequency of the free vibration of the discrete cantilever beam is compared to the first mode shape of the continuous cantilever beam.

The discrete aeroelastic model can be verified against any comparable set of published results as long as it is parametrized correctly. In this case, the closed form analytical solution presented by Rao, (1995) for bending and torsion of a uniform cantilever beam was very appealing because it is simple to implement and the mode shapes were published. In addition, although Rao, (1995) does not present the torsion mode shapes, Bismarck-Nasr, (1999) presents them for the same modelling technique (separation of variables) and the same problem of a uniform cantilever beam.

While a uniform cantilever beam is suitable for verification, the approach falls short for validation purposes because it does not provide a good comparison for the discrete model parametrized as the Citation V wing.

Evaluation of the variable camber aerodynamics and the aeroelastic wing model is carried out at the flight state corresponding to segment 1 of the RCAM trajectory described in Appendix F with the aircraft weight at the maximum landing weight  $m_{land}$ . This low speed, high angle of attack (AoA), high mass flight has the advantage of being the most challenging in terms of manoeuvring the aircraft because the authority of the control surfaces is severely reduced and the aircraft inertia is high. Therefore an evaluation of the variable camber wing under these conditions will consider the worst case scenario in terms of control authority.

This flight state also lies within the limitations of the model because it is both low speed and steady-state and therefore the air will be incompressible and the assumption of quasi-steady dynamics will be valid. The modelling of the aircraft does not consider the effect of flaps on the variable camber wing and therefore the aircraft configuration is always flaps up. This means that a higher than normal

AoA is required in order to maintain lift at approach speed. Note however that the approach speed at maximum landing weight of  $58\text{ m/s}$  is still well above the clean configuration stall speed of  $48\text{ m/s}$ .

## 2.3 Application

Having validated the aerodynamic model and verified the aeroelastic model, investigations are carried out into the aero- and structural dynamics of the variable camber wing. The flight state at which these investigations are carried out is the same low speed, high AoA approach at which the models were verified and validated.

There are three primary applications of interest:

1. To parametrize the discrete aeroelastic model to represent the wing of the Citation V.
  - (a) To compare the static deflection of the wing to the discrete cantilever beam.
  - (b) To compare the free response of the wing to the discrete cantilever beam.
2. To investigate the aerodynamics and roll authority of differentially actuated variable camber wings to that of conventional ailerons.
3. To investigate the aeroelastic dynamics of the variable camber wing and determine whether it is stable in response to actuation input and external excitations.

The wing has a discontinuity about a quarter of the way out from the root. Due to the thickness and longer chord of the inboard section, the first-order dynamics are expected to be dominated by the outboard three-quarters of the span with the effect of the inboard portion only showing in the higher order dynamics. In addition, the first order mode should not differ significantly from the uniform cantilever beam, other than perhaps for the shape to have a discontinuity (non-linearity) at the same position as the wing. For qualitative analysis purposes it is of interest to show that the natural frequency of the first wing mode is comparable to both the uniform cantilever and in the correct range for the type of aircraft under consideration. Prediction of higher modes is less reliable, however their influence over the model at the conditions under which it is being tested can be inferred from the reference cantilever beam.

The camber actuation aerodynamics are investigated in terms of the dependence of the aerodynamic forces on the magnitude and direction of the camber actuation. In addition, the roll authority is analysed in terms of lift distribution along the wing span.

The performance of the aeroelastic model is evaluated together with the interactions between the structure and the aerodynamics of the variable camber wing. In order to do this, the response of the aeroelastic model is analysed with respect to external disturbances as well as control input. The response is evaluated using Bode plots.

## 3 Mathematical Model

This chapter presents the development of first-order aerodynamic and aeroelastic models of a variable camber wing according to the methodology described in Section 2.1.

Section 3.1 presents the definitions of the coordinate systems and the discretization technique.

Section 3.2 presents the development of the aerodynamic model of the whole aircraft and its implementation in the Tornado vortex lattice code. The model is extended to include a wing camber actuation variable and the linear variation of the camber along the wing span from root to tip.

Section 3.3 presents the development of the aeroelastic model based on strip theory which provides a discretized model of the wing including local structural and aerodynamic effects.

Section 3.4 presents the aeroelastic equations of motion in state-space form.

### 3.1 System Definitions

This section defines the reference frames within which the mathematics of this work are presented. The definitions of the coordinate systems, standard atmosphere, actuator movements and wing discretization are presented.

The VLM and strip theory models require the wing to be discretized into  $n$  chord-wise strips as shown in Figure 3.1. The VLM further discretizes each strip into a number of panels along the chord. The figure also shows the elastic axis which is defined to coincide with the  $y_W$  axis of the wing coordinate system. The reference point for each strip is defined as mid-way along the span of the strip on the elastic axis. All moments of inertia are taken referred to this point.

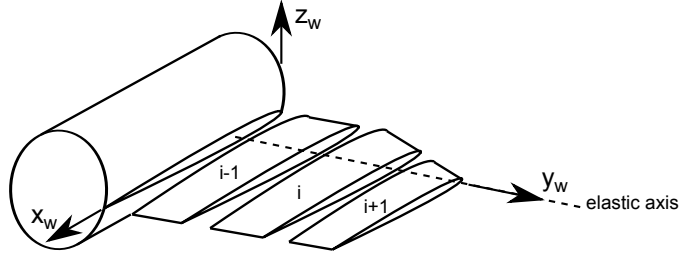


Figure 3.1: Discretization of the wing span into  $n$  chordwise strips

The wing coordinate system is used when modelling the structural dynamics of the strip and is defined with respect to the body coordinate system. Figure 3.2 illustrates the wing (subscript  $W$ ) and body (subscript  $B$ ) coordinate systems and the left and right wings which are defined when facing forward along the aircraft centre line.

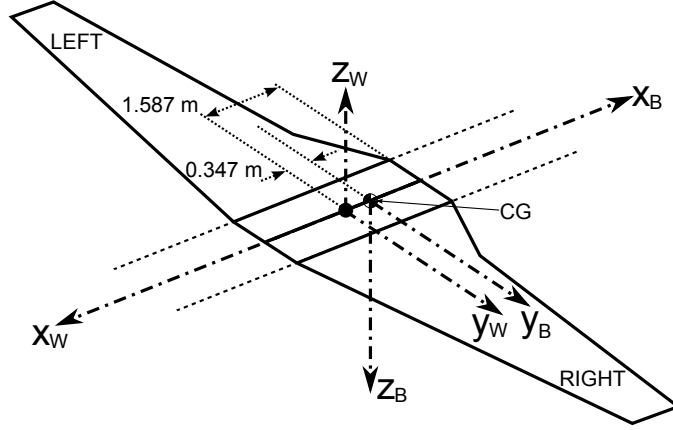


Figure 3.2: Definition of the wing and body coordinate systems

The **wing** coordinate system is indicated by  $[ \ ]^W$  for vectors and tensors and  $(x_W, y_W, z_W)$  for vector components. It is fixed in the body reference frame and is defined as having its x axis pointing backward along the longitudinal axis of the aircraft, its y axis pointing towards the tip of the right wing and its z axis pointing up. The origin of the wing coordinate system is fixed at the same location used by Tuzcu, (2001) (see Appendix A).

The **body** coordinate system is indicated by  $[ \ ]^B$  for vectors and tensors and  $(x_B, y_B, z_B)$  for vector components. It is fixed in the body reference frame and is defined as having its x axis pointing forward along the longitudinal axis of the aircraft, its y axis pointing towards the tip of the right wing and its z axis pointing down. The origin of the body coordinate system is coincident with the CG of the

aircraft.

In order to calculate the aerodynamic forces and moments, the properties of the atmosphere need to be defined. For this purpose the atmosphere is considered to be at rest and the 1976 International Standard Atmosphere (ISA) model is used.

Finally, it is necessary to define the signs of the aircraft actuator movements which follow standard conventions as follows:

- A downward deflection of the elevator trailing edge is positive ( $\delta_e$ ).
- A downward deflection of the right aileron trailing edge coupled with a corresponding upward deflection of the left aileron trailing edge is defined as positive ( $\delta_a$ ).
- Similarly, an increase in camber of the right wing coupled with a corresponding decrease in camber of the left wing is defined as positive ( $\delta_c$ ).
- A leftwards movement of the rudder trailing edge is positive ( $\delta_r$ ).

### 3.2 Aerodynamics

In order to validate the longitudinal and lateral aerodynamics of the complete aircraft; a first-order linear model is developed using non-dimensional coefficients. For this analysis it is sufficient to consider only the aerodynamic coefficients themselves (and not the actual forces) because these can be compared to known values for a rigid aircraft.

The aerodynamic forces and moments are functions of the shape and size of the aircraft (represented by a characteristic length  $c$ ), atmospheric density  $\rho$ , atmospheric pressure  $p$ , the linear velocity of the aircraft CG with respect to the air  $\mathbf{v}_B^A$ , the angular velocity of the aircraft with respect to the air  $\omega^{BA}$ , the acceleration of the aircraft with respect to the air  $D^A \mathbf{v}_B^A$  and the control surface deflections  $\delta$ . These relationships are represented in functional form as follows (Zipfel, 2000):

$$\mathbf{f}_a = f(c, \rho, p, \mathbf{v}_B^A, \omega^{BA}, D^A \mathbf{v}_B^A, \delta) \quad (3.1a)$$

$$\mathbf{m}_a = f(c, \rho, p, \mathbf{v}_B^A, \omega^{BA}, D^A \mathbf{v}_B^A, \delta) \quad (3.1b)$$

Table 3.1 shows a  $\bullet$  in the boxes corresponding to derivatives that exist and a  $\circ$  in the boxes of derivatives that are normally negligible according to Etkin and Reid,



(1996). The symbols in Table 3.1 are defined as follows:  $u$  is the speed of the aircraft along the x axis of the body coordinate system;  $\beta$  is the sideslip angle;  $\alpha$  is the angle of attack;  $p$ ,  $q$  and  $r$  are the roll, pitch and yaw rates respectively;  $\delta_c$ ,  $\delta_e$  and  $\delta_r$  are the camber setting, elevator and rudder angles respectively.  $D$ ,  $Y$  and  $L$  are the drag, side and lift forces;  $\ell$ ,  $m$  and  $n$  are the rolling, pitching and yawing moments respectively.

The following considerations are taken into account in Table 3.1:

- The flight state corresponding to Segment 1 of the RCAM trajectory (Appendix F) represents low speed, high AoA flight. Therefore the aerodynamic behaviour is steady which allows the  $\dot{u}$ ,  $\dot{\alpha}$  and  $\dot{\beta}$  derivatives to be discarded.
- The  $u$  derivatives are a function of compressibility, aeroelastic and propulsive effects (Etkin and Reid, 1996). Therefore the  $u$  derivatives can be discarded because the air is incompressible, the aeroelastic effects are accounted for in the model of the wing structure and the engines are positioned behind the wing and therefore do not affect the airflow over the wing. It is also assumed that aerodynamic interference effects of the engine with the horizontal stabilizer are negligible.
- The dependence of the longitudinal aerodynamics on the variable camber is investigated as part of this work and therefore these derivatives are marked with a \*.

Table 3.1: First order dimensional derivatives

$[f_a]^S, [m_a]^S$	$u$	$\beta$	$\alpha$	$p$	$q$	$r$	$\dot{u}$	$\dot{\beta}$	$\dot{\alpha}$	$\delta_c$	$\delta_e$	$\delta_r$
$D$	○		●		○		○		○	*	●	
$L$	○		●		●		○		○	*	●	
$m$	○		●		●		○		○	*	●	
$Y$		●		●		●		○		●		●
$\ell$		●		●		●		○		●		●
$n$		●		●		●		○		●		●

Analysing Table 3.1 and expressing drag using the standard method of adding profile and induced drag shows that the aerodynamic force and moment coefficients are expressed in terms of non-dimensional derivatives as follows:

$$C_D = C_{D_0} + \gamma C_L^2 \quad (3.2a)$$

$$C_Y = C_{Y_\beta} \beta + C_{Y_p} p + C_{Y_r} r + C_{Y_{\delta_r}} \delta_r \quad (3.2b)$$

$$C_L = C_{L_\alpha} \alpha + C_{L_q} q + C_{L_{\delta_e}} \delta_e \quad (3.2c)$$

$$C_\ell = C_{\ell_\beta} \beta + C_{\ell_p} p + C_{\ell_r} r + C_{\ell_{\delta_c}} \delta_c + C_{\ell_{\delta_r}} \delta_r \quad (3.2d)$$

$$C_m = C_{m_\alpha} \alpha + C_{m_q} q + C_{m_{\delta_e}} \delta_e \quad (3.2e)$$

$$C_n = C_{n_\beta} \beta + C_{n_p} p + C_{n_r} r + C_{n_{\delta_c}} \delta_c + C_{n_{\delta_r}} \delta_r \quad (3.2f)$$

where  $\gamma$  is the induced drag constant given in Appendix E.

### 3.2.1 Vortex Lattice Method

Tornado is a vortex lattice code implemented in MATLAB (Melin, 2000). Tornado models finite wings and also provides the option of including the Prandtl-Glauert compressibility correction. Tornado models cambered wings by rotating the normal of each panel so that it is perpendicular to the camber line at the collocation point. The collocation point is the point at which Tornado enforces the boundary condition and is defined to be positioned at  $\frac{3}{4}$  of the panel chord. Tornado improves on classic vortex lattice methods by using a 7 segment horseshoe vortex which re-aligns itself with the free stream when it leaves the trailing edge.

Tornado stores the panel slopes for each pair of symmetric partitions in a one dimensional vector,  $\mathbf{S}$ , the indexing of which is illustrated in Figure 3.3 (Melin, 2000). The letters belong to partition 1, the numbers belong to partition 2, etc. The slope

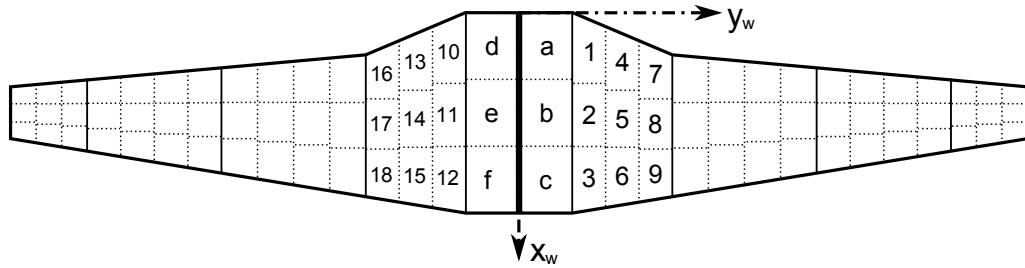


Figure 3.3: Numbering scheme used by Tornado to reference individual wing panels

vectors are defined as follows:

$$\begin{aligned} \mathbf{S}_1 &= \left[ \left( \frac{dz}{dx} \right)_{11} \left( \frac{dz}{dx} \right)_{12} \cdots \left( \frac{dz}{dx} \right)_{1i} \right] \\ \mathbf{S}_2 &= \left[ \left( \frac{dz}{dx} \right)_{21} \left( \frac{dz}{dx} \right)_{22} \cdots \left( \frac{dz}{dx} \right)_{2i} \right] \\ &\vdots \\ \mathbf{S}_j &= \left[ \left( \frac{dz}{dx} \right)_{j1} \left( \frac{dz}{dx} \right)_{j2} \cdots \left( \frac{dz}{dx} \right)_{ji} \right] \end{aligned} \quad (3.3)$$

where  $\mathbf{S}_j$  is the slope vector of partition  $j$  and  $\left(\frac{dy}{dx}\right)_{ji}$  is the slope of panel  $i$  in partition  $j$ . Similarly,  $\frac{dz}{dy}$  defines the y component of the panel slope.

In order to implement variable camber control in Tornado, the calculation of the panel normals  $\frac{dz}{dx}$  is replaced with a calculation which varies the camber as a function of an actuation variable.  $\frac{dz}{dy}$  remains a function of dihedral angle only. Note that the number of chord panels can vary between different partitions and the coordinate system used by Tornado is identical to the wing coordinate system defined in Section 3.1.

In Tornado the wing, horizontal and vertical tails and engine are modelled as rigid lifting surfaces (Melin, 2000). In this work the elevator and rudder control surfaces are included in the model and, where necessary for comparison purposes, the ailerons are modelled as well. Additionally, the fuselage is included in the model for evaluation of its effect on the dependency of the yawing and rolling moment coefficients on sideslip angle  $\beta$ .

### 3.2.2 Airfoil Camber Actuation

Tornado had two methods of calculating the camber of an airfoil (Melin, 2000):

1. Using the mathematical definition of the camber line for a National Advisory Committee for Aeronautics (NACA) 4 digit airfoil and,
2. Using the airfoil coordinates directly.

The proprietary Citation V airfoils can be represented by a modified NACA 5 digit airfoil, 23014 at the root and 23012 at the tip (Lednicer ). It was therefore necessary to add a third method to Tornado using the camber function for a NACA 5 digit airfoil including an actuation variable.

The camber of the NACA 5 digit airfoil series is defined as follows (Abbott and von Doenhoff, 1959):

$$z = \frac{k}{6}(x^3 - 3mx^2 + m^2(3 - m)x) \quad \text{for } x \leq p \quad (3.4a)$$

$$z = \frac{km^3}{6}(1 - x) \quad \text{for } x > p \quad (3.4b)$$

where  $p$  is the position of the maximum camber as a percentage of the chord,  $m$  is chosen so that the maximum camber occurs at  $p$  and  $k$  is chosen to give a desired

lift coefficient. For the NACA 23012 airfoil the value of these constant are given in Table 3.2.

Table 3.2: Parameters defining the NACA 23012 airfoil

Parameter	Value
$p$	0.15
$m$	0.2025
$k$	15.957

A plot of the NACA 23012 airfoil and camber line at the wing MAC is shown in Figure 3.4. Note that the thickness distribution of the airfoil does not effect the

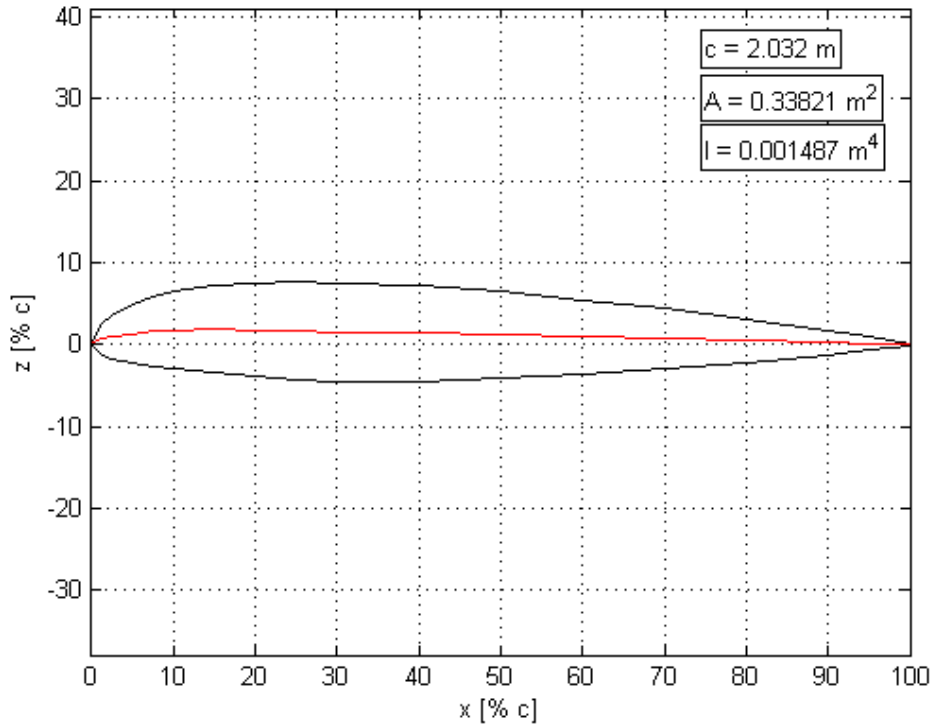


Figure 3.4: Camber line and cross-section profile of a NACA23012 airfoil with maximum thickness of 12% and maximum camber at  $p = 15\%$  of  $c$

model because the vortex sheet in the VLM is infinitely thin. Therefore only the camber line is modified while the thickness distribution is ignored in the model.

In order to implement camber control it is necessary to determine how the camber can be changed by manipulating the parameters defining the camber line. This is achieved by multiplying each one of the parameters in Table 3.2 by  $(1 + \Delta)$  as follows:

$$p' = p(1 + \Delta) \quad (3.5a)$$

$$m' = m(1 + \Delta) \quad (3.5b)$$

$$k' = k(1 + \Delta) \quad (3.5c)$$

Varying  $\Delta$  from -1 to +1 for one variable while keeping the other two unchanged shows the effect of that variable on the shape of the camber line.

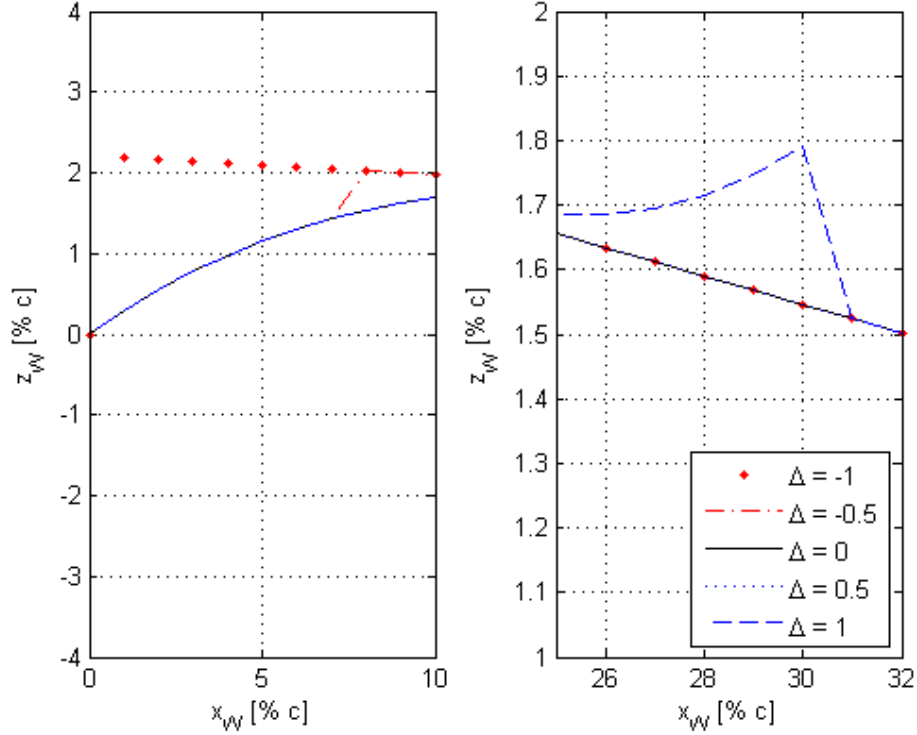


Figure 3.5: Effect of  $p$  on the camber line shape with  $m$  and  $k$  fixed at the values shown in Table 3.2

Figure 3.5 shows that decreasing  $p$ , ie. moving the position of maximum camber towards the airfoil leading edge, causes a discontinuous increase in camber within the first 10% of the chord while increasing  $p$  causes a discontinuous increase in camber between 30% and 31% of the chord. This is consistent with a change in the position of the transition point (non-linearity) between Equation (3.4a) and (3.4b). The equations defining the slope of the camber line before and after the transition point are investigated as follows:

$$\frac{dz}{dx} = \frac{k}{6}(3x^2 - 6mx + m^2(3 - m)) \quad \text{for } x \leq p \quad (3.6a)$$

$$\frac{dz}{dx} = -\frac{km^3}{6} \quad \text{for } x > p \quad (3.6b)$$

In order for the camber line to have no discontinuities, the slopes of the two equations must be equal at  $p$ . Setting Equation (3.6a) equal to Equation (3.6b) results in the cancellation of  $k$  and the following dependency of  $p$  on  $m$ :

$$p = \sqrt{\frac{2}{3}m^3} + m \quad (3.7)$$

This shows that  $p$  must vary with  $m$  in order to ensure a continuous camber line.

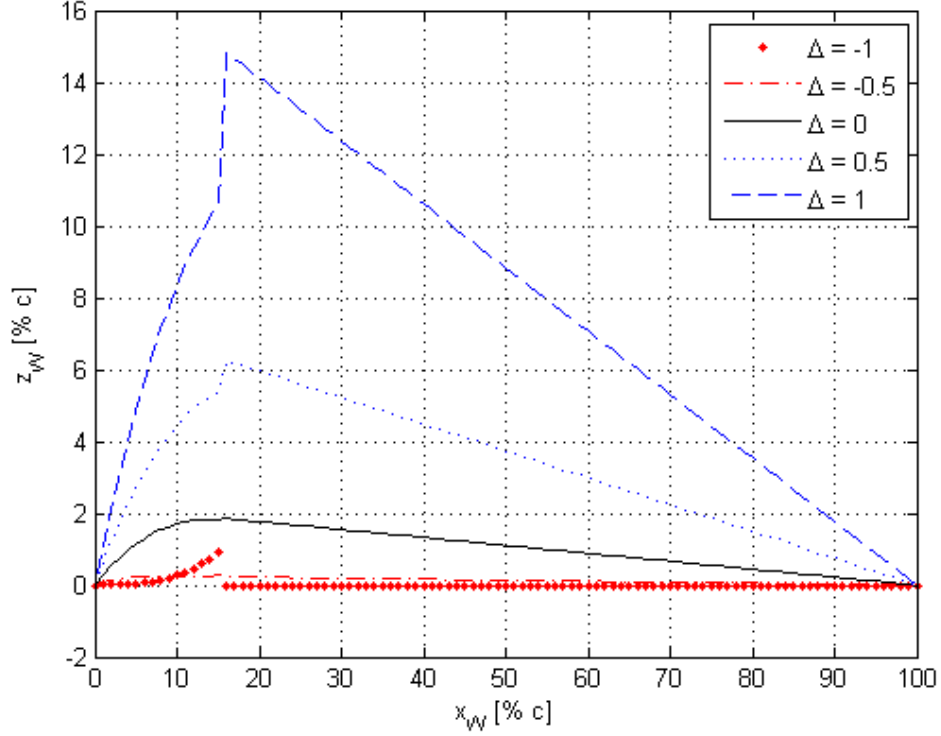


Figure 3.6: Effect of  $m$  on the camber line shape with  $p$  and  $k$  fixed at the values shown in Table 3.2

Figure 3.6 shows that all changes in parameter  $m$  cause a discontinuity at the 15% chord position, ie. at the position of maximum camber. It is also evident that the effect of a change in parameter  $m$  is much greater than the effect of parameter  $p$  as expected from Equation (3.6b) which shows that the slope of the aft section of the camber line is proportional to  $m^3$ .

Figure 3.7 shows that decreasing parameter  $k$  yields a smooth decrease in camber while increasing parameter  $k$  yields a smooth increase in camber. Equation (3.7) proves that parameter  $k$  has no influence on the smoothness of the camber line and is therefore the best choice of actuation variable because it yields a directly proportional camber response as long as  $p$  and  $m$  are held constant. Figure 3.7 also shows that if  $\Delta = -1$  the wing has no camber and therefore will produce no lift at

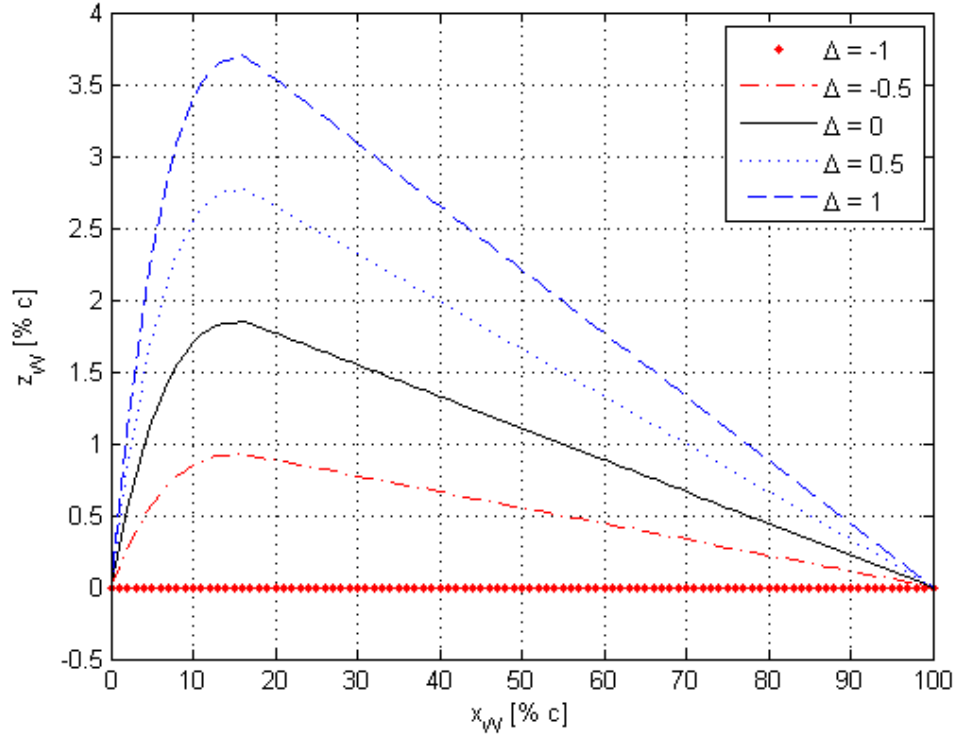


Figure 3.7: Effect of  $k$  on the camber line shape with  $p$  and  $m$  fixed at the values shown in Table 3.2

zero AoA. However, at  $\Delta = +1$  the camber is doubled and hence the lift at zero AoA will be greater than at the nominal camber position.

Therefore, the camber line is defined using Equation (3.4b) and Table 3.2 and dimensionless actuation variable  $\delta_k$  so that:

$$k = 15.957(1 + \delta_k) \quad (3.8)$$

Tornado was modified to accept 5 series camber lines and then the implementation of these camber lines was further modified to accept the actuation variable  $\delta_k$ . Tornado only provides results in the linear region of the lift curve slope (Melin, 2000) and therefore cannot predict the effect of  $\delta_k$  on  $C_{L_{max}}$ . A negative value of  $k$  does not correspond to reflex camber. Instead, it is equivalent to turning the airfoil upside down which means that the same magnitude of aerodynamic forces are generated but in the opposite direction.

The minimum magnitude of  $k$  is 0 which corresponds to  $\delta_k = -1$  and a symmetrical airfoil with a design lift coefficient of 0.3. The thickness distributions of the NACA 5 series airfoils are the same as the 4 series (Abbott and von Doenhoff, 1959) and therefore  $\delta_k = -1$  corresponds to the 4 series airfoil with the same thickness (eg.

20012  $\equiv$  0012). Jacobs and Pinkerton, (1935) conducted wind tunnel tests on NACA 5 Series airfoils in which the position and amount of maximum camber was varied in order to investigate the effect on the aerodynamic properties. They obtained results for values of camber up to 2.7% and showed that  $C_{L_{max}}$  varied between 1.56 and 1.67 within this range. Jacobs et al., (1935) also carried out wind tunnel tests on NACA 4 Series airfoils and obtained results for maximum camber up to 6%. They showed that  $C_{L_{max}}$  increased from 1.6 to approximately 1.75 as the maximum camber increased from 2% to 6% and, when it is positioned 20% from the leading edge. However, they did not test an airfoil with the position of maximum camber as far forward (15% from the leading edge) as the NACA 23012.

Based on the above analysis and the similarities between the NACA 4 and 5 Series airfoils, a maximum camber of 6% is selected for the variable camber wing. This corresponds to  $\delta_k = 2.25$  and therefore the range of  $\delta_k$  is given by  $-4.25 < \delta_k < 2.25$ .

### 3.2.3 Spanwise Camber Variation

In order to achieve roll authority the camber had to be varied along the span. The following convention is defined: a positive actuation input shall cause a negative rolling moment by inducing a lift differential between the left and right wings. This is done by decreasing the camber on the left wing, thereby decreasing the lift produced by the left wing and increasing the camber on the right wing, thereby increasing the lift produced by the right wing. This convention is analogous to that used for ailerons. This technique is applied as follows:

$$\begin{aligned} k_{left} &= 15.957(1 - \delta_k) \\ k_{right} &= 15.957(1 + \delta_k) \end{aligned} \tag{3.9}$$

An important additional consideration is that the camber of the airfoil at the wing root is more difficult to change than the camber at the tip because the root has a greater cross-sectional area than the tip and is therefore stiffer. For this reason the wing semi-span is divided into three sections (A, B and C or D, E and F) and the amount of actuation input is varied linearly along the span in sections B and E as shown in Figure 3.8.

Using Figure 3.8 the definition of the actuation variable is further refined in terms



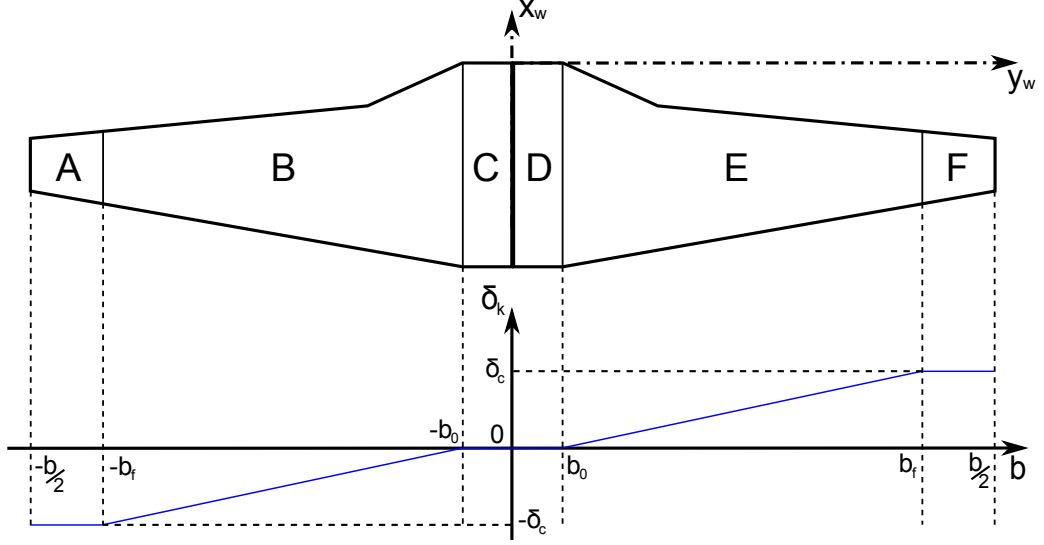


Figure 3.8: Linear variation of camber actuation along the wing span

of dimensionless variable  $\delta_c$  as follows:

$$\begin{aligned}
 \delta_k &= \delta_c \frac{y + b_0}{b_f - b_0} \quad \text{if} \quad -b_0 < y < -b_f \\
 \delta_k &= 0 \quad \text{if} \quad 0 < |y| < b_0 \\
 \delta_k &= \delta_c \frac{y - b_0}{b_f - b_0} \quad \text{if} \quad b_0 < y < b_f \\
 \delta_k &= \delta_c \quad \text{if} \quad b_f < |y| < \frac{b}{2}
 \end{aligned} \tag{3.10}$$

where  $\delta_k$  will be used in Equation (3.9) and  $\delta_c$  is the overall camber actuation variable.

This provides a parametrizable model in which the camber can be varied along the span. The limits of  $b_0$  and  $b_f$ , the start and end points of the camber actuation, are going to be determined by the structural implementation of this actuation scheme. As this is not being considered in this work, the only limit that can be stated is that  $b_0$  must lie at or outside the fuselage. The range of  $\delta_c$  is the same as  $\delta_k$  discussed at the end of Section 3.2.2. Note that a maximum value of  $\delta_c$  will only cause a maximum value of  $\delta_k$  at position  $b_f$ .

### 3.3 Wing Structure

The wing structure is modelled using strip theory by dividing the half wing into  $n$  chord-wise strips where each strip represents the typical section used in aeroelasticity

as shown in Figure 3.9 (Bismarck-Nasr, 1999). The chord length of strip  $i$  is the mean of it's inboard and outboard lengths.

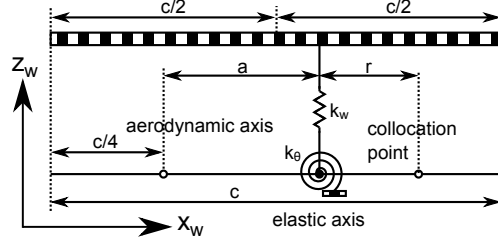


Figure 3.9: Model of the typical section in aeroelasticity

For each strip at station  $y_i$  the heave and twist is given by Equations (3.11a) and (3.11b) respectively (Bismarck-Nasr, 1999). The translation coordinate  $w$  is positive upwards (in the direction of  $z_W$ ) and the rotation coordinate  $\hat{\theta}$  is positive nose up according to the right hand rule for rotation around the  $y_W$  axis.

$$w(y, t) = W(y)\underline{w} \quad (3.11a)$$

$$\hat{\theta}(y, t) = H(y)\underline{\hat{\theta}} \quad (3.11b)$$

$W(y)$  and  $H(y)$  are assumed to be uncoupled mode shapes in bending and torsion respectively and are normalized to unit values at the wing tip.

$W(y)$  is assumed to be the first bending mode of a cantilever beam as given by Equation 28 (Bismarck-Nasr, 1999).

$$W(y) = \frac{\sin \zeta y - \sinh \zeta y - \kappa (\cos \zeta y - \cosh \zeta y)}{|\sin \zeta s - \sinh \zeta s - \kappa (\cos \zeta s - \cosh \zeta s)|} \quad (3.12)$$

where:

$$\kappa = \left( \frac{\sin \zeta s + \sinh \zeta s}{\cos \zeta s + \cosh \zeta s} \right) \quad (3.13)$$

where  $s$  is the wing semi-span (cantilever beam length) and  $\zeta s = 1.875104$  corresponds to the first mode shape of a cantilever beam in bending.

$H(y)$  is assumed to be the first torsion mode of a cantilever beam as given by Equation (3.14) (Bismarck-Nasr, 1999).

$$H(y) = \sin \frac{\pi y}{2s} \quad (3.14)$$

Lagrange's Equation is used to obtain the equation of motion for the wing structure:

$$\frac{d}{dt} \left( \frac{\partial L}{\partial \dot{q}} \right) - \frac{\partial L}{\partial q} = Q \quad (3.15)$$

$L = T - U$  is known as the Lagrangian,  $q$  is a generalized coordinate and  $Q$  is a generalized force. The kinetic energy is given by (Bismarck-Nasr, 1999):

$$T = \frac{1}{2}M\dot{w}^2 + \frac{1}{2}I_\theta\dot{\hat{\theta}}^2 + S\dot{w}\dot{\hat{\theta}} \quad (3.16)$$

The strain energy expression is given by (Bismarck-Nasr, 1999):

$$U = \frac{1}{2}k_w w^2 + \frac{1}{2}k_\theta \hat{\theta}^2 \quad (3.17)$$

Substituting Equations (3.16) and (3.17) into Equation (3.15) yields the complete undamped equation of motion for the half wing.

$$\begin{bmatrix} M & S \\ S & I_\theta \end{bmatrix} \begin{bmatrix} \ddot{w} \\ \ddot{\hat{\theta}} \end{bmatrix} + \begin{bmatrix} k_w & 0 \\ 0 & k_\theta \end{bmatrix} \begin{bmatrix} w \\ \hat{\theta} \end{bmatrix} = \begin{bmatrix} Q_w \\ Q_\theta \end{bmatrix} \quad (3.18)$$

The variables  $M$ ,  $I_\theta$ ,  $S$ ,  $k_w$  and  $k_\theta$  are complicated integrals involving the mode shapes and anti-derivatives do not always exist (Bismarck-Nasr, 1999). Therefore the method of exhaustion is used to perform the integration as follows:

$$M = \int_0^l m(y)[W(y)]^2 dy = l \sum_{i=1}^n \sum_{j=1}^{2^i-1} (-1)^{j+1} 2^{-i} m(jl2^{-i}) [W(jl2^{-i})]^2 \quad (3.19)$$

$$I_\theta = \int_0^l I_{yy}(y)[H(y)]^2 dy = l \sum_{i=1}^n \sum_{j=1}^{2^i-1} (-1)^{j+1} 2^{-i} I_{ea}(jl2^{-i}) [H(jl2^{-i})]^2 \quad (3.20)$$

$$S = \int_0^l S_{ea} W(y) H(y) dy = l \sum_{i=1}^n \sum_{j=1}^{2^i-1} (-1)^{j+1} 2^{-i} S_{ea} W(jl2^{-i}) H(jl2^{-i}) \quad (3.21)$$

The spring stiffness's are given by (Bismarck-Nasr, 1999):

$$k_w = \int_0^l EI(y) \left[ \frac{\partial^2}{\partial y^2} [W(y)] \right]^2 dy = l \sum_{i=1}^n \sum_{j=1}^{2^i-1} (-1)^{j+1} 2^{-i} EI(jl2^{-i}) \left[ \frac{\partial^2}{\partial y^2} [W(jl2^{-i})] \right]^2 \quad (3.22a)$$

$$k_\theta = \int_0^l GJ(y) \left[ \frac{\partial^2}{\partial y^2} [H(y)] \right]^2 dy = l \sum_{i=1}^n \sum_{j=1}^{2^i-1} (-1)^{j+1} 2^{-i} GJ(jl2^{-i}) \left[ \frac{\partial^2}{\partial y^2} [H(jl2^{-i})] \right]^2 \quad (3.22b)$$

The generalized forces in Equation (3.18) are calculated using the incremental work done by the external aerodynamic lift in moving the wing in the direction of  $w$  and pitching moment in rotating the wing through  $\hat{\theta}$  (about the elastic axis). The incremental work done is given by:

$$\delta W = L\delta w + M_{ea}\delta\hat{\theta} \quad (3.23)$$

The lift and pitching moment in Equation (3.23) are given in terms of the non-dimensional lift and pitching moment coefficients as follows:

$$L = qS_w C_L = qS_w \left[ C_{L_\alpha} \alpha + \sum_{i=1}^n C_{L_{\alpha_i}} \alpha_i + C_{L_{\delta_c}} \delta_c \right] \quad (3.24a)$$

$$M_{ea} = M_{aa} + aL = qS_w \bar{c} C_m + aL = qS_w \bar{c} C_{m_\alpha} \alpha + aL \quad (3.24b)$$

The local strip AoA is given in terms of  $w$  and  $\hat{\theta}$  as follows:

$$\alpha_i = \hat{\theta} - \frac{\dot{w}}{V} + \frac{\dot{\hat{\theta}} r}{V} = H(y) \hat{\theta} - \frac{W(y)}{V} \underline{\dot{w}} + \frac{H(y)r}{V} \underline{\dot{\hat{\theta}}} \quad (3.24c)$$

where  $q = \frac{1}{2} \rho V^2$  is the dynamic pressure,  $S_w$  is the wing reference area,  $a$  distance from the aerodynamic centre (AC) to the elastic axis (EA) as shown in Figure 3.9,  $r$  distance from the collocation point to the EA as shown in Figure 3.9 and  $\alpha_i$  is the local AoA of strip  $i$ . Therefore:

$$\begin{aligned} & \begin{bmatrix} Q_w \\ Q_\theta \end{bmatrix} \quad (3.25) \\ = & \begin{bmatrix} -\frac{qS_w}{V} \sum_{i=1}^n C_{L_{\alpha_i}} W(y) & \frac{qS_w r}{V} \sum_{i=1}^n C_{L_{\alpha_i}} H(y) \\ -\frac{qS_w}{V} \sum_{i=1}^n a C_{L_{\alpha_i}} W(y) & \frac{qS_w r}{V} \sum_{i=1}^n a C_{L_{\alpha_i}} H(y) \end{bmatrix} \begin{bmatrix} \underline{\dot{w}} \\ \underline{\dot{\hat{\theta}}} \end{bmatrix} \\ & + \begin{bmatrix} 0 & qS_w \sum_{i=1}^n C_{L_{\alpha_i}} H(y) \\ 0 & qS_w \sum_{i=1}^n a C_{L_{\alpha_i}} H(y) \end{bmatrix} \begin{bmatrix} \underline{w} \\ \underline{\hat{\theta}} \end{bmatrix} \\ & + \begin{bmatrix} qS_w C_{L_\alpha} \\ qS_w (\bar{c} C_{m_\alpha} + a C_{L_\alpha}) \end{bmatrix} \alpha + \begin{bmatrix} qS_w C_{L_{\delta_c}} \\ qS_w a C_{L_{\delta_c}} \end{bmatrix} \delta_c \end{aligned}$$

Note that the signs of the elements of the matrices in Equation (3.25) are dependant on the mode shapes and the position of the EA with respect to the AC. In addition, the matrices in Equation (3.25) are functions of both the flight state and the airfoil geometry. Therefore, no detailed analysis about the performance can be made by inspection because the relative magnitudes and signs of the terms in the matrices are unknown and depend on how the problem is defined. However, the general composition of the equation is analysed as follows:

1. There exists an aerodynamic damping matrix ( $C_{aero}$ ) which couples the vertical and twist velocities and is directly proportional to the aircraft speed  $V$  (through the term  $\frac{q}{V}$ ).
2. There exists an aerodynamic stiffness matrix ( $K_{aero}$ ) which couples the twist angle to the vertical displacement and is proportional to the square of the aircraft speed  $V$  (through  $q$ , the dynamic pressure).
3. There is a vector coupling the aircraft aerodynamics (aircraft AoA  $\alpha$ ) with the local strip dynamics and it is proportional to the square of the aircraft speed.

4. There is a vector coupling the variable camber control  $\delta_c$  with the local strip dynamics and it is proportional to the square of the aircraft speed.

Aeroelastic instabilities will not affect the validity of the results because they will not occur at the low airspeed at which this investigation is carried out (the variable camber wing has the same stiffness as the conventional wing). The validity of the model will however be limited to the approach and landing phases of flight.

### 3.4 State Space

The aeroelastic equations of motion are formulated in state-space form for the following reasons:

- The set of simultaneous differential equations are represented in the time domain using matrices and can be formulated in state-space form directly,
- The model has multiple inputs and multiple outputs and may have non-zero initial conditions,
- State-space models are easy to solve and analyse in either the time or frequency domains using MATLAB,
- State-space form lends itself to future control system design applications using both linear and non-linear control theory.

The structural equations of motion are formulated in state-space form as follows:

$$\dot{\mathbf{x}} = \mathbf{A}\mathbf{x} + \mathbf{B}u \quad (3.26a)$$

$$\mathbf{y} = \mathbf{C}\mathbf{x} \quad (3.26b)$$

The system matrix  $\mathbf{A}$  is a 4 x 4 matrix that models the system dynamics.  $\mathbf{B}$  is a 4 x 1 column vector that models the effect of external input  $u$  on the system.  $\mathbf{C}$  is a 2 x 4 matrix mapping the state vector to the measured output.

The wing structural dynamics are represented by the state vector:  $\mathbf{x} = [\underline{\dot{w}} \ \underline{\dot{\theta}} \ \underline{w} \ \underline{\theta}]^T$  and rearranging Equation (3.18) yields the state space form.

$$\begin{bmatrix} \underline{\ddot{w}} \\ \underline{\ddot{\theta}} \\ \underline{\dot{w}} \\ \underline{\dot{\theta}} \end{bmatrix} = \hat{\mathbf{M}} \begin{bmatrix} C_{aero} \begin{bmatrix} -k_w & 0 \\ 0 & -k_\theta \end{bmatrix} + K_{aero} \\ \begin{bmatrix} 1 & 0 \\ 0 & 1 \end{bmatrix} \begin{bmatrix} 0 & 0 \\ 0 & 0 \end{bmatrix} \end{bmatrix} \begin{bmatrix} \underline{\dot{w}} \\ \underline{\dot{\theta}} \\ \underline{w} \\ \underline{\theta} \end{bmatrix} + \hat{\mathbf{M}} \begin{bmatrix} qS_w C_{L_\alpha} \\ aqS_w C_{L_\alpha} \\ 0 \\ 0 \end{bmatrix} \alpha + \hat{\mathbf{M}} \begin{bmatrix} qS_w C_{L_{\delta_c}} \\ aqS_w C_{L_{\delta_c}} \\ 0 \\ 0 \end{bmatrix} \delta_c \quad (3.27)$$

where  $\hat{\mathbf{M}}$  is the inverse generalized mass matrix and is given by:

$$\hat{\mathbf{M}} = \begin{bmatrix} \begin{bmatrix} M & S \\ S & I_\theta \end{bmatrix}^{-1} \begin{bmatrix} 0 & 0 \\ 0 & 0 \end{bmatrix} \\ \begin{bmatrix} 0 & 0 \\ 0 & 0 \end{bmatrix} \begin{bmatrix} 1 & 0 \\ 0 & 1 \end{bmatrix} \end{bmatrix} \quad (3.28)$$

The mathematical models for the aerodynamics and wing structure have been formulated leading to a complete aeroelastic model in state space form.

## 4 Verification and Validation

This chapter describes the verification and validation of the aerodynamic and aeroelastic models presented in Chapter 3.

Section 4.1 analyses the aerodynamic model in terms of lift distribution, discretization, longitudinal and lateral aerodynamics.

Section 4.2 analyses the structural model by comparing the discrete and continuous models of a uniform cantilever beam.

### 4.1 Aerodynamic Model

In order to calculate aerodynamic forces and moments it is necessary to define a flight state. As described in Section 2.2, the flight state is chosen to be steady, straight and level, high AoA flight corresponding to segment 1 of the RCAM evaluation trajectory (see Appendix F).

The dimensions and weight and balance properties of the aircraft used for the aerodynamic calculations are presented in Appendices C and D respectively. At the altitude of 1000  $m$  defined for segment 1 of the RCAM evaluation trajectory the atmospheric density is  $\rho = 1.112 \text{ kg/m}^3$ . The angle of attack  $\alpha$  and elevator deflection  $\delta_e$  required to maintain straight and level flight are determined from equilibrium as follows:

$$\begin{bmatrix} C_{L_\alpha} & C_{L_{\delta_e}} \\ C_{m_\alpha} & C_{m_{\delta_e}} \end{bmatrix} \begin{bmatrix} \alpha \\ \delta_e \end{bmatrix} = \begin{bmatrix} \frac{mg}{qS_w} - C_{L_0} \\ -C_{m_0} \end{bmatrix} \quad (4.1)$$

Tornado was used to calculate the coefficients:  $C_{L_0} = 0.1733$ ,  $C_{m_0} = 0.03403$ ,  $C_{L_\alpha} = 5.644$ ,  $C_{m_\alpha} = -2.558$ ,  $C_{L_{\delta_e}} = 0.7230$  and  $C_{m_{\delta_e}} = -2.351$ .

The trimmed flight state is then represented in terms of the variables required by the aerodynamic model implementation which are shown in Table 4.1.

Table 4.1: Definition of the flight state for verification and validation

Parameter	Value
$m$	6895 kg
$h$	1000 m
$V$	58 m/s
$\alpha$	10.39 °
$\beta$	0.000 °
$p$	0.000 °/s
$q$	0.000 °/s
$r$	0.000 °/s
$\delta_e$	-10.48 °
$\delta_c$	0.000 °
$\delta_r$	0.000 °

#### 4.1.1 Lift Distribution

In order to evaluate the shape and magnitude of the lift distribution along the wing span, the lift coefficient per unit span of each wing strip is plotted against its spanwise position (in % of semi-span) in Figure 4.1. The lift coefficient of each strip was extracted from Tornado’s internal data structures.

The lift coefficient shown in each label is calculated from the area under each curve. The line of an ideal elliptical lift distribution is included for reference purposes (the lift coefficient of the elliptical distribution is made equal to the lift coefficient of the published curve which was obtained from the manufacturer’s data provided by (Tuzcu, 2001)). The figure shows that the line of the predicted lift distribution lies close to the published data and has an elliptical shape except near the fuselage. This is the expected result and verifies the implementation of the Tornado model.

The NACA 23012 has  $C_{L_{max}} = 1.8$  and Figure 4.1 confirms that this is not exceeded at any point and therefore the aircraft is below the stall AoA.

An evaluation of the quality of the fit is gained by comparing the lift coefficient of each of the curves. The lift coefficient of the Tornado curve is 5% greater than under the curve representing the manufacturer’s data. Of this 5%, 4% lies along the region of the curve close to the fuselage (0 - 50% of the wing semi-span). The flexible Tornado model appears to overpredict the amount of lift generated by the part of the wing that coincides with the fuselage. There are a number of reasons for Tornado to overpredict the lift in this region:



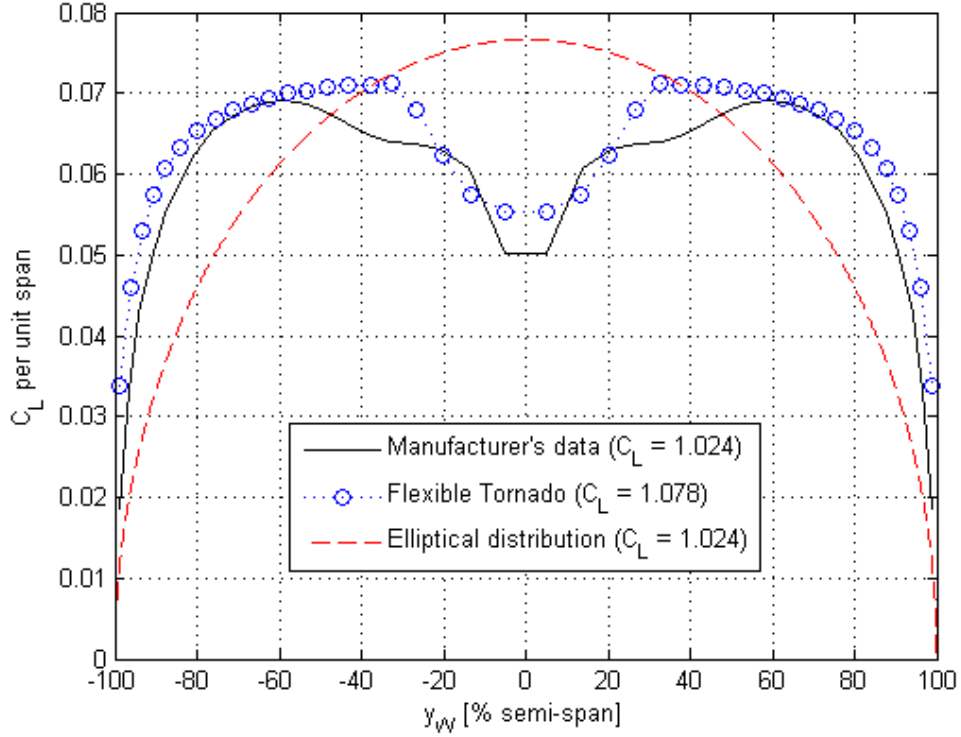


Figure 4.1: Lift distribution along the wing span, calculated at the steady, trimmed flight state of  $h = 1000 \text{ m}$ ,  $V = 58 \text{ m/s}$ ,  $\alpha = 10.39^\circ$

- Tornado models the fuselage as two flat plates perpendicular to each other (Melin, 2000). Although the vertical flat plate does not make a contribution, the lift generated by the horizontal flat plate is greater than that of a cylinder with its axis aligned with the flow.
- There is a loss of lift generation in the region of the intersection between the wing and fuselage. Figure 4.1 shows that although the reduction in lift in the intersection region is correctly predicted, both the magnitude of the reduction and the span over which it occurs is smaller than expected.

Due to the shorter moment arms of the inboard wing sections, the error will have little effect on the accuracy of the roll authority precision and is therefore acceptable. The error along the outboard section of the wing (50 - 100% of the wing semi-span) accounts for the remaining 1% and can be attributed to the difference between the first order modelling method being applied here and the experimental methods used by the manufacturer to obtain the reference data.

### 4.1.2 Discretization

The lift distribution is also used to investigate the optimum number of panels for discretization of the wing by plotting the error between the Tornado and the manufacturer's data published by Tuzcu, (2001) for lift coefficients.

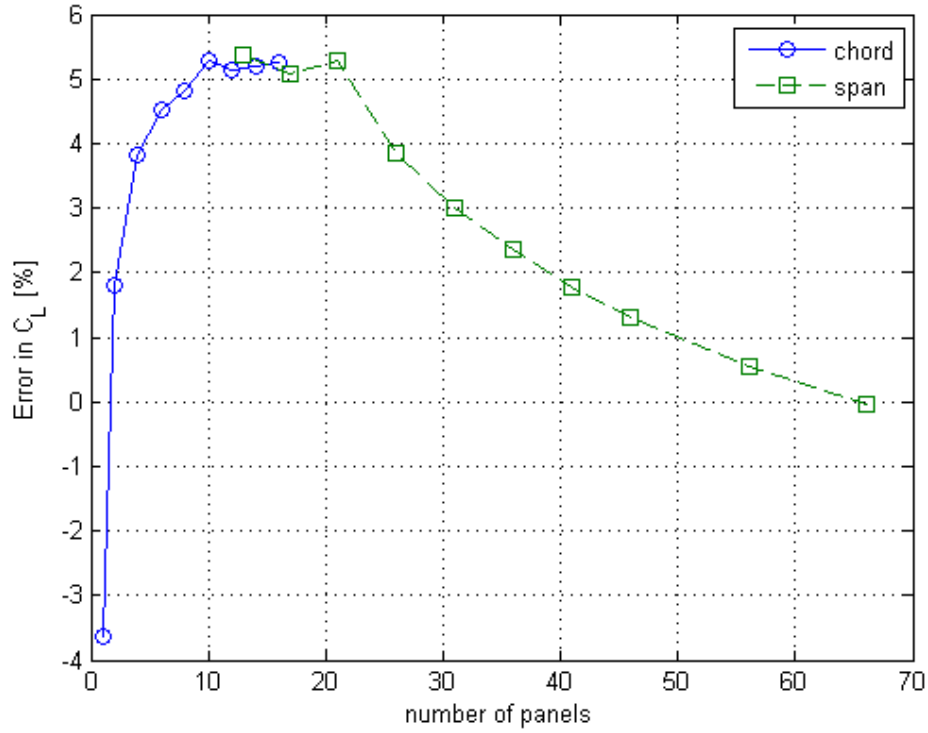


Figure 4.2: Error between the lift coefficient predicted by the discrete model in Tornado and the manufacturer's data; plotted as separate curves for variation in the number of panels along the chord and the span

Figure 4.2 shows one curve obtained by varying the number of panels in the chord-wise direction while holding the number of panels along the span at 21. The curve shows that the error tends to a constant value of 5% as the degree of discretization along the chord increases. This result shows that selecting a chord-wise discretization of 10 panels yields an acceptable resolution with no appreciable gain in accuracy at higher resolutions. Note that increasing the accuracy by reducing the number of panels along the chord will not have the desired effect because then the resolution will be insufficient to model the variable cambered actuation.

Figure 4.2 shows a second curve obtained by varying the number of panels in the span-wise direction while holding the number of panels along the chord at 10. The error tends towards 0% as the degree of discretization along the span increases.

Although the curve clearly shows that it would be possible to achieve the greatest accuracy when using 66 or more panels along the span, limitations in the available computing power (a 32 bit computer with 4 GB of memory does not have sufficient memory for Tornado to generate a solution to a wing with 76 panels along the span) meant that Tuzcu's (2001) selection of 21 panels was reused in this work because the corresponding error of 5% is acceptable for a first order model.

#### 4.1.3 Longitudinal Aerodynamics

The aircraft longitudinal aerodynamics are compared to the manufacturer's data published by Tuzcu, (2001) in order to validate the Tornado model and identify any discrepancies which may affect the analysis of the variable camber wing aerodynamics. Appendix E shows how the reference longitudinal aerodynamic coefficients are built up using the published discretized force coefficients of the fuselage, wing, horizontal tail, elevator and engines.

Figure 4.3 shows the lift curve of the wing compared to the published data and the NACA23012 airfoil. The discrete model is within 1% of the published data which further confirms that the code can accurately predict the lift and lift curve slope. The discrete model is only capable of predicting the linear part of the lift curve slope and is not capable of predicting  $C_{L_{max}}$ . Therefore the model is only applicable up to the AoA at which the airfoil  $C_{L_{max}}$  occurs, ie.  $\alpha_{stall} = 18^\circ$ .

Figure 4.4 shows the pitching moment curve of the wing compared to the published data and the NACA23012 airfoil. The sign of the gradient of the pitching moment curve predicted by Tornado is correct but it is much steeper than both the NACA23012 and published data. The most likely reason for this is a mismatch in reference points about which the pitching moment is calculated. The NACA23012 data is calculated about the airfoil AC and this is clearly demonstrated by the fact that it is independent of AoA up to the stall. Abbott and von Doenhoff, (1959) show that the pressure distribution of the NACA 5 Series airfoils beginning with 230 has the largest pressure ratio in front of the AC (0%-20% of the chord). Therefore as the reference point moves forward of the AC,  $C_{m_\alpha}$  will become more negative and vice versa as the reference point moves behind the AC. Therefore the reference point for the published data does not coincide with the wing AC but lies in front of it and closer to it than the reference point for the discrete wing. The reference point for the discrete wing is 25% of the wing MAC and this analysis shows that the actual wing AC lies behind this which can be attributed to the fact that the wing is not a conventional straight tapered wing. The error in location of the discrete wing AC

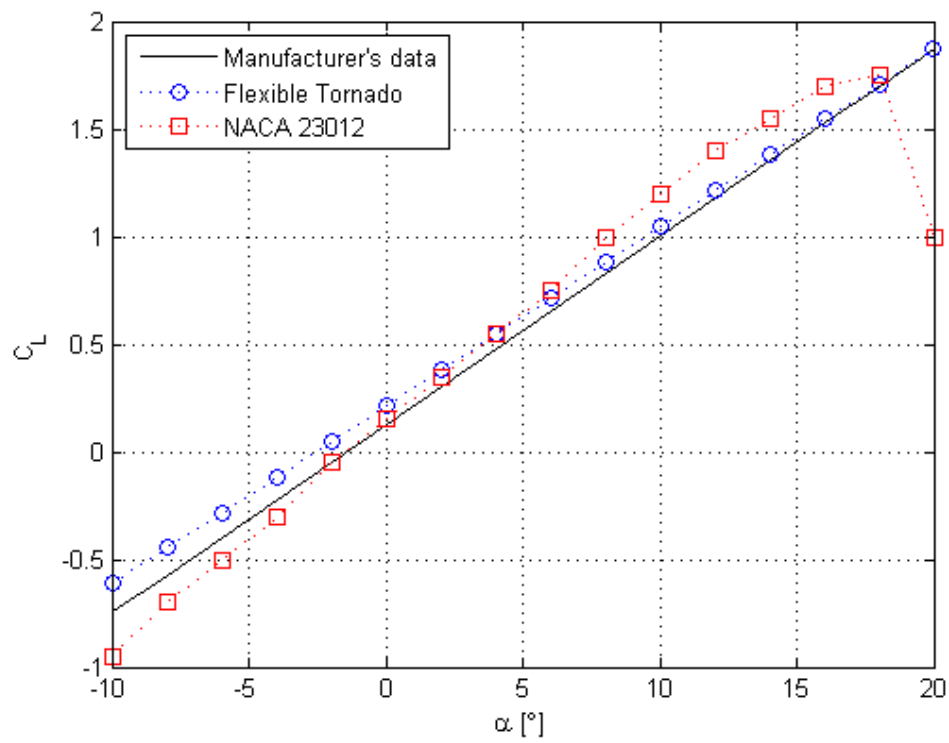


Figure 4.3: Wing lift coefficient as a function of  $\alpha$  for the flexible model implemented in Tornado compared to both the manufacturer's data and published wind tunnel test results for the NACA23012 airfoil

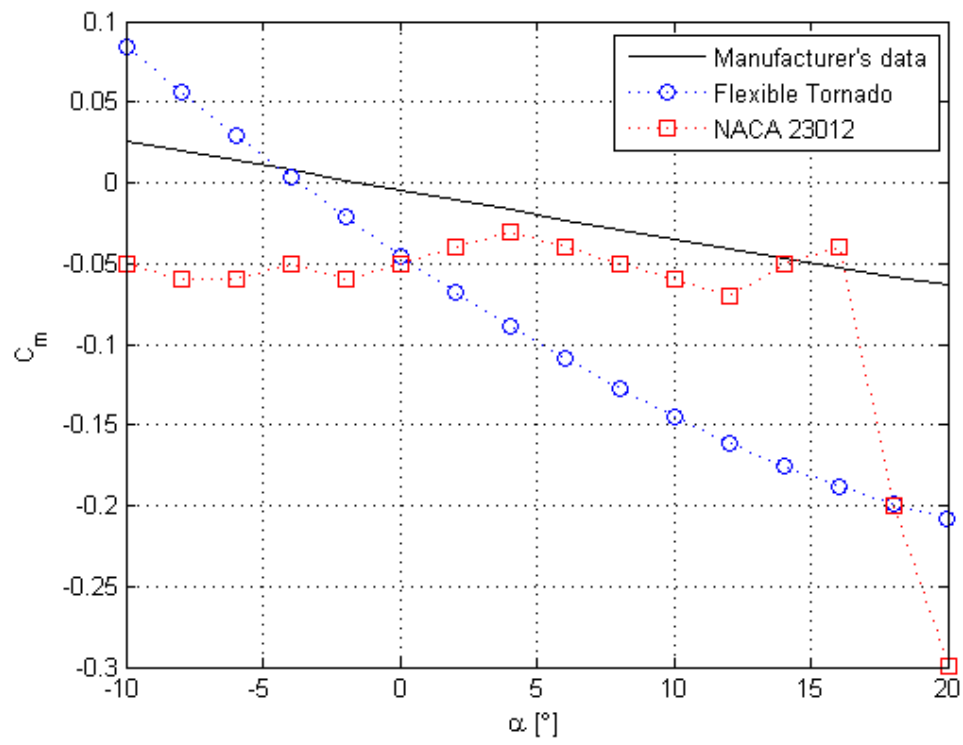


Figure 4.4: Wing pitching moment coefficient as a function of  $\alpha$  for the flexible model implemented in Tornado compared to both the manufacturer's data and published wind tunnel test results for the NACA23012 airfoil

needs to be accounted for in all calculations that use this as a reference point.

The derivatives in Table 4.2 were obtained at the flight state shown in Table 4.1 by using Tornado to sweep  $\alpha$  from  $-10^\circ$  to  $20^\circ$  and the elevator through its published range of motion:  $\delta_e$  from  $-22^\circ$  to  $15^\circ$  (Cessna Aircraft Company, 1989).  $C_{L_0}$  and  $C_{m_0}$  were determined by inspecting the resulting plots of  $C_L$  and  $C_m$  vs  $\alpha$ .  $C_{L_{\delta_e}}$

Table 4.2: Longitudinal aerodynamic results

Static derivative	Published	Model	Error [%]
$C_{D_0}$	$9.600 \times 10^{-2}$	-	-
$C_{L_0}$	$1.519 \times 10^{-1}$	$1.733 \times 10^{-1}$	14.1
$C_{L_\alpha} [rad^{-1}]$	5.717	5.644	-1.3
$C_{L_{\delta_e}} [rad^{-1}]$	$2.012 \times 10^{-1}$	$7.230 \times 10^{-1}$	259.4
$C_{m_0}$	$1.005 \times 10^{-1}$	$3.403 \times 10^{-2}$	-66.1
$C_{m_\alpha} [rad^{-1}]$	-1.840	-2.558	39.0
$C_{m_{\delta_e}} [rad^{-1}]$	$-6.959 \times 10^{-1}$	-2.351	237.8

and  $C_{m_{\delta_e}}$  show large errors; 260% and 238% respectively. It is suspected that this is not due to the fidelity of the Tornado model but is instead due to an error in the horizontal tail reference area in the published data. This statement can be justified with the following analysis: substituting the data from column 1 of Table 4.2 yields a trim AoA of  $9.776^\circ$  as opposed to using the data from column 2 which yields  $10.38^\circ$ . These two angles of attack are less than  $1^\circ$  apart and, together with the small 1.3% error in  $C_{L_\alpha}$ , confirm that the amount of lift generated by the wing is being correctly predicted by Tornado. However, using the published data, the elevator deflection required to trim is  $-17.52^\circ$  as opposed to the Tornado predicted value of  $-10.47^\circ$ . The elevator only has a deflection range of  $-22^\circ$  to  $15^\circ$  (Cessna Aircraft Company, 1989) and, while a large deflection is expected during low speed flight,  $-17.52^\circ$  leaves little additional travel of the elevator for further maneuvering such as flare during landing. Fortunately, this does not have any effect on the model, nor on the results of this investigation. The source of this error is not pertinent to the current study and has not been explored further.

#### 4.1.4 Lateral Aerodynamics

The aircraft lateral aerodynamics are compared to the manufacturer's data published by Tuzcu, (2001) in order to validate the Tornado model and identify any discrepancies which may affect the analysis of the variable camber wing aerodynamics. Appendix E shows how the reference lateral aerodynamic coefficients are built

up using the published discretized force coefficients of the fuselage, vertical tail, ailerons and rudder.

The derivatives in Table 4.3 were obtained at the flight state shown in Table 4.1 by using Tornado to sweep  $\beta$  from  $-10^\circ$  to  $10^\circ$  and the control surfaces through their published range of motion:  $\delta_a$  from  $-25^\circ$  to  $25^\circ$  and  $\delta_r$  from  $-22^\circ$  to  $22^\circ$  (Cessna Aircraft Company, 1989). A detailed analysis of the results presented in Table 4.3 is

Table 4.3: Lateral aerodynamic results

Static derivative	Published	Model	Error [%]
$C_{Y_\beta} [rad^{-1}]$	$-2.677 \times 10^{-1}$	$-1.630 \times 10^{-1}$	-39.1
$C_{Y_{\delta_r}} [rad^{-1}]$	$9.870 \times 10^{-2}$	$1.160 \times 10^{-1}$	17.6
$C_{\ell_\beta} [rad^{-1}]$	$-3.277 \times 10^{-2}$	$-5.519 \times 10^{-2}$	68.4
$C_{\ell_{\delta_a}} [rad^{-1}]$	$-1.415 \times 10^{-1}$	$-1.729 \times 10^{-1}$	22.2
$C_{\ell_{\delta_r}} [rad^{-1}]$	$1.354 \times 10^{-2}$	$1.332 \times 10^{-2}$	-1.6
$C_{n_\beta} [rad^{-1}]$	$7.028 \times 10^{-2}$	$7.721 \times 10^{-2}$	9.9
$C_{n_{\delta_a}} [rad^{-1}]$	$-2.592 \times 10^{-2}$	$-2.254 \times 10^{-2}$	-13.0
$C_{n_{\delta_r}} [rad^{-1}]$	$-4.144 \times 10^{-2}$	$-5.443 \times 10^{-2}$	31.4

obtained with reference to Melin,'s (2000) dissertation describing the experimental results and validity of the Tornado coefficients:

- In the prediction of  $C_{Y_\beta}$ , the modelling of the fuselage has a large impact because it affects the surface area and hence how much side force is generated (Melin, 2000). Therefore the error can be attributed to the area of the vertical fuselage in the discrete model being too small.
- Melin, (2000) shows that the prediction of  $C_{Y_{\delta_r}}$  should be more accurate. Therefore the over prediction is attributed to the area of the rudder in the discrete model being too large.
- Melin, (2000) confirms a poor correlation for  $C_{\ell_\beta}$  which can be attributed to differences in the  $z$  location of the reference point. Note that the published value only accounts for the moment generated by the offset of the vertical tail aerodynamic centre with respect to the roll axis and does not include dihedral and sweep effects.
- Melin, (2000) confirms an over prediction of the aileron effectiveness coefficient  $C_{\ell_{\delta_a}}$ . However, the error is sufficiently small that this result is considered a reasonable baseline for comparison with the variable camber wing because the

error shown here is likely to also be present in the variable camber results and therefore the delta between the two sets of results will be negligible.

- The prediction of  $C_{\ell_{\delta_r}}$  is accurate. This can be attributed to minimal coupling of the aileron deflection with the yawing moment.
- The error in  $C_{n_\beta}$  is relatively small and is also shown to be over predicted by Melin, (2000) who attributes it to fuselage and thickness effects.
- The error in  $C_{n_{\delta_a}}$  is relatively small and is also shown to be under predicted by Tornado due to a lack of stabilizing moment from the fuselage (Melin, 2000).
- Melin, (2000) confirms an over prediction of the rudder effectiveness coefficient  $C_{n_{\delta_r}}$  which is due to a combination of fuselage effects and the large rudder area discussed above.

The overall performance of the discrete aerodynamic model is acceptable for this work in which the main focus lies on the lift generated by the variable camber wing.

This lift is shown to be well predicted for a rigid wing and therefore, due to the assumption made in Section 2.1 that the camber control mechanism can be assumed to be rigid, the results are sufficiently accurate for use in analysis of the variable camber wing longitudinal dynamics as long as the error in reference points is considered when evaluating the pitching moment. All subsequent aerodynamic analysis is based on the variable camber wing being rigidly fixed at a specific camber setting and therefore effectively being a rigid wing.

Based on the above analysis, the smaller the AoA, the smaller the influence of the error in  $C_m$  and the more accurate the results. The lateral dynamics that are not affected by the fuselage are also shown to be sufficiently accurate for use in analysis of the variable camber wing lateral dynamics. However, the sideslip angle  $\beta$  must be kept to a minimum because of the large errors in  $C_{Y_\beta}$  and  $C_{\ell_\beta}$ .

## 4.2 Structural Model

This section presents the verification of the wing structural model parametrized as a uniform cantilever beam. The following terminology is used:

- reference cantilever beam - continuous uniform cantilever beam



- discrete cantilever beam - structural model presented in Section 3.3 parametrized as a uniform cantilever beam

Equation (3.18) was parametrized as a uniform cantilever beam with a constant rectangular cross section and structural stiffness equal to the wing at the mean aerodynamic chord. The polar moment of inertia of the cross section,  $I$ , was calculated for a rectangular beam having chord  $\bar{c}$ , a thickness equal to the airfoil thickness and moment of inertia (MOI)  $I_{yy}$  all calculated at the wing MAC. Reference models of a uniform cantilever beam undergoing pure bending and torsion vibrations were obtained from Rao, (1995) and used to verify the model. The data used for verification is shown in Table 4.4.

Table 4.4: Parameters defining the cantilever beam

Parameter	Value
Moment of inertia about elastic axis ( $I_{yy}$ )	$4.752 \text{ kg.m}^2$
Flexural Stiffness ( $EI$ )	$5.883 \times 10^6 \text{ N.m}^2$
Torsional Stiffness ( $GJ$ )	$8.587 \times 10^6 \text{ N.m}^2$
Polar moment of inertia per unit span ( $I_o$ )	$998.8 \text{ kg.m}$
Static mass moment about elastic axis ( $S_{ea}$ )	$0.6832 \text{ m}^3$
Material density ( $\rho$ )	$4.048 \times 10^2 \text{ kg/m}^3$
Semi-span ( $s$ )	$8.510 \text{ m}$
Cross-sectional area ( $A$ )	$3.206 \times 10^{-1} \text{ m}^2$
Mass ( $m$ )	$5.918 \times 10^2 \text{ kg}$

For the discrete model, the output matrix  $\mathbf{C}$  in Equation (3.26b) is set up to extract  $w$  and  $\hat{\theta}$  from the state vector as follows:

$$\mathbf{C} = \begin{bmatrix} 0 & 0 & 1 & 0 \\ 0 & 0 & 0 & 1 \end{bmatrix} \quad (4.2)$$

The set of discrete  $y$  coordinates corresponds to the span-wise ( $y_W$ ) location of the centroid of each strip. This set of  $y$  coordinates is given in the first column of Table B.1 in Appendix B.

#### 4.2.1 Reference Cantilever Beam

The continuous model of a cantilever beam in bending and torsion as presented by Rao, (1995) is based on Euler-Bernoulli beam theory and assumes a uniform beam in order to simplify the problem. The free vibration solution is based on the principle

of separation of variables for which a set of assumed mode shapes is combined with a general harmonic function. A brief overview of the model and the relevant aspects of its implementation is presented here.

Figure 4.5 shows a cantilever beam in bending. The expression for the free lateral

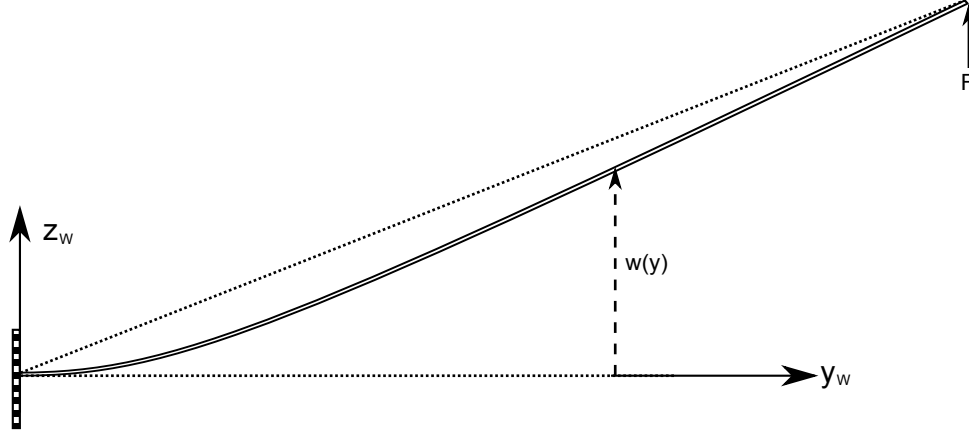


Figure 4.5: Deflection of a cantilever beam in bending with a point force  $F$  applied to the free end

vibration of the cantilever beam is given by Equation (4.3) (Rao, 1995).

$$w(y, t) = \sum_{n=1}^{\infty} W_n(y) (A_n \cos \omega_n t + B_n \sin \omega_n t) \quad (4.3)$$

$A_n$  and  $B_n$  are constants calculated from the initial conditions.  $W_n(y)$  is the  $n^{th}$  normalized bending mode shape of the beam and is given by Equation (3.12) in which each mode shape is defined by the variables  $\zeta s$ . In order to identify effects from higher modes that may be missing from the discrete model developed in Section 3.3, the first four mode shapes are included in the continuous model. The first mode shape has already been given in Section 3.3 as  $\zeta_1 s = 1.875104$ . The second, third and fourth mode shapes are given by  $\zeta_2 s = 4.694091$ ,  $\zeta_3 s = 7.854757$  and  $\zeta_4 s = 10.995541$  (Rao, 1995):

$\omega_n$  is the natural frequency of vibration corresponding to the  $n^{th}$  mode shape and is given by Equation (4.4) (Rao, 1995):

$$\omega_n = (\zeta_n s)^2 \sqrt{\frac{EI}{\rho A s^4}} \quad (4.4)$$

Figure 4.6 shows a cantilever beam in torsion. The expression for the free torsional vibration of a cantilever beam is of the same form as Equation (4.3) and is given by

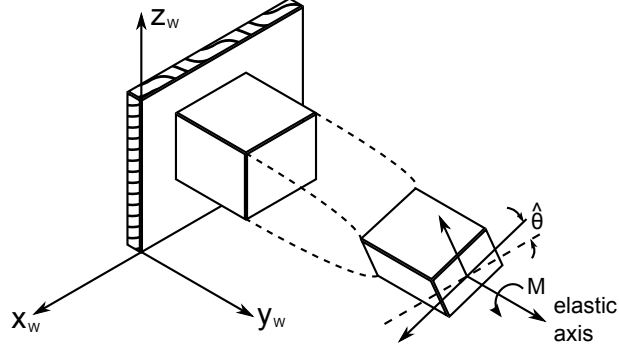


Figure 4.6: Twist of a cantilever beam in torsion with a moment  $M$  applied to the free end

Equation (4.5) (Rao, 1995).

$$\hat{\theta}(y, t) = \sum_{n=1}^{\infty} H_n(y) (C_n \cos \omega_n t + D_n \sin \omega_n t) \quad (4.5)$$

$C_n$  and  $D_n$  are constants calculated from the initial conditions.  $H_n(y)$  is the  $n^{th}$  normalized torsion mode shape of the beam and is given by an extended form of (3.14) to account for higher modes:

$$H_n(y) = \sin \frac{(2n+1)\pi y}{2s} \quad (4.6)$$

$\omega_n$  is the natural frequency of vibration corresponding to the  $n^{th}$  mode shape and is given by Equation (4.7) (Bismarck-Nasr, 1999):

$$\omega_n = \frac{(2n-1)\pi\gamma}{2s}, \quad n = 1, 2, 3, \dots \quad (4.7)$$

where:

$$\gamma = \sqrt{\frac{GJ}{I_o}} \quad (4.8)$$

where  $I_o = \frac{I_{xx} + I_{zz}}{s}$  is the mass polar moment of inertia of the beam per unit length. These equations are implemented in MATLAB and parametrized using Table 4.4 in order to obtain the free vibration responses in bending and torsion.

#### 4.2.2 Static Deflections and Initial Conditions

In order to analyse the static deflections of the reference and discrete cantilever beams, point loads of  $F = 1000 \text{ N}$  and  $M = 1000 \text{ Nm}$  are applied at the free end. Note that in Equation (3.18) the stiffness matrix is decoupled and therefore the

static bending and torsion deflections are independent of each other. This means that the point loads can be applied simultaneously without affecting the results. The static deflections of the discrete cantilever beam are calculated using Equation (3.18) with  $\ddot{w} = 0$  and  $\ddot{\theta} = 0$  and  $Q_w = F = 1000 \text{ N}$  and  $Q_\theta = M = 1000 \text{ Nm}$ . The static deflections are then used as initial conditions when evaluating the free responses.

## Bending

The static bending deflection of a continuous uniform cantilever beam with a point force  $F$  applied to the end is given by (Hibbeler, 2000):

$$w(y) = \frac{F}{EI} \left( \frac{s}{2} y^2 - \frac{1}{6} y^3 \right) \quad (4.9)$$

The static bending deflection of the discrete cantilever beam is compared to the reference cantilever beam in Figure 4.7. The figure shows that the shapes are the

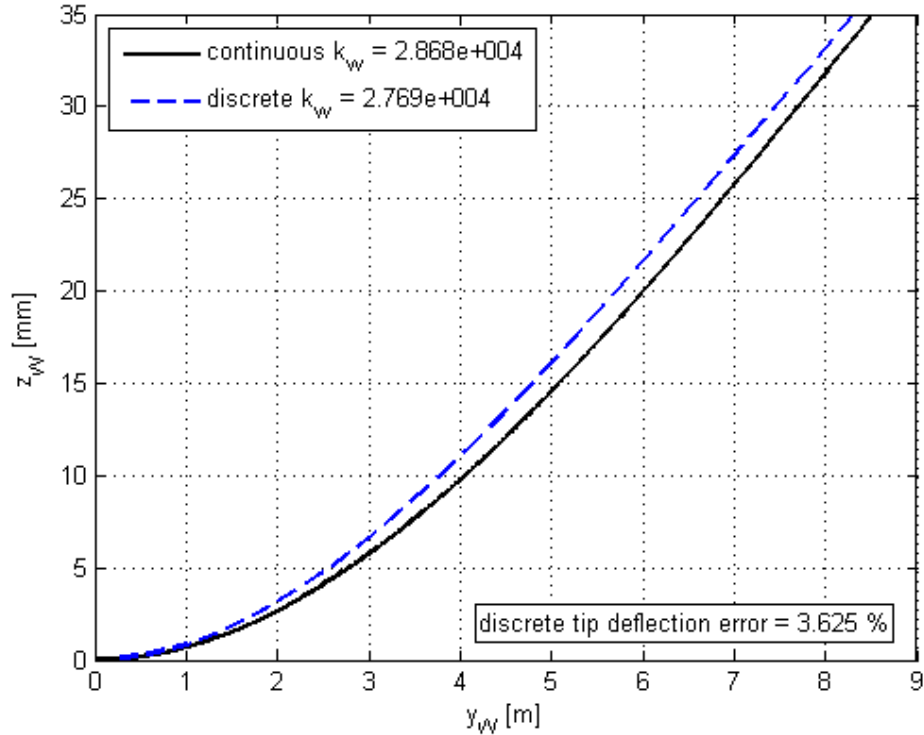


Figure 4.7: Static deflection of the discrete cantilever beam compared to a continuous cantilever beam when a point force of 1000 N is applied to the free end

same which shows how well the expression for the mode shape (Equation (3.12)) approximates the expression for the static deflection of a continuous uniform beam

(Equation (4.9)). The error in the tip deflection between the discrete and continuous cantilever beams is a result of the discretization which causes the effective stiffness of the discrete model to be less than the continuous model.

To complete the definition of the initial conditions, the derivative of Equation (4.3) is taken with respect to time in order to obtain an expression for the velocity which is then set equal to zero at  $t = 0$  as follows:

$$\frac{dw}{dt}(s, 0) = \sum_{n=1}^{\infty} W_n(y) B_n \omega_n = 0 \quad (4.10)$$

Therefore  $B_n = 0$  and Equation (4.3) reduces to:

$$w(y, t) = \sum_{n=1}^4 W_n(y) A_n \cos \omega_n t \quad (4.11)$$

$A_n$  is calculated using the initial static displacements of  $n$  arbitrary points on the beam which yields a set of  $n$  equations in  $n$  unknowns:

$$\sum_{n=1}^{\infty} W_n(y) A_n = \frac{F}{EI} \left( \frac{s}{2} y^2 - \frac{1}{6} y^3 \right) \quad (4.12)$$

## Torsion

The static twist of a continuous uniform cantilever beam with a constant torque  $M$  applied to the end is given by (Hibbeler, 2000):

$$\hat{\theta}(y) = \frac{My}{GJ} \quad (4.13)$$

The static twist (in *mrad*) of the discrete cantilever beam is compared to the reference cantilever beam in Figure 4.8. The figure shows that the shapes are not the same: the discrete cantilever beam shows the assumed mode shape (Equation (3.14)) while the continuous cantilever beam shows the straight line that is the expression for the static twist given by Equation (4.13). Figure 4.8 also shows a large error in the tip deflection which is caused by the large difference in effective stiffnesses. Both of these errors are caused by the use of Equation (4.13) from Hibbeler, (2000) which assumes a beam with a circular cross-section. Since this is obviously not the case for the beam under consideration, the shear stress will be distributed over the cross-section in a very complex manner and it will deform as it twists. Therefore, the mode shape given by Bismarck-Nasr, (1999) is assumed to be a better approximation of the actual wing twist than the linear function given by (Hibbeler, 2000). This is supported by Hibbeler,'s (2000) statement that a shaft with a circular cross-section is the most efficient, i.e. it has the smallest angle of twist for a given input moment.

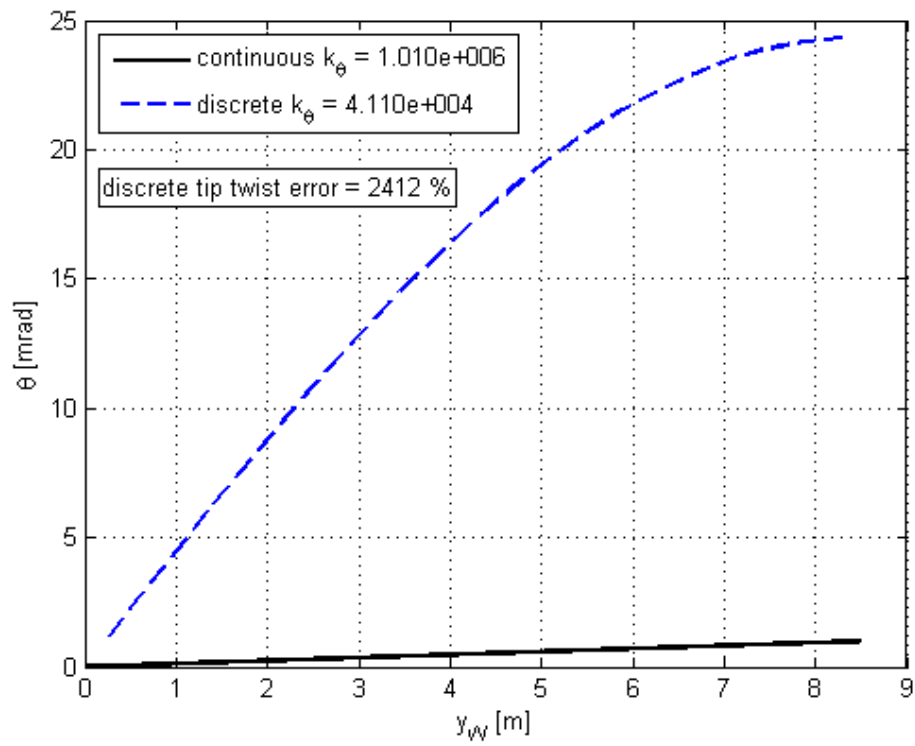


Figure 4.8: Static twist of the discrete cantilever beam compared to a continuous cantilever beam when a moment of 1000  $Nm$  is applied to the free end

Note also that if the static twist is assumed to be linear then  $H(y) = y$  and its second derivative with respect to  $y$  in Equation (3.22b) is zero leading to  $k_\theta = 0$  which is impossible. Therefore the linear expression for static twist (Equation (4.13)) is not valid for the cantilever beam. Finally, note that as long as the initial conditions are static, the analysis of the beam dynamics will not be affected because the initial condition specifies only the angle of twist of the end of the beam.

It can be argued that it would be better to parameterize the discrete model with a circular cross-section instead of a rectangular one in order to get a more meaningful comparison against which to verify the torsion model. However, while it would provide verification for this one unique case, it is not needed because it does not contribute to the interpretation of the results obtained for the discrete wing model. This research does not consider or analyze any results from a geometry with a circular cross-section and therefore verification of the discrete model parameterized as such is not needed to fulfill the objectives.

To complete the definition of the initial conditions, the derivative of Equation (4.5) is taken with respect to time in order to obtain an expression for the velocity which is then set equal to zero at  $t = 0$  as follows:

$$\frac{d\hat{\theta}}{dt}(s, 0) = \sum_{n=1}^{\infty} H_n(y) D_n \omega_n = 0 \quad (4.14)$$

Therefore  $D_n = 0$  and Equation (4.5) reduces to:

$$\hat{\theta}(y, t) = \sum_{n=1}^4 H_n(y) C_n \cos \omega_n t \quad (4.15)$$

$C_n$  is calculated using the initial static displacements of  $n$  arbitrary points on the beam which yields a set of  $n$  equations in  $n$  unknowns.

$$\sum_{n=1}^{\infty} H_n(y) C_n = \frac{My}{GJ} \quad (4.16)$$

### 4.2.3 Mode Shape and Natural Frequency

The first four bending and torsion mode shapes of the cantilever beam are generated using Equations (3.12) and (4.6) respectively. The natural frequency of each of the first four mode shapes is calculated using Equations (4.4) and (4.7) together with the data in Table 4.4.

Figure 4.9 shows the mode shape corresponding to each of the first four bending natural frequencies. The typical range for the first few bending modes of a light

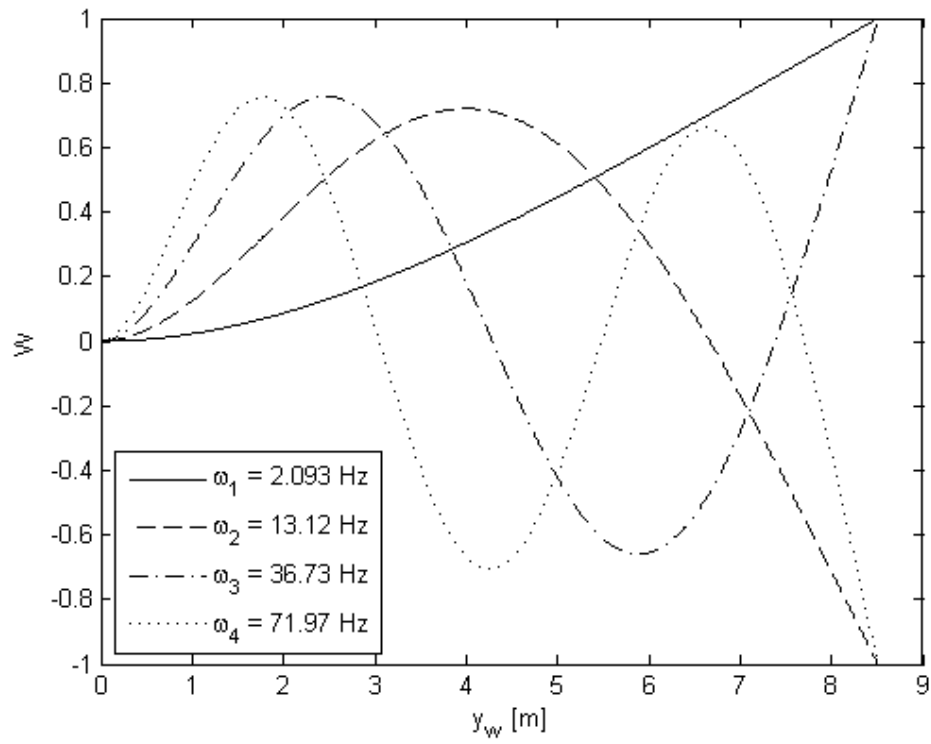


Figure 4.9: First four bending mode shapes and natural frequencies of the reference uniform cantilever beam model (Equations (3.12) and (4.4)) parameterized as per Table 4.4



passenger jet aircraft structure are given by Smith and Shust, (2004) as 4 - 20 Hz. Figure 4.9 shows that the first two bending modes fall within this range. This demonstrates the applicability of the continuous beam model for use in verifying the discrete wing model in bending.

Figure 4.10 shows the mode shape corresponding to each of the first four torsion natural frequencies. The typical range for the first few torsion modes of a light

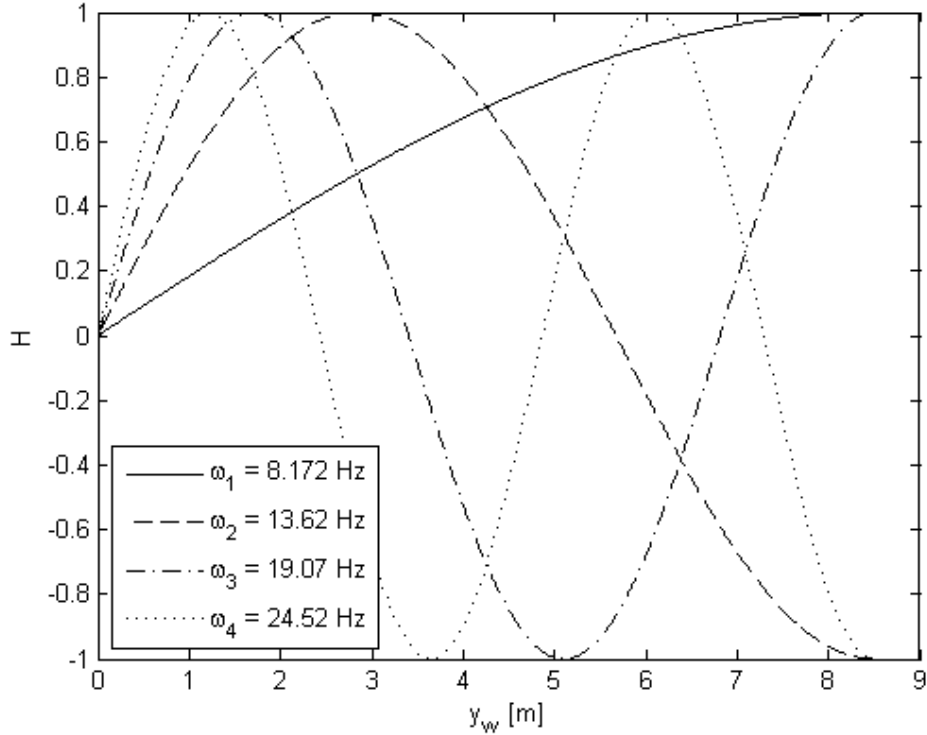


Figure 4.10: First four torsion mode shapes and natural frequencies of the reference uniform cantilever beam model (Equations (4.6) and (4.7)) parameterized as per Table 4.4

passenger jet aircraft structure are given by Smith and Shust, (2004) as 4 - 20 Hz. The first three torsion modes of the beam fall within this range. This demonstrates the applicability of the continuous beam model for use in verifying the discrete wing model in torsion.

#### 4.2.4 Free Response

In order to verify the free response of the discrete cantilever beam, first the decoupled ( $S = 0$ ) and then the coupled responses of the free end are compared to the response of the reference cantilever beam described in Section 4.2.1 (which is

inherently decoupled). Both the reference and discrete models are initialized at the same initial conditions corresponding to the static deflection of the free end of a continuous uniform beam as given by Equations (4.9) and (4.13).

The bending vibration of the free end of the discrete (decoupled and coupled) and reference cantilever beams are plotted in Figure 4.11. The figure shows that the

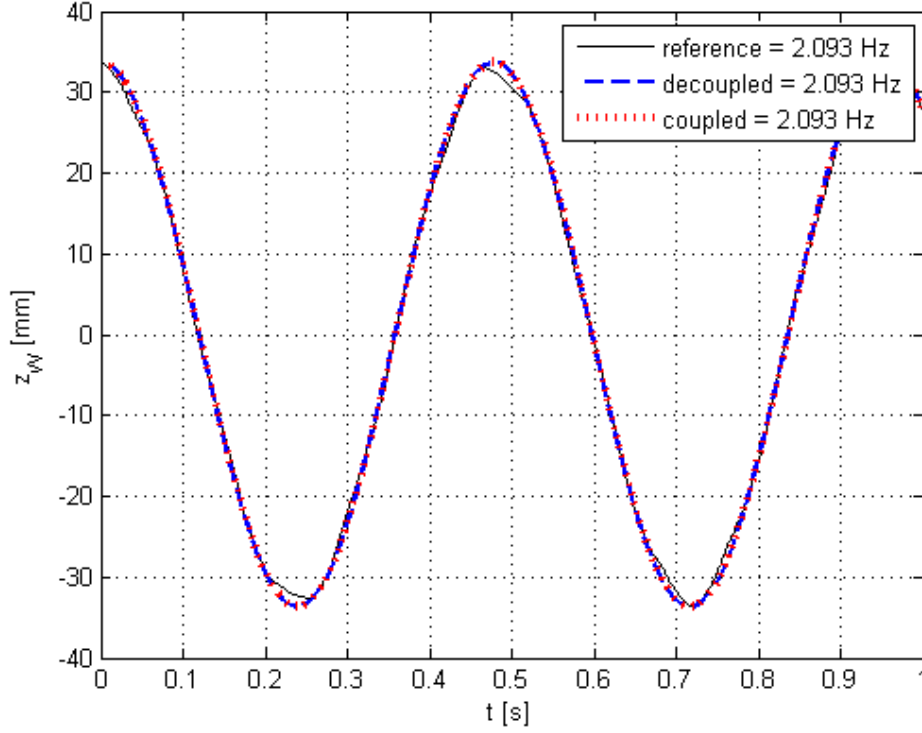


Figure 4.11: Comparison between the bending responses of the reference and discrete cantilever beam models (with and without the presence of cross-coupling terms in the mass matrix) in response to an initial bending deflection

natural frequency of the decoupled discrete model is effectively equal to that of the first mode shape of the reference beam shown in Figure 4.9. This is an excellent verification of the discrete implementation and further verifies the correlation shown in the static deflection (Figure 4.7). Figure 4.11 also shows that the effect of the torsion mode coupling with the bending dynamics is negligible. This is primarily due to the relatively small magnitude of the angular response which, when multiplied by the coupling term  $S$  in the mass matrix in Equation (3.18), effectively vanishes when compared to the magnitude of the bending response.

The torsion vibration of the free end of the discrete (decoupled and coupled) and reference cantilever beams are plotted in Figure 4.12. Note that the y axis in Figure 4.12 has units of  $mrad$ . The figure shows that the natural frequency of the decoupled

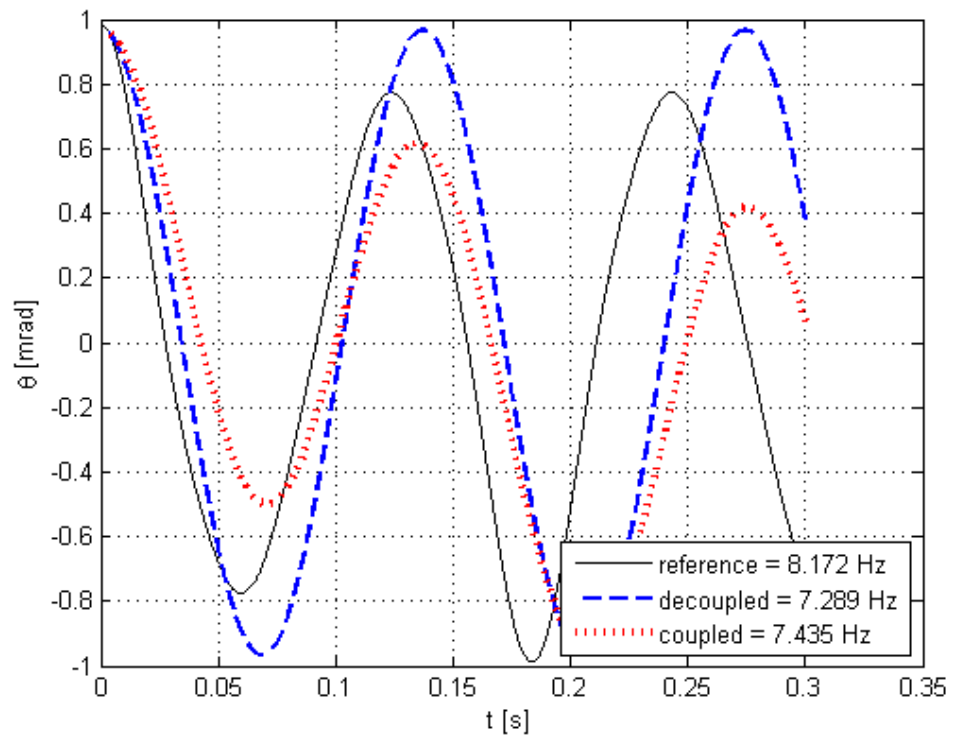


Figure 4.12: Comparison between the twist responses of the reference and discrete cantilever beam models (with and without the presence of cross-coupling terms in the mass matrix) in response to an initial twist deflection

discrete model is approximately 10.8% less than the first mode shape shown in Figure 4.10. This error is relatively large, however, while the decoupled vibration has a fixed amplitude, the reference vibration does not and the amplitude changes over time. This can only be due to the effect of the higher mode shapes on the reference response and means that there are multiple frequencies superimposed on each other. The magnitude of the error and the closeness of the lines in Figure 4.12 clearly shows that the first mode shape is dominant and on this basis the results are considered sufficiently accurate to verify the discrete model.

Although not shown in Figure 4.12, if the length of the simulation is extended the bending mode is observed superimposed on the torsion dynamics of the discrete model. This is primarily due to the relatively large magnitude of the bending response which, when multiplied by the coupling term (Equation (3.18)) becomes significant when compared to the magnitude of the torsion response.

In this chapter the aerodynamic model was validated against the manufacturer's data published by Tuzcu, (2001) for the Cessna Citation V and the structural model was verified against a continuous model of a cantilever beam with stiffness properties representing the wing MAC. The aerodynamic coefficients obtained from the VLM formed the inputs to the aeroelastic model. The results obtained are of sufficient accuracy to use in a qualitative analysis of the overall behaviour of the variable camber wing in the next chapter.

## 5 Application

This chapter describes the application of the variable camber aerodynamics and aeroelastic wing model presented in Chapter 3 and verified and validated in Chapter 4.

Section 5.1 evaluates the discrete structural model parameterized to represent the wing of the Citation V.

Section 5.2 explores the aerodynamics of the variable camber wing including the roll authority.

Section 5.3 explores the dynamics of the aeroelastic wing by looking at the response to changes in aircraft AoA and camber actuation  $\delta_c$ .

The flight state is chosen to be the same as that used for validation: steady, straight and level, high AoA flight corresponding to segment 1 of the RCAM evaluation trajectory (see Appendix F). The flight state is shown in Table 4.1.

### 5.1 Wing Structural Model

This section presents an evaluation of the wing structural model parametrized as the Citation V half wing.

#### 5.1.1 Static Deflections and Initial Conditions

In order to analyse the static deflections of the half wing and compare them to a uniform cantilever beams, point loads of  $F = 1000 \text{ N}$  and  $M = 1000 \text{ Nm}$  are applied at the free ends. The static deflections are then used as initial conditions when evaluating the free responses.

## Bending

The static bending deflection of the half wing is compared to the discrete uniform cantilever beam in Figure 5.1. Figure 5.1 shows the static bending deflection of the

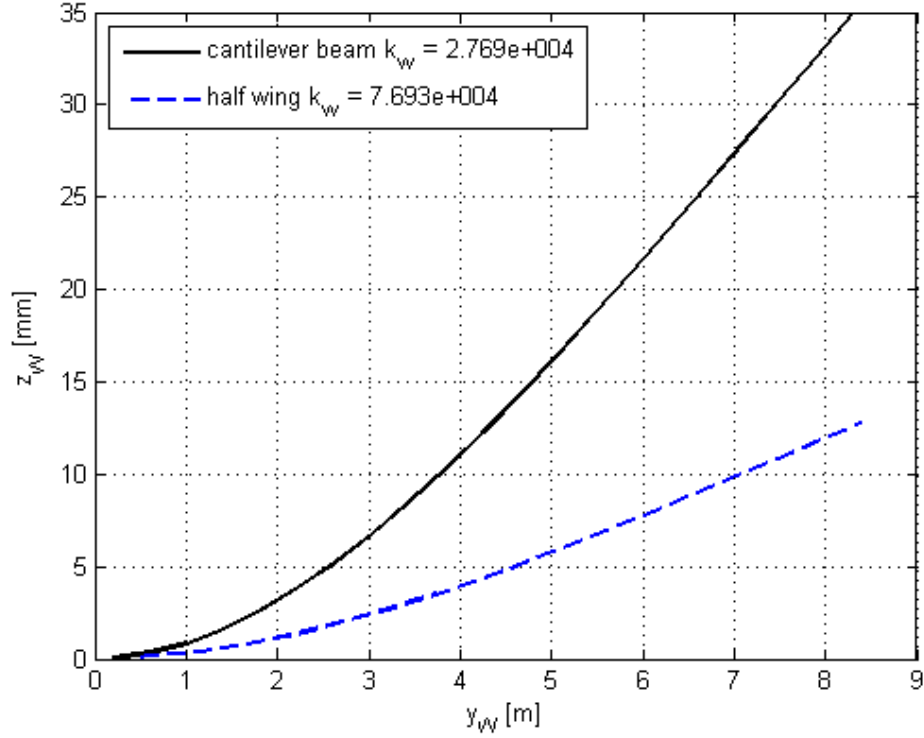


Figure 5.1: Static deflection of the half wing compared to the discrete uniform cantilever beam when a force of 1000  $N$  is applied to the free end

wing for which the greater bending stiffness is evident in the smaller deflection.

## Torsion

The static twist (in  $mrad$ ) of the half wing is compared to the discrete uniform cantilever beam in Figure 5.2. Figure 4.8 also shows the static twist of the half wing for which the smaller torsion stiffness is evident in the greater deflection.

### 5.1.2 Mode Shape and Natural Frequency

When the model is parameterized as a wing the parameters in Equations (3.19) to (3.22b) are correctly integrated along the wing semi-span. However, the assumed mode shapes  $W(y)$  and  $H(y)$  are still those of a uniform cantilever beam due to the

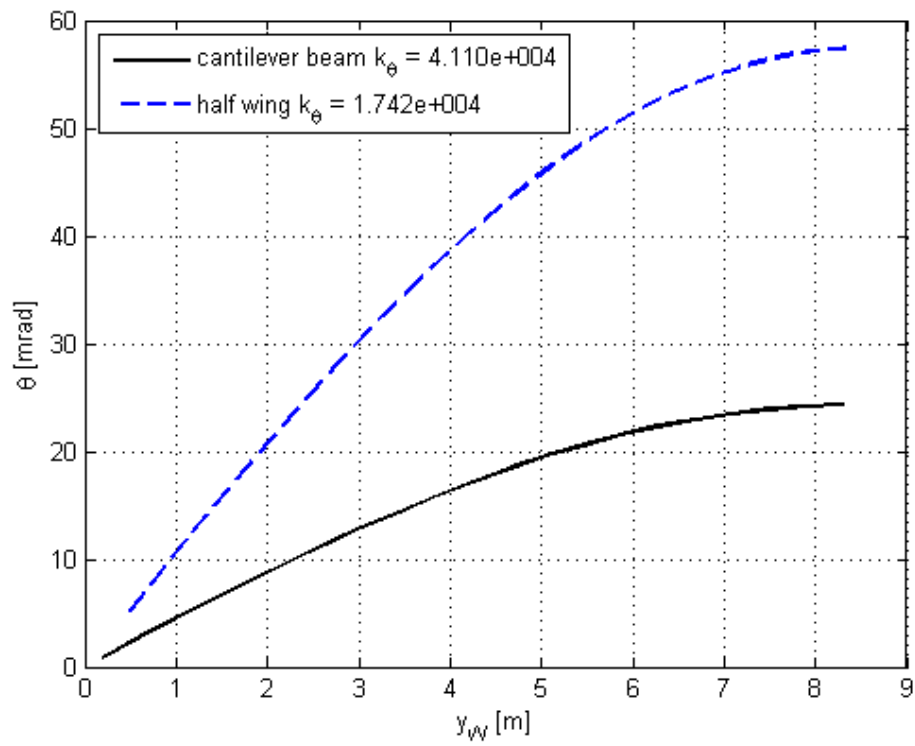


Figure 5.2: Static twist of the half wing compared to the discrete uniform cantilever beam when a moment of 1000  $Nm$  is applied to the free end

availability of analytical expressions for these modes. Therefore, the validity of the model and hinges on how well the first mode of the Citation V wing matches the first mode of the uniform cantilever beam.

### 5.1.3 Free Response

In order to evaluate the free response of the discrete model parametrized as the Citation V wing it is compared to the discrete model parametrized as a uniform cantilever beam. Both the wing and discrete cantilever beam models are initialized at the same initial conditions corresponding to the static deflection of the free end of a continuous uniform beam as given by Equations (4.9) and (4.13). The natural frequencies of the Citation V wing are extracted directly from the eigenvalues of the system matrix  $A$  in Equation (3.26a).

Table 5.1 shows a comparison of the parameters making up the mass and stiffness matrices for the discrete cantilever beam and the Citation V wing. This comparison is used to identify reasons for the differences in the free responses shown in Figures 5.3 and 5.4.

Table 5.1: Comparison of mass and stiffness parameters

Parameter	Discrete cantilever beam	Wing
$M$	160.1	28.58
$I_\theta$	19.59	19.01
$S$	1.880	1.700
$k_w$	$2.769 \times 10^4$	$7.693 \times 10^4$
$k_\theta$	$4.110 \times 10^4$	$1.742 \times 10^4$

The bending vibration of the free end is plotted in Figures 5.3. Figure 5.3 shows that the frequency of the wing bending vibration is approximately 4 times greater than that of the discrete cantilever beam. Based on the fact that the mode shapes are the same, the following observations can be made: the first cause of the larger bending frequency is the decrease in mass which is due to the fact that its distribution along the wing span is not uniform and therefore the mass at the MAC is not the mean of the mass of all panels making up the wing (see Equation (3.19)). The second cause of the larger bending frequency is the larger bending stiffness  $k_w$  which is also due to the fact that its distribution along the wing span is not uniform and therefore the stiffness at the MAC is not the mean of the stiffness of all panels making up the wing (see Equation (3.22a)). The larger stiffness shows that the strips towards the



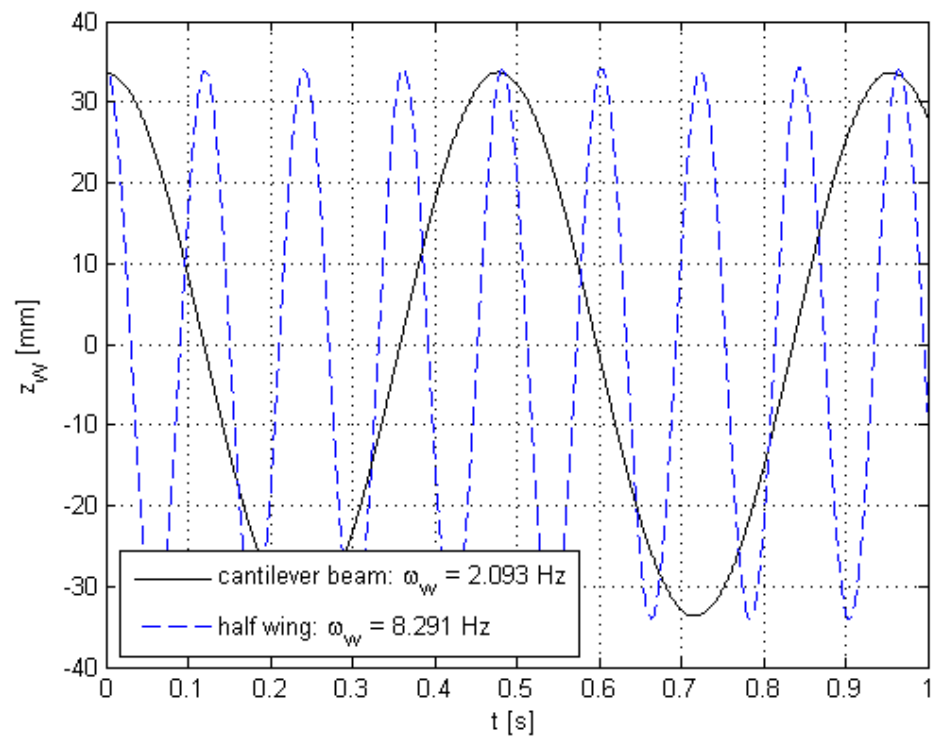


Figure 5.3: Comparison between the bending responses and natural frequencies of the wing and discrete cantilever beam models in response to an initial bending deflection

wing root that have a greater cross-sectional area also have a greater influence on the bending stiffness than the strips at the wing tip. The non-uniformity in cross-section will also affect the assumed mode shape. Therefore, based on the results presented here the discrete model is considered to be a qualitative representation of bending behaviour of the Citation V wing. However, care needs to be taken that the assumed bending mode shape is indeed valid for the application under consideration, especially as the magnitude of deflections increase.

The torsion vibration of the free end is plotted in Figures 5.4. Figure 5.4 shows

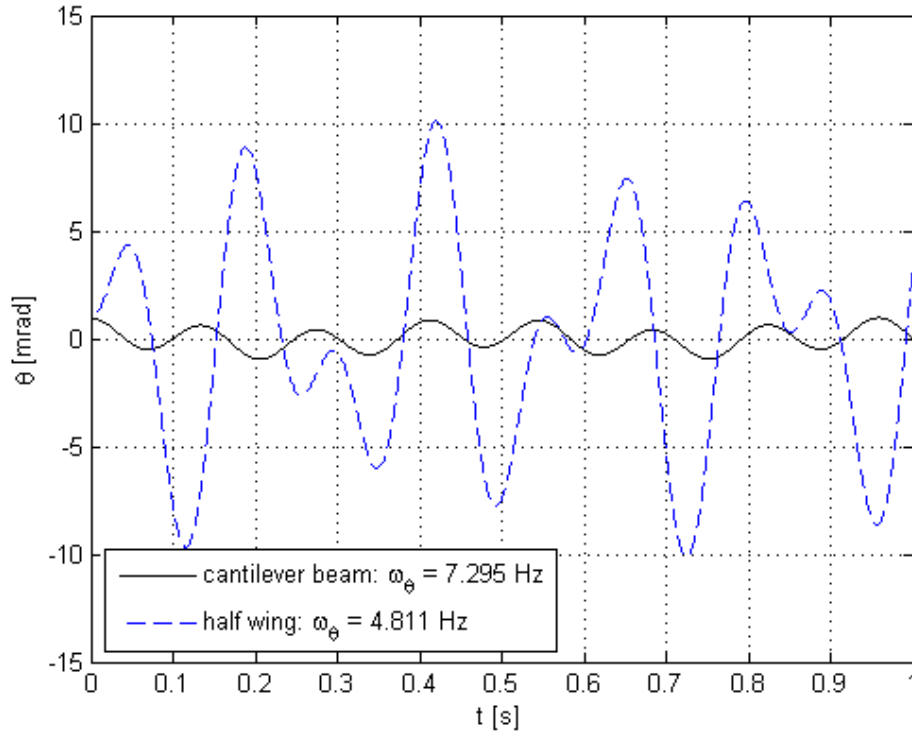


Figure 5.4: Comparison between the twist responses and natural frequencies of the wing and discrete cantilever beam models in response to an initial twist deflection

that the frequency of the wing torsion vibration is approximately 34% less than the torsion frequency of the discrete cantilever beam. Based on the fact that the mode shapes are the same, the following observations can be made: the cause of the decrease in frequency is the decrease in torsion stiffness  $k_\theta$  due to the fact that its distribution along the wing span is not uniform and therefore the stiffness at the MAC is not the mean of the stiffness of all panels making up the wing (see Equation (3.22b)). The decrease shows that the strips towards the wing tip that have a smaller cross-sectional area have a greater influence on the torsional stiffness than the strips at the wing root. Therefore, based on the results presented here the discrete model is

considered to be a qualitative representation of the torsion behaviour of the Citation V wing. However, care needs to be taken that the assumed torsion mode shape is indeed valid for the application under consideration, especially as the magnitude of deflections increase.

## 5.2 Variable Camber Aerodynamics

When comparing the variable camber wing aerodynamics to conventional ailerons, the fact that  $\delta_a$  and  $\delta_c$  do not have the same units means that neither of them can be used as the independent variable. To solve this problem and have a common base for comparison, the maximum camber is selected for this purpose. An analysis of the change in maximum camber caused by an aileron deflection compared to variable camber deflection is shown in Table 5.2. Section 3.2.2 showed that the maximum camber is limited to 6% and Table 5.2 shows that this corresponds to  $\delta_a \approx 11^\circ$  and  $\delta_c = 2.25$ . Therefore, in order to compare the variable camber aerodynamic coefficients to a wing with conventional ailerons, the maximum camber is varied from -6% to 6% by varying  $\delta_a$  from  $-11^\circ$  to  $11^\circ$  and  $\delta_c$  from -2.25 to 2.25.

Table 5.2: Effect of aileron and camber deflection on the airfoil maximum camber

$\delta_a$ [ $^\circ$ ]	Max camber (aileron) [%c]	$\delta_c$	Max camber (variable) [%c]
0	1.855	0	1.855
5	2.800	0.5	2.783
10	5.643	1	3.710
15	8.574	1.5	4.638
20	11.65	2	5.565
25	14.92	2.25	6.029

It is pertinent to the analysis of the aerodynamics in terms of maximum camber to note that the position at which the maximum camber occurs is further back in conventional ailerons than in the case of the variable camber wing. However, Jacobs et al., (1935) show that a rearward movement of the position of maximum camber has very little effect on the lift curve slope ( $C_{L_\alpha}$ ) of the airfoil while causing the zero lift pitching moment ( $C_{m_0}$ ) to become more negative (leading edge down).

### 5.2.1 Lift Distribution with Camber Deflection

As in Section 4.1.1, in order to evaluate the shape and magnitude of the lift distribution along the wing span, the lift coefficient of each wing strip is plotted against its span-wise position (in percentage of semi-span) in Figure 5.5. The ailerons and variable camber were deflected to achieve a maximum camber of 6% and therefore  $\delta_a = 11^\circ$  and  $\delta_c = 2.25$ .

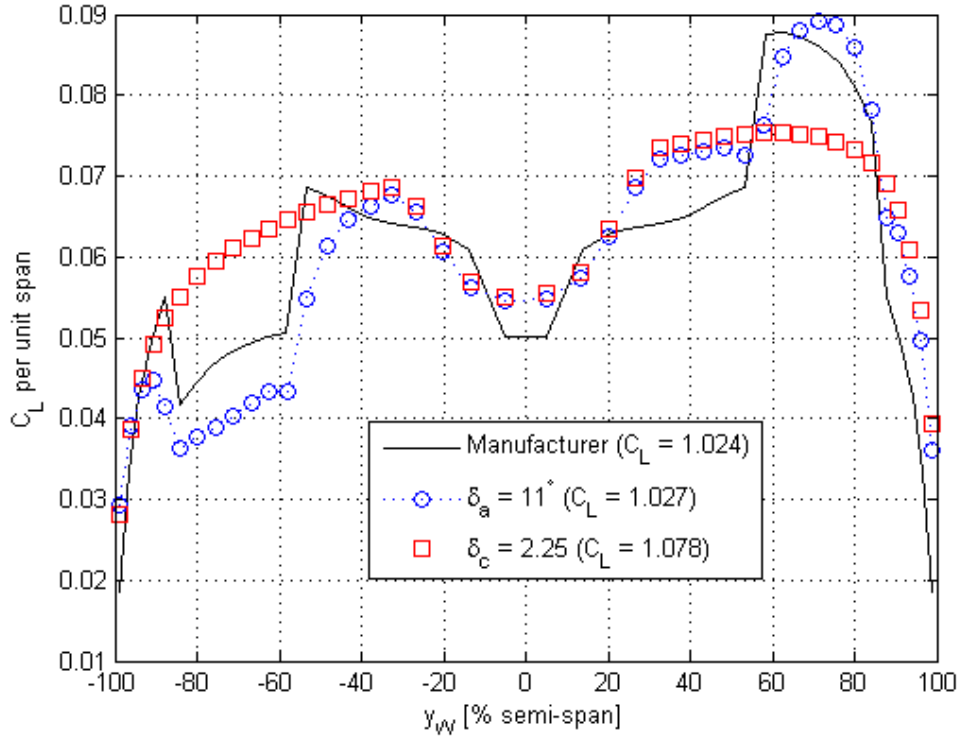


Figure 5.5: Comparison between the effects of aileron deflection and variable camber actuation on the lift distribution along the wing span, calculated at the steady flight state of  $h = 1000 \text{ m}$ ,  $V = 58 \text{ m/s}$ ,  $\alpha = 10.39^\circ$

An evaluation of the quality of the fit is gained by comparing the area under the curves. The area under the aileron curve is only 0.3% greater than under the published (manufacturer's data - Tuzcu, (2001)) curve (as opposed to 5% with undeflected ailerons). Although this appears to be a much better correlation than that obtained with no aileron deflection, it is not possible for the introduction of discontinuities such as ailerons to improve the accuracy of the results. In fact, the opposite is expected and this can be confirmed by noting that the flexible Tornado model overpredicts the changes in lift on both the left and right wings.

The published change in lift is very abrupt at the aileron edges, whereas Tornado

predicts a smoother transition and the aerodynamic effects extend beyond the physical extent of the ailerons themselves. In reality, interference effects between the edges of the ailerons and the cut outs in the wing will cause turbulence and a corresponding loss of lift in these areas. Therefore, the smoother transitions and lower lift predictions by Tornado at the aileron edges are closer to reality than the sharp transitions of the published data. Therefore, considering the unrealistic published data at the aileron edges and the over predictions by Tornado, it can only be concluded that the error in the Tornado lift distribution with deflected ailerons is at least equal to the error without deflected ailerons which is 5%. This is an acceptable result for a first order model.

The area under the variable camber curve is only 5% greater than under the aileron curve. Since the error between the aileron and camber curves and the published data is expected to be the same, the relative error between the aileron and camber curves themselves will be smaller. Therefore the variable camber results are compared to the aileron results in order to compare the aerodynamics of wings with variable camber and conventional ailerons. Figure 5.5 shows that deflection of the flexible wing causes a similar change in the lift distribution to that caused by deflection of the ailerons but that the lift distribution of the deflected flexible wing has no discontinuities. This is a singularly important result because it clearly demonstrates the value of a homogeneous wing as opposed to having articulated control surfaces. As identified by many authors in Chapter 1, this smoothness has the most significant implications for drag reduction because there are no trailing vortices shed from the aileron tips. Note that since the wing tips are the location of maximum camber deflection, the wing tip vortices may actually be larger than on a conventional wing.

An important observation to make is that the lift distribution corresponding to  $\delta_c$  in Figure 5.5 represents a linear increase in the change in camber from wing root to tip. The results presented here demonstrate the feasibility of this variation in camber and its benefits. A potential area of future investigation is the variation and potential optimization of the distribution of change in camber. Both the magnitude and the distribution of the change in camber could be used to change the shape of the wings either to provide roll authority as illustrated here or to optimized the shape for the respective flight phases.

### 5.2.2 Roll Authority

The next step after comparing the lift distribution of the conventional ailerons and the variable camber wing is to identify how much roll authority the latter will provide

as well as the effect of the variable camber on the other aircraft aerodynamics. Figures 5.6 compares the effects of camber and aileron deflections on the rolling moment coefficient  $C_\ell$ .

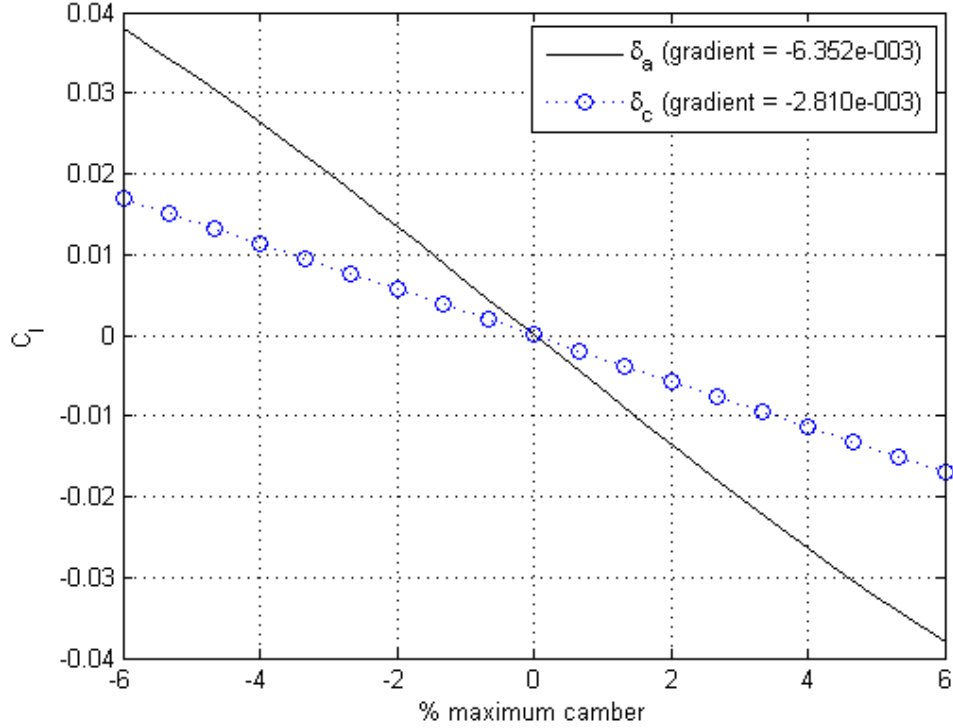


Figure 5.6: Comparison between the effects of aileron deflection and variable camber actuation on the aircraft rolling moment coefficient  $C_\ell$

Table 4.3 shows that the Tornado model over predicts  $C_{\ell_{\delta_a}}$  by 22% compared to the published data and the accuracy of the variable camber actuation will be of the same order of magnitude. Figure 5.6 shows that the variable camber is 44% less effective at generating a rolling moment than conventional ailerons. This is not a good result because it means that a significantly larger change in camber will be required to achieve the same amount of roll authority. However, it is important to keep in mind the linear variation of the camber along the span which means that the position of maximum camber occurs at the wing tip where the amount of lift generated goes to zero (as shown in Figure 5.5). Note also that the span of the aileron is only 30.5% of the wing semi-span and yet it achieves a much higher  $C_{L_{\delta_a}}$  with the same change in max camber.

Therefore, as discussed at the end of Section 5.2.1, it will be possible to change the distribution of the camber actuation along the span in order to achieve higher roll authority. Based simply on the observations recorded above, an alternative camber

variation to explore would provide the same maximum camber as the aileron over the same portion of the span while providing smooth changes on either side so that no discontinuities are introduced into the lift distribution. Another possibility to improve the control authority lies in the fact that the valid range of  $\delta_k$  in Equation (3.8) is quite limited. A full investigation based on a CFD model and/or wind tunnel tests could be conducted in order to expand it. The maximum aileron deflection angle is  $22^\circ$  which corresponds to a maximum camber of 14.9%. This is more than double the current limit of 6% and therefore it is feasible that the maximum allowable camber of the variable camber wing can be extended at least this far.

An effective evaluation of the control effectiveness can be accomplished by comparing the amount of actuation energy required by ailerons to that required by the variable camber (Gern et al., 2002). The required energy is a strong function of dynamic pressure and is made up of both structural and aerodynamic components. Gern et al., (2002) show that for a non-optimum actuation scheme the actuation energy required at the low dynamic pressure at which these results are presented can be orders of magnitude larger than for conventional ailerons due to a lack of ability to extract aerodynamic energy from the air to assist with the structural deformation. This means that the camber actuation may be unachievable at such low speeds making flexible wings for civil transport aircraft impractical. These results, which are generated at a low speed, suggest that it may be possible to achieve practical control because only small deflections are required. The challenge lies in the fact that the whole wing needs to be deformed by a small amount. The key to implementing such an actuation strategy lies in effectively controlling the camber along the whole wing span.

### 5.2.3 Aircraft Aerodynamics

In the introduction to Section 3.2, it was identified that the differential deflection of the variable camber may couple with the longitudinal aerodynamics in unforeseen ways. Therefore the dependency of the longitudinal aerodynamic coefficients on  $\delta_c$  was analysed and it was found that all coupling effects were significantly less than for conventional ailerons. The results are shown in Appendix G. When analysing aircraft dynamics, especially using first order models, it is commonplace to consider the coupling effect of the ailerons on the longitudinal aerodynamics negligible (Etkin and Reid, 1996). Therefore the coupling effect of the variable camber on the longitudinal aerodynamics was also deemed negligible. Similarly, any effects caused by differences in the position of maximum camber between the aileron and the variable camber

are discarded and the analysis is based purely on the lateral aerodynamics.

Figure 5.7 compares the amount of yawing moment ( $C_n$ ) generated by conventional ailerons and the flexible wing. Table 4.3 shows that the Tornado model under

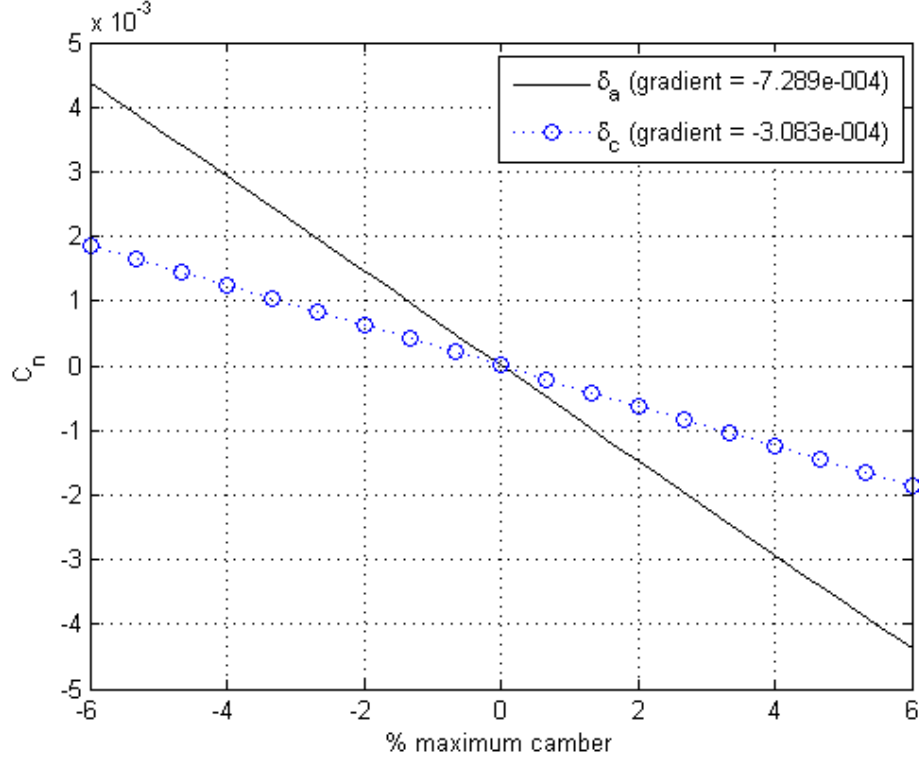


Figure 5.7: Comparison between the effects of aileron deflection and variable camber actuation on the aircraft yawing moment coefficient  $C_n$

predicts  $C_{n\delta_a}$  by 13% compared to the published data and the accuracy of the variable camber actuation will be of the same order of magnitude. Figure 5.7 shows that the variable camber appears to generate less yawing moment than conventional ailerons. However, because  $C_{\ell\delta_c}$  is also smaller than  $C_{\ell\delta_a}$ , the amount of camber deflection required in order to roll the aircraft is larger and therefore Figure 5.7 does not necessarily imply a reduction in roll-yaw coupling.

Figure 5.8 compares the amount of side force ( $C_Y$ ) generated by conventional ailerons and the flexible wing. Figure 5.7 shows that the variable camber appears to generate less side force than conventional ailerons. As with the roll-yaw coupling above, because  $C_{\ell\delta_c}$  is smaller than  $C_{\ell\delta_a}$ , the amount of camber deflection required in order to roll the aircraft is larger and therefore Figure 5.8 does not necessarily imply a reduction in roll-side force coupling.



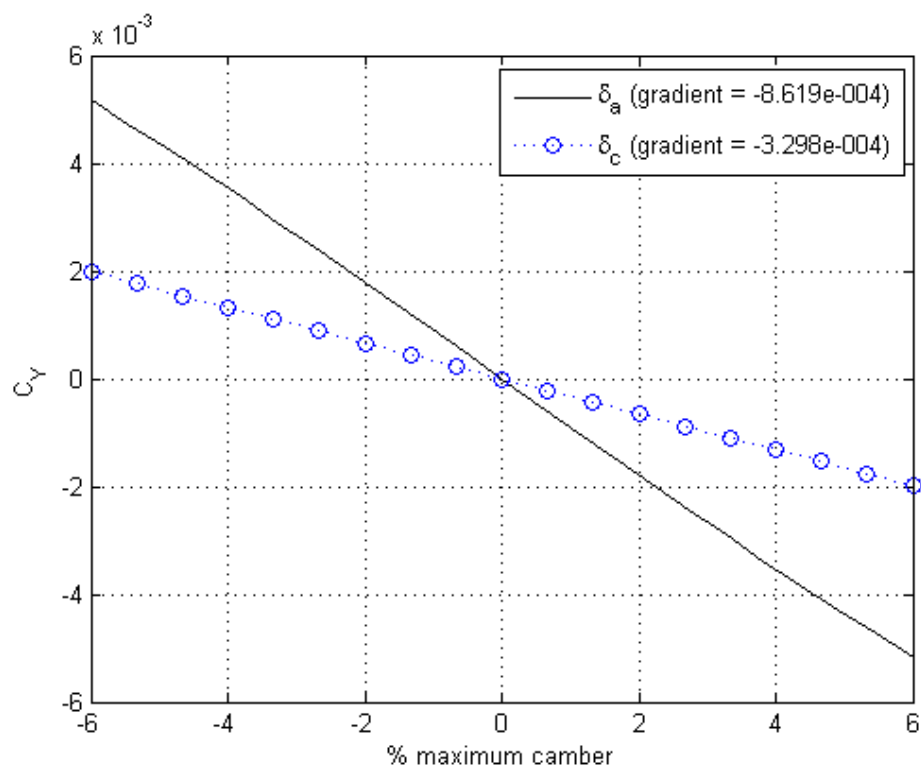


Figure 5.8: Comparison between the effects of aileron deflection and variable camber actuation on the aircraft side force coefficient  $C_Y$

### 5.3 Aeroelastic Wing

In order to investigate the dynamics of the aeroelastic wing, the responses to changes in aircraft AoA and camber actuation  $\delta_c$  are investigated using Bode frequency response plots. The lift curve slope of each strip is needed to calculate the generalized forces in Equation (3.25) and this data is shown in Table 5.3. In addition, the data

Table 5.3: Lift curve slope for each wing strip

Strip	$C_{L_\alpha}$ [/rad]
1	3.921
2	4.115
3	4.538
4	5.023
5	5.315
6	5.363
7	5.409
8	5.451
9	5.489
10	5.514
11	5.524
12	5.526
13	5.517
14	5.488
15	5.430
16	5.327
17	5.159
18	4.912
19	4.558
20	3.988
21	2.941

summarized in Table 5.4 is also required by Equation (3.25). The flight state is chosen to be the same as that used for validation: steady, straight and level, high AoA flight corresponding to segment 1 of the RCAM evaluation trajectory (see Appendix F and Table 4.1).

The undamped responses to external input  $\alpha$  in Figure 5.9 show two distinct unstable resonance peaks at 6 Hz and 31 Hz (note that the y axis of the magnitude plot has units of  $dB$ ). These are frequencies at which the  $w$  and  $\hat{\theta}$  vibrations combine to form

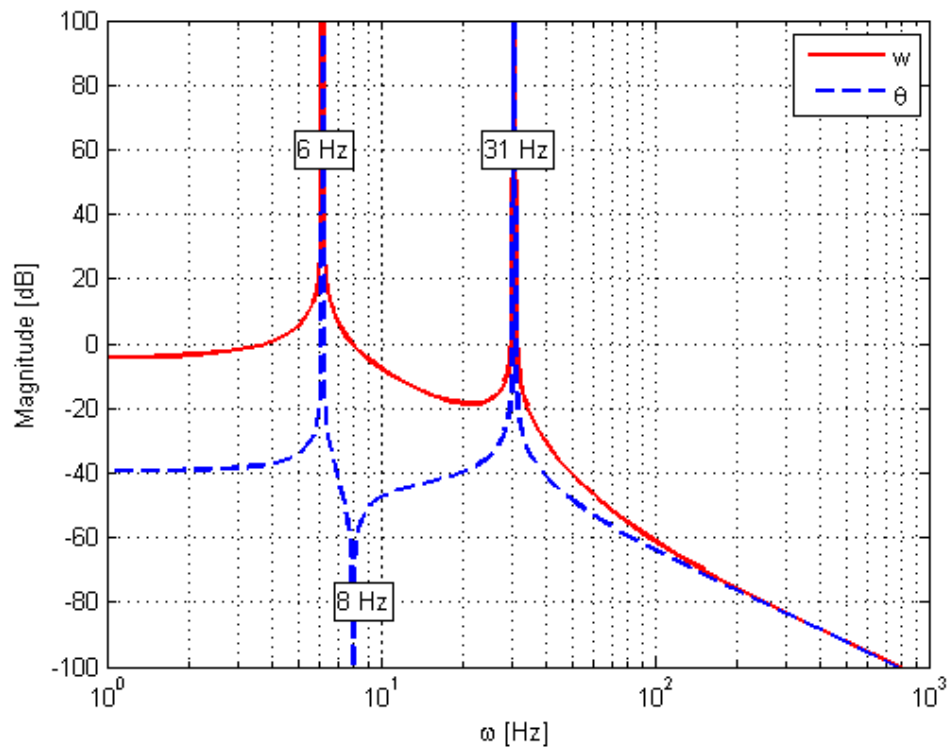


Figure 5.9: Phase space plot of the undamped frequency response of the aeroelastic model to an external stepped pitch input ( $\alpha$ ), clearly showing the unstable pitch and plunge frequency peaks at 6 Hz and 31 Hz

Table 5.4: Parameters calculated using the Citation V wing

Parameter	Value
Distance from quarter chord to elastic axis ( $a$ )	0.2760 $m$
Distance from elastic axis to collocation point ( $r$ )	0.7400 $m$
Lift curve slope ( $C_{L_\alpha}$ )	5.644 [ $/rad$ ]
Pitching moment curve slope ( $C_{m_\alpha}$ )	-2.558 [ $/rad$ ]
Variable camber control effect on lift ( $C_{L_{\delta_c}}$ )	$-7.493 \times 10^{-3}$

an unstable system with an infinite response (ie. the wing will be destroyed). The  $\hat{\theta}$  response also has a stable resonance trough at 8 Hz at which it will go to zero. Away from the resonant frequencies, the magnitude of both responses to input  $\alpha$  is always less than 0  $dB$  indicating that they are smaller than the magnitude of the input. This is a good result because it means that the system is stable in response to AoA inputs at all but the resonant peaks.

The aerodynamically damped responses to external input  $\alpha$  in Figure 5.10 show only one stable resonance peak at 59 Hz. Both  $w$  and  $\hat{\theta}$  responses exhibit the same

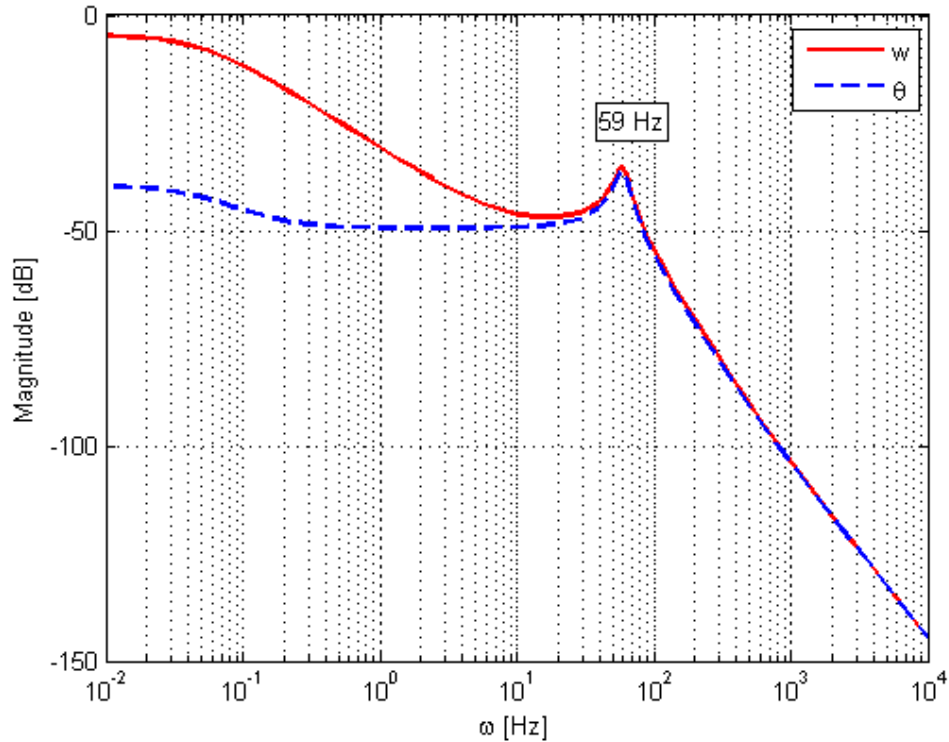


Figure 5.10: Phase space plot of the aerodynamically damped frequency response of the aeroelastic model to an external stepped pitch input ( $\alpha$ ), clearly showing the stable pitch and plunge frequency peak at 59 Hz

resonant peak and behaviour at higher frequencies. However, the resonant peak does not extend to infinity and is therefore stable, unlike in the undamped case. The magnitude of the both responses to input  $\alpha$  is always less than 0 dB indicating that they are always smaller than the magnitude of the input. The Bode plot of the damped system shows a system that always has a stable response to input  $\alpha$ . This is a good result because it means that the system is stable in response to AoA inputs at all frequencies.

The undamped responses to external input  $\delta_c$  in Figure 5.11 show the same two distinct unstable resonance peaks at 6 Hz and 31 Hz as the undamped response to input  $\alpha$ . The  $\alpha$  and  $\delta_c$  responses also have stable resonance troughs at 9 Hz and 48 Hz

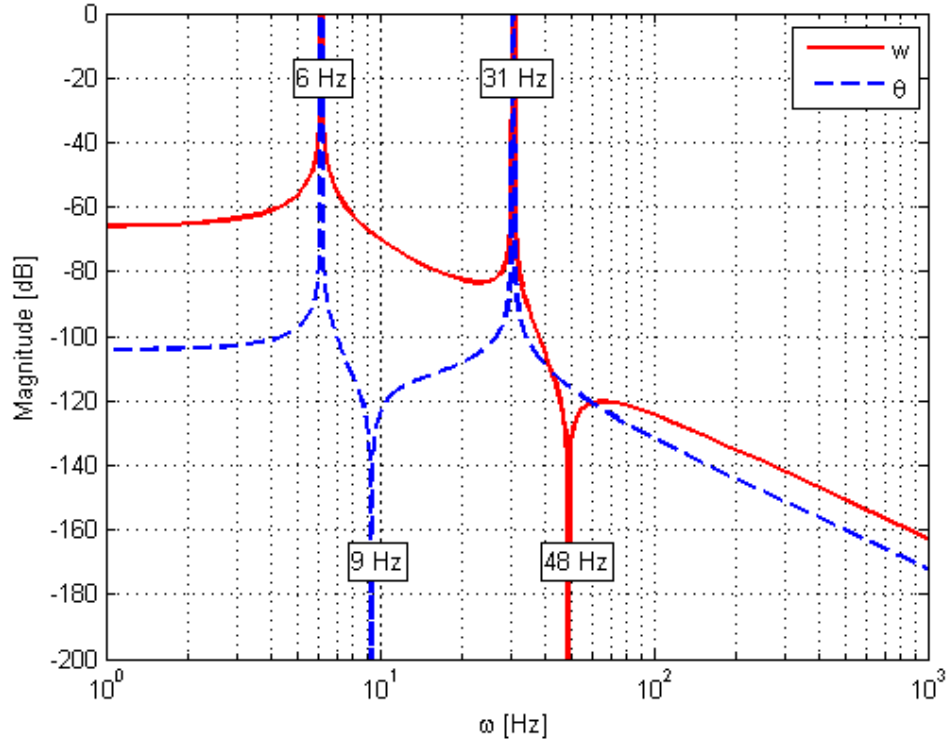


Figure 5.11: Phase space plot of the undamped frequency response of the aeroelastic model to a stepped control input ( $\delta_c$ ), clearly showing the unstable pitch and plunge frequency peaks at 6 Hz and 31 Hz

48 Hz respectively. Away from the resonant frequencies, the magnitude of both responses to input  $\delta_c$  is always less than 0 dB indicating that they are smaller than the magnitude of the input. This is a good result because it means that the system is stable in response to camber actuation inputs at all but the resonant peaks.

The aeroelastically damped responses to external input  $\delta_c$  in Figure 5.12 show a similar resonance peak at 60 Hz to the one in the damped response to input  $\alpha$ .

Both  $w$  and  $\hat{\theta}$  responses exhibit the same peak and similar behaviour, although with

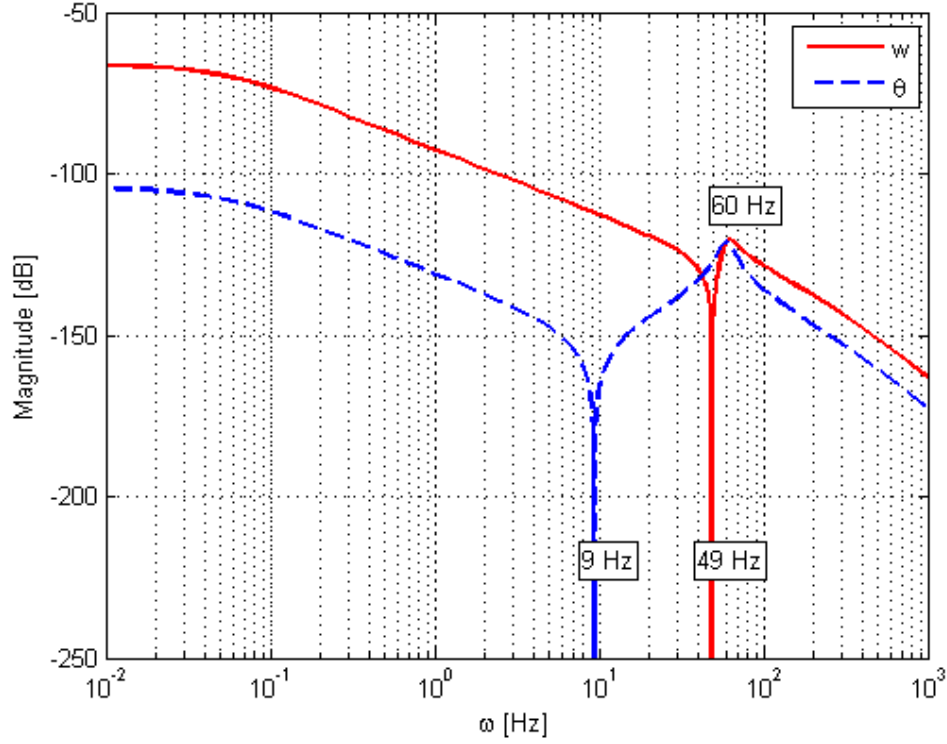


Figure 5.12: Phase space plot of the aerodynamically damped frequency response of the aeroelastic model to a stepped control input ( $\delta_c$ ), clearly showing the stable pitch and plunge frequency peak at 60 Hz

slightly different magnitudes, at higher frequencies. However, as in the case with  $\alpha$ , the resonant peak does not extend to infinity and is therefore stable, unlike in the undamped case. The  $\alpha$  and  $\delta_c$  responses also have resonance troughs similar to the undamped response at 9 Hz and 49 Hz respectively. The magnitude of both responses to  $\delta_c$  is always less than 0 dB indicating that they are always smaller than the magnitude of the input. The Bode plot of the damped system shows a system that always has a stable response to input  $\delta_c$ . This is a good result because it means that the system is stable in response to camber actuation inputs at all frequencies.

Some general observations can be made based on the observation of all four plots:

- The response to a change in AoA is greater than the response to variable camber actuation. This is due to the much larger magnitude of  $C_{L_\alpha}$  as compared to  $C_{L_{\delta_c}}$  in Equation (3.27). This does not affect the stability of the system in response to either input.
- The undamped system shows resonant peaks occurring at the same frequencies

regardless of the types of input. These instability can therefore be said to be a property of the system itself and represent a type of aeroelastic instability (most likely flutter because the results show the heave and twist responses combining in an unstable manner).

- Introduction of aerodynamic damping removes the resonant peaks and the damped system is always stable at the flight state under consideration.

These results show that the stability of the system depends on the amount of aerodynamic damping present. Equation (3.27) shows that the aerodynamic damping is proportional to the aircraft speed  $V$ . However, since the aerodynamic stiffness is proportional to the square of the aircraft speed  $V^2$ , the stiffness will increase faster than the damping as the speed increases. The stiffness determines the frequencies of the resonant peaks and therefore it may happen that a speed will be reached where the aerodynamic damping is no longer strong enough to remove the resonant peaks. The aircraft designer must therefore ensure that the resonant peaks occur at frequencies much higher than the external inputs otherwise flutter will occur. Future investigations should consider the effect of aircraft speed on the response in order to determine at what speed the resonant peaks reappear. The dynamics of the aircraft should then be analysed at this speed to determine whether or not there will be risk of flutter occurring (and whether the Federal Aviation Administration (FAA) requirements are met).

## 6 Conclusions

Several authors and research programs were found where the potential of variable camber to reduce drag was investigated. However, while it was proven that it was possible to achieve significant reductions in drag, no practical applications were found in the public domain. Various programs have investigated the control of a variable camber wing but, except for FlexSys, none attempted to employ a homogeneous wing and to date, flexible wing research has not yet presented a viable solution. The focus has, in general, been limited to the use of flexible leading and trailing edges for drag reduction. This led to the motivation for this work: to develop a model of a homogeneous variable camber wing suitable for later use for control system design and development.

The modelling methodology was based on first order aerodynamic and aeroelastic models with the aim of developing a variable camber actuation scheme and analysing the resulting dynamics. The Cessna Citation V was chosen for use in verification and validation of the model and application of the variable camber technology because the required inertial and aerodynamic data has been published by Tuzcu, (2001). The modelling, verification and validation process was defined and key performance indicators were identified as being the distribution of lift along the wing span, the aircraft and variable camber aerodynamic coefficients and the structural and aeroelastic dynamic responses. The Tornado VLM provided a reliable means of predicting lift when the flow is inviscid and incompressible such as in the approach phase considered here. A suitable approximation for modelling the Citation V airfoil was identified as the NACA23012 airfoil which was kept constant along the whole span. The steady state, low speed, high AoA approach defined in the RCAM problem was chosen as suitable test conditions because they represent the most challenging conditions in terms of required roll authority. The mathematical models were implemented in MATLAB which provided all the required tools for solving the equations and analysing the results.



## 6.1 Mathematical Model

The non-dimensional aerodynamic derivatives were defined for the whole aircraft as functions of the motion and attitude of the aircraft with respect to the air (following standard conventions). The wing was then divided into span-wise strips, each of which has its own geometric, inertial and aerodynamic properties. The VLM implementation in Tornado further divides each strip into a number of sections along the chord.

The homogeneous wing has no external control surfaces and therefore an actuation methodology was defined that takes advantage of the analytical expression for the NACA 5 series camber line (Equations (3.4a) and (3.4b)). An investigation was carried out by manipulating each of the three available parameters. It was found that manipulating parameter  $k$  yielded a smooth change in camber as long as  $p$  and  $m$  were held constant. Therefore the parameter  $\delta_k$  was defined as a modifier to  $k$  such that  $\delta_k = 0$  represents the unmodified airfoil.  $\delta_k$  was shown to vary in the range of  $-4.25 < \delta_k < 2.25$ . In order to achieve roll authority, differential camber control was implemented by linearly varying the change in camber along the wing span. The camber was varied in opposing directions on each wing and a negative camber value implies a mirrored airfoil and not a reflex airfoil.

Strip theory provided a means of modelling the structure of the variable camber wing and combining it with the aerodynamics. The model was based on the typical section in aeroelasticity and has two degrees of freedom: heave and twist. It was assumed that the camber actuation mechanism holds the wing perfectly rigid once the desired camber is reached which simplified the problem by removing any elastic degrees of freedom associated with the variable camber. Structural damping was disregarded for this initial investigation and it was assumed that the bending deflection and angle of twist remain small. The first bending and torsion modes of a cantilever beam were used in the model which was developed using Lagrange's equation. Expressions for the generalised forces were obtained using the work done by the aerodynamic lift and pitching moments. Aerodynamic damping and stiffness matrices were identified as well as control vectors that are functions of the aircraft AoA and variable camber actuation input  $\delta_c$ . This modelling approach means that the applicability is limited to approach and landing phases where aeroelastic instabilities will not be present. A careful investigation will need to be made to extend the model envelope to cover higher speeds. An ideal solution is to design the variable camber wing so that it meets the same aeroelastic performance requirements as the conventional wing. To this end, one of the advantages of the strip theory model is that it can easily

be extended to determine the flutter frequency and the speed at which it occurs (Bismarck-Nasr, 1999). The aeroelastic equations of motion were formulated in state-space form and implemented in MATLAB.

## 6.2 Verification and Validation

The verification and validation process was defined, the first part of which consisted of proving that the aerodynamic coefficients of the discrete aircraft modelled in Tornado match the published data. The trim AoA was found to be  $\alpha = 10.39^\circ$  and the trim  $\delta_e = -10.48^\circ$  which clearly demonstrates the high AoA during the approach phase. The area under the discrete lift distribution curve was found to be only 5% greater than under the published curve. Of this 5%, 4% was attributed to overprediction of the lift in the area of the fuselage which is due to the fuselage being modeled as two perpendicular flat plates as well as the incapability of the VLM to predict interference aerodynamics. The lift distribution along the wing span was shown to be insensitive to the degree of discretization when the number of panels along the chord is greater than 10. It was shown that it would be possible to achieve the greatest accuracy when using 66 or more panels along the span, however limitations in the available computing power meant that a selection of 21 spanwise panels and 10 chordwise panels yielded sufficiently accurate results to validate the discrete aerodynamic model.

The longitudinal aerodynamics were compared to the published data in order to further validate the discrete model. The discrete model was found to lie with 1% of the pulished lift curve ( $C_{L_\alpha}$ ) but only within 39% of the pitching moment curve ( $C_{m_\alpha}$ ). The prediction of the lift curve is excellent, while the error in the pitching moment curve was shown to be a result of a mismatch in the location of the wing AC. It was shown that due to the fact that the wing is not a conventional straight tapered geometry, the AC actually lies behind the 25% MAC position that is used as a reference point in Tornado. The error in elevator effectiveness ( $C_{L_{\delta_e}}$ ) was found to be in the order of 259%. Further analysis was carried out based on the elevator angle required to trim the aircraft using the published data which was calculated to be  $-17.52^\circ$  and is close to the limit of the elevator movement ( $-22^\circ$ ) (as opposed to  $-10.48^\circ$  predicted by Tornado). This showed that there is an error either in the reference data or in its application. However, the source of the error is not pertinent to the results present here and was not explored. The discrete model was shown to be valid up until the stall AoA of  $18^\circ$ .

The lateral aerodynamics were also compared to the published data in order to further validate the discrete model. The lateral dynamics that are not affected by the fuselage were shown to be sufficiently accurate for use in analysis of the variable camber wing lateral dynamics. However, the sideslip angle  $\beta$  must be kept to a minimum because of the large errors in  $C_{Y_\beta}$  and  $C_{\ell_\beta}$ . Therefore the VLM was found to be suitable for steady state analysis of variable camber aerodynamics. Dynamic effects due to rate of change of camber were not modelled and are expected to be significant but are not expected to introduce any additional coupling between the aerodynamic forces that is not already present in the static derivatives.

The second part of the verification process was to show that the static deflections and natural frequencies of the discrete aeroelastic model parametrized as a uniform cantilever beam matched the reference continuous cantilever beam. The free vibration solution of the reference beam was based on Euler-Bernoulli beam theory and was solved using the principle of separation of variables. The deflections were modelled in terms of assumed mode shapes with associated natural frequencies which are multiplied by a harmonic function. The static deflection of the end of the discrete cantilever beam with a point load of 1000  $N$  applied at the end was found to have the same shape as the continuous beam and a tip deflection error of 3.6%. This verified that the implementation of the discrete model was correct.

The static twist of the end of the discrete cantilever beam with a point load of 1000  $N.m$  applied at the end was found to have a completely different shape to the continuous beam and a large tip twist error. This was attributed to the fact that the linear expression used to calculate the static twist (Equation (4.13)) is for a uniform circular shaft and is not applicable to the cantilever beam under consideration. In addition, it was proven that it is not possible for the mode shape to be a straight line in the discrete wing model. Therefore this comparison only partially verified the static twist of the cantilever beam by virtue of the fact that it was both greater than the twist of the circular shaft and not a straight line.

The first four modes were used to model the continuous bending and torsion free responses and it was shown that the first two bending modes and the first three torsion modes lie in the range of 4 - 20 Hz expected for light civil passenger jets (Smith and Shust, 2004). This demonstrated the applicability of the reference model for use in verifying the discrete cantilever beam. The bending free responses of the decoupled and coupled discrete models were shown to equal the response of the reference model when they were initialized with the same conditions. This both verified the discrete implementation in terms of bending and demonstrated that the effect of coupling on the bending mode is negligible. The torsion free responses of the

decoupled and coupled discrete models was shown to lie within approximately 10% of the frequency of the response of the reference model when they were initialized with the same conditions. In addition, the amplitude was observed to vary with time for both the reference and coupled discrete models. This demonstrated the effect of the higher mode shapes in the reference model as well as the coupling in the discrete model which caused the bending mode to be superimposed on the torsion dynamics. On the basis of the dominance of the first mode shape and the relatively small magnitude of the frequency error, the discrete implementation was considered verified in terms of torsion.

### 6.3 Application

The discrete structural model was parameterized to represent the wing of the Citation V and evaluated accordingly. The static deflection of the tip of the Citation V wing with the same load applied was found to be much smaller than the uniform beam due to its much greater stiffness. The static twist of the tip of the Citation V wing with the same load applied was found to be much greater than the uniform beam due to its much smaller stiffness.

The natural frequencies of the discrete aeroelastic model parametrized as the Citation V wing were compared to the uniform cantilever beam. It was shown that while the wing vibrates in bending at a frequency almost 4 times that of the discrete beam (8.291  $Hz$ ) it still lies in the range of 4 - 20  $Hz$  expected for light civil passenger jets (Smith and Shust, 2004). The difference in bending frequencies was shown to be fully explainable by the changes in the model parameters and therefore the discrete wing model is considered to be a qualitative representation of the bending behaviour of the Citation V wing. Similarly, it was shown that the wing vibrates in torsion at a frequency approximately 34% of that of the discrete beam (4.811  $Hz$ ) it also lies in the range of 4 - 20  $Hz$  expected for light civil passenger jets (Smith and Shust, 2004). The difference in torsion frequencies was shown to be fully explainable by the changes in the model parameters and therefore the discrete wing model is considered to be a qualitative representation of the torsion behaviour of the Citation V wing.

The results presented here assume that the first mode of the wing is reasonably well approximated by the first mode shape of a continuous uniform cantilever beam. Since this assumption cannot be validated without the use of finite element methods (FEM) or experimental techniques, care must be taken when applying the model to

problems where the deflections are expected to be large. The larger the deflection, the more an error in the assumed mode shape will have an effect.

The validated aerodynamic model was used to investigate the variable camber aerodynamics and compare them to conventional ailerons. The investigation was carried out at the same low speed approach as the verification and validation. The maximum camber was selected as the independent variable in order to obtain a common baseline for comparison of the variable camber and conventional aileron aerodynamics. The maximum camber was varied from -6% to 6% by varying  $\delta_a$  from  $-11^\circ$  to  $11^\circ$  and  $\delta_c$  from -2.25 to 2.25.

The lift distribution along the wing span was analysed with the ailerons and variable camber deflected to achieve a maximum camber of 6% and therefore  $\delta_a = 11^\circ$  and  $\delta_c = 2.25$ . The area under the aileron lift distribution curve was found to be only 0.3% greater than under the published curve. However, this reduction in error compared to the error with the ailerons undeflected (5%) was not attributed to the accuracy of the solution because the change in lift distribution in the region of the ailerons was observed to be over predicted by Tornado. The error in the variable camber results is expected to be the same or less than the aileron results and therefore comparison between the two was deemed to yield a satisfactory analysis.

The lift distribution of the variable camber wing clearly demonstrated the anticipated smoothness with none of the discontinuities caused by conventional ailerons. This demonstrated the value of a homogeneous wing as opposed to articulated control surfaces. As identified by many authors in Chapter 1, this smoothness has significant implications for drag reduction because there are no trailing vortices shed from the aileron tips.

The camber effectiveness (on rolling moment)  $C_{\ell_{\delta_c}}$  was shown to be 44% less than the aileron effectiveness  $C_{\ell_{\delta_a}}$ . This is not a good result because it means that a significantly larger change in camber will be required to achieve the same amount of roll authority. However, the linear variation of the amount of camber actuation along the span was considered to play an important role here. It was shown that the variable camber has even less coupling with the longitudinal aerodynamics than ailerons and on this basis the longitudinal aerodynamics were not considered in the analysis. The effect of the variable camber deflection on both the yaw  $C_{n_{\delta_a}}$  and side force  $C_{Y_{\delta_a}}$  coefficients was shown to be approximately 40% less than the ailerons. However, because  $C_{\ell_{\delta_c}}$  is also smaller than  $C_{\ell_{\delta_a}}$ , the amount of camber deflection required in order to roll the aircraft is larger and therefore this does not necessarily imply a reduction in roll-yaw or roll-side force coupling.

The interactions between the structure and the aerodynamics of the variable camber wing were investigated at the same flight state as used in all previous analysis. The responses to aircraft AoA and variable camber actuation inputs were evaluated both with and without the presence of aerodynamic damping in the model. The undamped responses to  $\alpha$  and  $\delta_c$  were shown to share common unstable resonance peaks at 6  $Hz$  and 31  $Hz$ . These were identified as points where the natural frequencies of heave and twist combine to form an instability that will destroy the wing. The undamped system was shown to be stable in response to inputs at all other frequencies away from the resonant peaks.

The introduction of aerodynamic damping in the model replaced the unstable resonance peaks with a single stable peak at approximately 60  $Hz$ . The damped responses demonstrated stability at all input frequencies which is a good result. These results also showed that the stability of the system depends on the amount of aerodynamic damping present. It was observed that as the air speed increases, the stiffness will increase faster than the damping and it may happen that a speed will be reached where the aerodynamic damping is no longer strong enough to remove the resonant peaks. The aircraft designer must therefore ensure that the resonant peaks occur at frequencies much higher than any expected external inputs.

## 6.4 Conclusions

This work presents the development, implementation and analysis of a first order model of a variable camber wing. An aerodynamic model of a homogeneous wing employing variable camber actuation was developed based on the VLM and was applied to the approach and landing phases (low speed, steady state, high AoA) of a civil transport aircraft flight profile. The variable camber actuation mechanism works by changing the parameter  $k$  in the analytical equation of the NACA 5 Series airfoil and the amount of change was varied linearly across the wing span. The model was found to over predict the amount of lift generated by 5%, mainly due to inaccuracies in the region of the fuselage. On the other hand, the error in the lift curve was found to be only 1% and the prediction of the pitching moment was shown to have an error related to mismatching reference points. The model was shown to be valid up until the stall AoA of  $18^\circ$ .

Strip theory provided a means of modelling the structure of the variable camber wing and combining it with the aerodynamics. The model was based on the typical section in aeroelasticity and has two degrees of freedom: heave and twist. It was

assumed that the camber actuation mechanism holds the wing perfectly rigid once the desired camber is reached which simplified the problem by removing any elastic degrees of freedom associated with the variable camber. Structural damping was disregarded and it was assumed that the heave and twist remain small. It was shown that the static bending deflection and natural frequency of the discrete model when parametrized as a uniform cantilever beam matched a reference continuous cantilever beam based on Euler-Bernoulli beam theory but that the static twist deflection did not. This was attributed to the fact that the reference beam assumed a circular cross-section and corresponding linear twist along the length and this is not valid for the cantilever beam or the aircraft wing. The free bending response of the discrete model was found to match the continuous model exactly and show no coupling effects. The free torsion response of the discrete model was found to lie within 10% of the continuous model and clearly show the bending frequency superimposed on the torsion dynamics. The first modes of the Citation V wing in both bending and torsion were shown to lie in the expected range for light civil passenger jets (4 - 20  $Hz$ ).

The variable camber aerodynamics were compared to conventional ailerons at the same low speed approach as before. The lift distribution of the variable camber wing clearly demonstrated smoothness with none of the discontinuities caused by conventional ailerons. This confirmed the value of a homogeneous wing as opposed to articulated control surfaces due to the potential for drag reduction because there are no trailing vortices shed from aileron tips. The camber effectiveness was shown to be 44% less than the aileron which means that a significantly larger change in camber will be required to achieve the same amount of roll authority. However, the linear variation of the amount of camber actuation along the span was considered to play an important role here and is an area for future investigation. It was shown that the variable camber has even less coupling with the longitudinal aerodynamics than conventional ailerons and that the coupling with both yaw and side force appears smaller. However, since more variable camber input is required in order to achieve the same roll authority as conventional ailerons, this does not necessarily mean that the pilot will not have to apply as much rudder correction in order to execute a coordinated turn.

The stability of the system in response to aircraft AoA and variable camber inputs was evaluated both with and without the presence of aerodynamic damping in the model. The undamped system was shown to be stable in response to inputs at all frequencies away from the resonant peaks at 6  $Hz$  and 31  $Hz$ . The introduction of aerodynamic damping in the model replaced the unstable resonance peaks with a

single stable peak at approximately 60  $Hz$  and demonstrated stability at all input frequencies. The stability of the system was therefore found to depend on the amount of aerodynamic damping present and the aircraft designer must ensure that the resonant peaks occur at frequencies much higher than any expected external inputs.

## 6.5 Recommendations for Future Work

Throughout this work, areas were identified and discussed as potential for future investigations. These discussions are presented and expanded below.

The biggest area of concern in the implementation described in this work was the assumption that the wing can be approximated by a uniform cantilever beam. This assumption was further brought into question by the fact that the wing is not straight but has a discontinuity in the first third of the span. Further work should be conducted in order to confirm or disprove this assumption. This could be done using FEM tools or actual experimentation with a scale model of both beam and wing and is expected to result in modifications to the discrete model and a corresponding extension to the envelope of validity of the model.

The next area of investigation should concern expansion of the usable range of  $\delta_k$ . CFD and/or wind tunnel testing can provide not only this but also an identification and quantification of dynamic aerodynamic effects.

As part of efforts to expand the range of applicability of the model, an investigation needs to be carried out to determine the effect of aircraft speed on the dynamic response in order to determine at what speed the resonant peaks reappear. The dynamics of the aircraft should then be analysed at this speed to determine whether or not there will be risk of flutter occurring (and therefore whether the FAA requirements are met).

After expanding the region of validity of the model, the next logical step is to expand the contents of model into a complete aircraft, possibly by assuming initially that the rest of the aircraft is rigid. It will then be possible to carry out control system design affecting both the amount of force generated by the flexible wing (an inner loop) and the roll control of the aircraft (an outer loop).

It was noted that the lift distribution considered in this work represents a linear increase in the change in camber from wing root to tip. As part of a control system



design, the variation and potential optimization of the distribution of variable camber should be investigated. Both the magnitude and the distribution of the variable camber can be used as inputs to a control system aimed at optimizing the wing shape for a specific phase of flight.

Together with any control system design, an investigation should be carried out into the amount of actuation energy required by ailerons as compared to that required by the variable camber. The required energy was noted to be a strong function of dynamic pressure and made up of both structural and aerodynamic components. The key to implementing an effective control system lies in controlling the camber along the whole span.

Finally, and in parallel with the above developments, a practical method of implementing a morphing wing needs to be investigated. This could consist of a wing constructed of smart material skins with a deformable core that can change its shape when the skins deflect. Another alternative is to implement an internal mechanical actuator such that the wing skin is homogeneous and deforms according to changes in shape in the internal structure. The most important factor to any practical implementation is that it be light enough that the aircraft does not lose in weight gain what it gains in wing efficiency.

## REFERENCES

- Abbott, I. and von Doenhoff, A. (1959). *Theory of Wing Sections: Including a Summary of Airfoil Data*, Dover Publications Inc.
- Anderson, J. (2001). *Fundamentals of Aerodynamics*, third edn, McGraw-Hill.
- Bismarck-Nasr, M. N. (1999). *Structural Dynamics in Aeronautical Engineering*, AIAA.
- Cessna Aircraft Company (1988). *Airplane Flight Manual Citation V*.
- Cessna Aircraft Company (1989). *Operating Manual Model 560 Citation V*.
- Culick, F. (2001). What the wright brothers did and did not understand about flight mechanics in modern terms, *Proceedings of the 37th AIAA/ASME/SAE/ASEE Joint Propulsion Conference and Exhibit*, Salt Lake City, Utah.
- Etkin, B. and Reid, L. D. (1996). *Dynamics of Flight: Stability and Control*, third edn, John Wiley and Sons Inc.
- FM(AG08) (1997a). Robust control techniques tutorial document.
- FM(AG08) (1997b). Robust flight control design challenge problem formulation and manual: the research civil aircraft model (rcam).
- Gern, H., Inman, D. and Kapania, R. (2002). Computation of actuation power requirements for smart wings with morphing airfoils, *Proceedings of the 43rd AIAA/ASME/ASCE/AHS/ASC Structures, Structural Dynamics, and Materials Conference*, Denver, Colorado.
- Gilbert, W. (1981). Mission adaptive wing system for tactical aircraft, *Journal of Aircraft* **18**(7): 597–602.
- Gilyard, G. B., Georgie, J. and Barnicki, J. S. (1999). Flight test of an adaptive configuration optimization system for transport aircraft, *Technical Report NASA/TM-1999-206569*, NASA.

- Hetrick, J., Osborn, R., Kota, S., Flick, P. and Paul, D. (2007). Flight testing of mission adaptive compliant wing, *Proceedings of the 48th AIAA/ASME/ASCE/AHS/ASC Structures, Structural Dynamics, and Materials Conference*, Honolulu, Hawaii.
- Hibbeler, R. (2000). *Mechanics of Materials*, fourth edn, Prentice Hall.
- Jacobs, E. N. and Pinkerton, R. M. (1935). Tests in the variable-density wind tunnel of related airfoils having the maximum camber unusually far forward, *Technical Report 537*, National Advisory Committee for Aeronautics.
- Jacobs, E. N., Ward, K. E. and Pinkerton, R. M. (1935). The characteristics of 78 related airfoil sections from tests in the variable-density wind tunnel, *Technical Report 460*, National Advisory Committee for Aeronautics.
- Johnston, C., Neal, D., Wiggins, L., Robertshaw, H., Mason, W. and Inman, D. (2003). A model to compare the flight control energy requirements of morphing and conventionally actuated wings, *Proceedings of the 44th AIAA/ASME/ASCE/AHS Structures, Structural Dynamics, and Materials Conference*, Norfolk, Virginia.
- Kota, S., Hetrick, J. and Osborn, R. (2006). Adaptive structures: Moving into the mainstream, *Aerospace America* pp. 16–18.
- Lednicer, D. *The incomplete guide to airfoil usage*, [www.ae.uiuc.edu/m-selig/ads/aircraft.html](http://www.ae.uiuc.edu/m-selig/ads/aircraft.html). Last accessed: 30 November 2011.
- Martins, A. and Catalano, F. (2003). Drag optimization for transport aircraft mission adaptive wing, *Journal of the Brazilian Society of Mechanical Sciences and Engineering* **25**(1): 1–8.
- Melin, T. (2000). *A vortex lattice matlab implementation for linear aerodynamic wing applications*, Master’s thesis, Royal Institute of Technology (KTH), Department of Aeronautics.
- Mukhopadhyay, V. (2003). Historical perspective on analysis and control of aeroelastic responses, *Journal of Guidance, Control and Dynamics* **26**(5): 673–684.
- NAFEMS and ASME (2006). What is verification and validation?
- NASA-DFRC, M Curry (ed.). *Back to the future: Active aeroelastic wing flight research*, [www.nasa.gov/centers/dryden/news/FactSheets/FS-061-DFRC.html](http://www.nasa.gov/centers/dryden/news/FactSheets/FS-061-DFRC.html). Last accessed: 30 November 2011.

- Patel, S., Majji, M., Koh, B., Junkins, J. and Rediniotis, O. (2005). Morphing wing: A demonstration of aero servo elastic distributed sensing and control, *Technical report*, Texas Institute for Intelligent Bio-nano Materials and Structures for Aerospace Vehicles.
- Pendleton, E. W., Bessette, D., Field, P. B., Miller, G. D. and Griffin, K. E. (2000). Active aeroelastic wing flight research program: Technical program and model analytical development, *Journal of Aircraft* **37**(4): 554–561.
- Powers, S. G., Webb, L. D., Friend, E. L. and Lokos, W. A. (1992). Flight test results from a supercritical mission adaptive wing with smooth variable camber, *Technical Report NASA-TM-4415*, NASA.
- Rao, S. (1995). *Mechanical Vibrations*, third edn, Addison-Wesley.
- Smith, K. B. and Shust, W. C. (2004). Bounding natural frequencies in structures 1: Gross geometry, material and boundary conditions, *Proceedings of the XXII International Modal Analysis Conference*, Society of Experimental Mechanics.
- Tuzcu, I. (2001). *Dynamics and Control of Flexible Aircraft*, PhD thesis, Virginia Polytechnic Institute and State University.
- Wilson, J. (2002). Active aeroelastic wing: A new/old twist on flight, *Aerospace America* pp. 34–37.
- Zipfel, P. (2000). *Modeling and Simulation of Aerospace Vehicle Dynamics*, AIAA.

## APPENDIX A Three View

Tuzcu, (2001) presents an investigation into a dynamic formulation capable of simulating the flight of flexible aircraft in which he chooses to use the reference frame ( $W$ ) presented in Section 3.1 and fixed in the undeformed body instead of using mean axes. Tuzcu, (2001) also provides a numerical example based on the data for the Cessna Citation V presented here. Additional information about the Citation V was obtained directly from Cessna in the form of the Flight Manual (Cessna Aircraft Company, 1988) and Operating Manual (Cessna Aircraft Company, 1989).

Figures A.1 and A.2 show two views of the aircraft as it is parametrized for use in Tornado. Note that the reference point in the figures is the origin of the wing coordinate system, however, because Tornado calculates all moments about its own reference point, the actual positions of the apexes are adjusted so that the Tornado reference point lies at the centre of gravity.

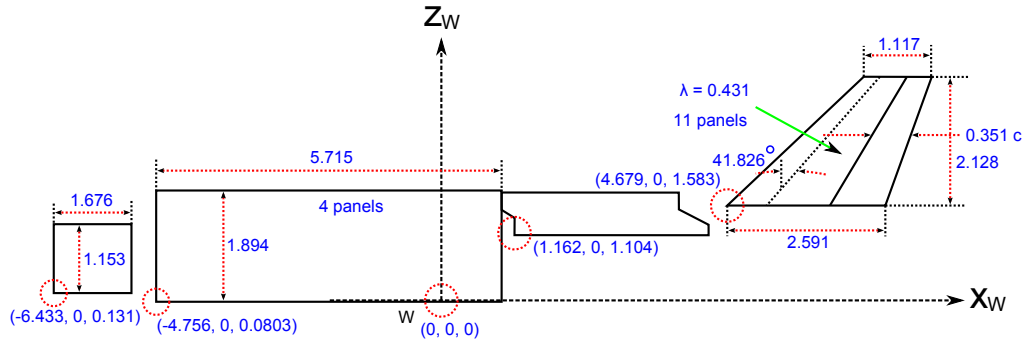


Figure A.1: Side view of the Cessna Citation V geometry showing important dimensions and reference points (indicated by dotted circles)

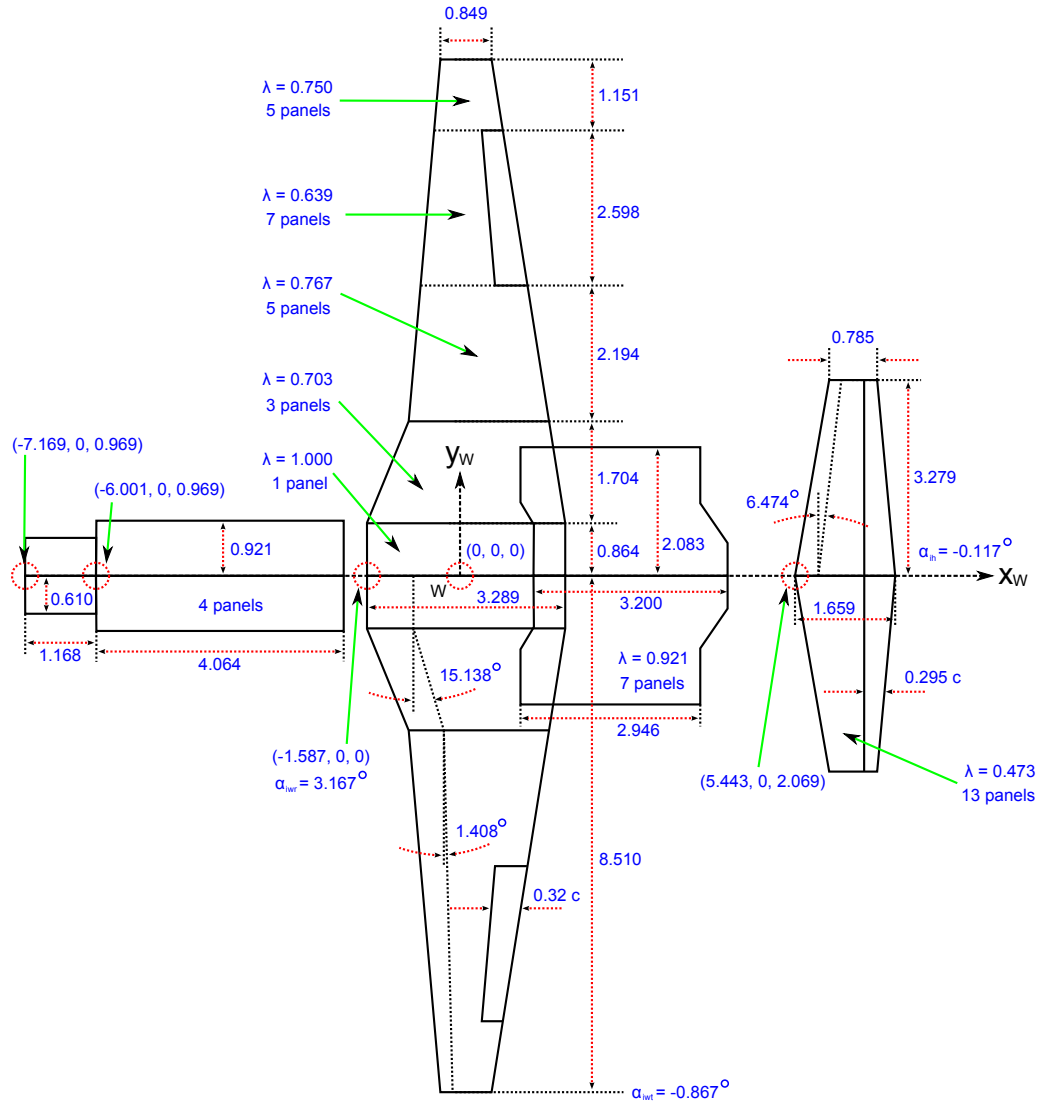


Figure A.2: Top view of Cessna Citation V geometry showing important dimensions and reference points (indicated by dotted circles)

## APPENDIX B Strip Properties

The calculations used to determine the structural properties of each wing strip are based on the geometry of the airfoil and the chord length at the midpoint of the strip width. The strip cross-sections were represented using the NACA23012 airfoil discretized into  $m$  trapezoids as shown in Figure B.1.

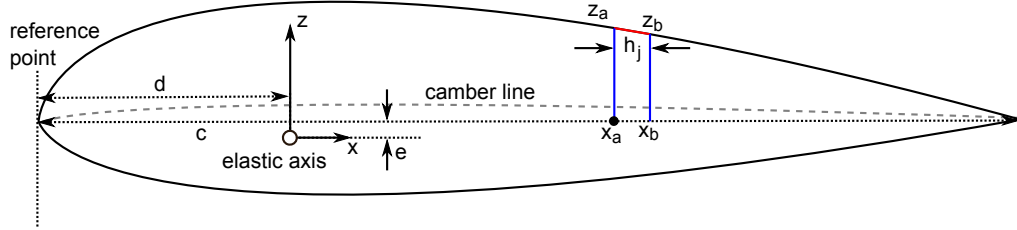


Figure B.1: Geometry of an airfoil cross section showing the elastic axis and relevant dimensions

The significant dimensions of trapezoid  $j$  were calculated as follows:

$$x_a = \begin{cases} |x_j - d| & \text{iff } |x_j - d| < |x_{j+1} - d| \\ |x_{j+1} - d| & \text{iff } |x_j - d| > |x_{j+1} - d| \end{cases} \quad (\text{B.1a})$$

$$x_b = \begin{cases} |x_{j+1} - d| & \text{iff } |x_j - d| < |x_{j+1} - d| \\ |x_j - d| & \text{iff } |x_j - d| > |x_{j+1} - d| \end{cases} \quad (\text{B.1b})$$

$$z_a = \begin{cases} |z(x_j) - e| & \text{iff } |x_j - d| < |x_{j+1} - d| \\ |z(x_{j+1}) - e| & \text{iff } |x_j - d| > |x_{j+1} - d| \end{cases} \quad (\text{B.1c})$$

$$z_b = \begin{cases} |z(x_{j+1}) - e| & \text{iff } |x_j - d| < |x_{j+1} - d| \\ |z(x_j) - e| & \text{iff } |x_j - d| > |x_{j+1} - d| \end{cases} \quad (\text{B.1d})$$

$$h = x_b - x_a \quad (\text{B.1e})$$

$d$  and  $e$  are the horizontal and vertical distances from the reference point to the elastic axis respectively.

The cross-sectional area of trapezoid  $j$  was calculated as follows:

$$A_j = \frac{h}{2}(z_a + z_b) \quad (\text{B.2})$$

The gradient of the non-parallel side was calculated as follows:

$$g = \frac{zb - za}{h} \quad (\text{B.3})$$

The moments of inertia of trapezoid  $j$  about the elastic axis were calculate as follows:

$$I_{x_j} = \frac{h}{12} (z_a^3 + z_a^2 z_b + z_a z_b^2 + z_b^3) \quad (\text{B.4a})$$

$$I_{z_j} = \frac{g}{4} (x_b^4 - x_a^4) + \frac{1}{3} (z_a - g x_a) (x_b^3 - x_a^3) \quad (\text{B.4b})$$

The area and moments of inertia of the whole strip were calculated by summing over all  $m$  trapezoids making up the airfoil. The polar moment of inertia of the strip about the elastic axis was calculated as follows:

$$J = I_x + I_z \quad (\text{B.5})$$

The static mass moment of inertia of trapezoid  $j$  about the elastic axis per unit mass and per unit span was calculated assuming constant density across the span as follows ( $\int r dm = \rho b \int r dA$ ):

$$\bar{S}_{ea_j} = \int r dA = \sum_{j=1}^m \left[ \frac{g}{3} (x_b^3 - x_a^3) + \frac{1}{2} (z_a - g x_a) (x_b^2 - x_a^2) \right] \quad (\text{B.6})$$

The static mass moment about the elastic axis of strip  $i$  was calculated as follows:

$$S_{ea_i} = m_i b_i \sum_{j=1}^m \bar{S}_{w_j} \quad (\text{B.7})$$

Tables B.1 and B.2 lists the properties of the strips making up the discretized wing. The column  $y$  contains the position of the strip centroid in the  $y_W$  coordinate system.



Table B.1: Geometric properties for each wing strip

<b>Strip</b>	$y$ [m]	$A$ [m <sup>2</sup> ]	$J$ [m <sup>4</sup> ]	$S_{ea}$ [m <sup>3</sup> ]
1	0.4307	0.840	0.5544	81.59
2	1.1701	0.752	0.4440	25.08
3	1.7619	0.596	0.2793	11.80
4	2.3030	0.470	0.1734	6.232
5	2.8052	0.393	0.1216	2.700
6	3.2809	0.354	0.09817	2.745
7	3.7313	0.318	0.07926	1.774
8	4.1563	0.286	0.06407	1.486
9	4.5558	0.257	0.05190	1.150
10	4.9539	0.230	0.04157	1.040
11	5.3564	0.204	0.03277	0.7492
12	5.7454	0.181	0.02568	0.4953
13	6.1218	0.159	0.01997	0.3098
14	6.4855	0.140	0.01542	0.2122
15	6.8366	0.123	0.01181	0.1512
16	7.1750	0.107	0.008976	0.1047
17	7.4870	0.0933	0.006842	0.06081
18	7.7601	0.0822	0.005310	0.03557
19	8.0013	0.0730	0.004186	0.02255
20	8.2089	0.0655	0.003370	0.01456
21	8.3955	0.0591	0.002742	0.01162

Table B.2: Inertial properties for each wing strip

<b>Panel</b>	$m[kg]$	$I_{yy} [kg.m^2]$	$EI [N.m^2]$	$GJ [N.m^2]$
1	161.7	83.05	$2.787 \times 10^7$	$3.071 \times 10^7$
2	81.96	33.33	$2.199 \times 10^7$	$2.730 \times 10^7$
3	59.51	19.16	$1.608 \times 10^7$	$2.142 \times 10^7$
4	49.32	12.93	$1.274 \times 10^7$	$1.610 \times 10^7$
5	29.44	10.26	$9.692 \times 10^6$	$1.264 \times 10^7$
6	37.10	14.03	$7.422 \times 10^6$	$1.051 \times 10^7$
7	29.76	8.913	$5.769 \times 10^6$	$8.414 \times 10^6$
8	31.05	8.369	$4.623 \times 10^6$	$6.631 \times 10^6$
9	32.00	7.856	$3.878 \times 10^6$	$5.345 \times 10^6$
10	30.26	6.908	$3.180 \times 10^6$	$4.307 \times 10^6$
11	26.98	5.212	$2.535 \times 10^6$	$3.258 \times 10^6$
12	22.14	3.444	$2.004 \times 10^6$	$2.325 \times 10^6$
13	17.28	2.417	$1.638 \times 10^6$	$1.625 \times 10^6$
14	14.88	1.800	$1.328 \times 10^6$	$1.166 \times 10^6$
15	13.42	1.418	$1.112 \times 10^6$	$8.592 \times 10^5$
16	11.87	1.155	$9.467 \times 10^5$	$6.472 \times 10^5$
17	9.597	0.9336	$7.983 \times 10^5$	$4.791 \times 10^5$
18	7.813	0.7825	$6.545 \times 10^5$	$3.253 \times 10^5$
19	6.576	0.6254	$5.268 \times 10^5$	$1.896 \times 10^5$
20	6.117	0.4438	$4.162 \times 10^5$	$7.315 \times 10^4$
21	5.704	0.2806	$4.162 \times 10^5$	$7.315 \times 10^4$

## APPENDIX C Aircraft Geometry

Tables C.1, C.2 and C.3 list relevant geometrical data together with the reference or calculation from which it was obtained. The positions of the wing MAC and all aerodynamic centres are in the wing coordinate system.

Table C.1: Parameters defining the wing geometry

Symbol	Name	Value	Reference
$b_w$	reference span	17.02 <i>m</i>	(Tuzcu, 2001)
$\bar{c}_w$	MAC	2.032 <i>m</i>	(Cessna Aircraft Company, 1989)
$x_{mac_w}$	MAC x position	−0.784 <i>m</i>	(Cessna Aircraft Company, 1989)
$y_{mac_w}$	MAC y position	3.693 <i>m</i>	(Tuzcu, 2001)
$z_{mac_w}$	MAC z position	0.258 <i>m</i>	$y_{mac_w} \tan(\theta_{di_w})$
$\theta_{di_w}$	dihedral angle	4°	(Cessna Aircraft Company, 1989)
$S_w$	reference area	34.002 <i>m</i> <sup>2</sup>	(Tuzcu, 2001)
$\alpha_{i_{wr}}$	root incidence angle	3.167°	(Cessna Aircraft Company, 1989)
$\alpha_{i_{wt}}$	tip incidence angle	−0.867°	(Cessna Aircraft Company, 1989)

Table C.2: Parameters defining the horizontal tail geometry

Symbol	Name	Value	Reference
$b_h$	reference span	6.450 <i>m</i>	(Tuzcu, 2001)
$\bar{c}_h$	MAC	1.274 <i>m</i>	$\frac{2}{3} \left[ \lambda + \frac{1}{\lambda+1} \right] c_{rh}$
$x_{mac_h}$	MAC x position	5.703 <i>m</i>	(Tuzcu, 2001)
$y_{mac_h}$	MAC y position	1.400 <i>m</i>	(Tuzcu, 2001)
$z_{mac_h}$	MAC z position	2.291 <i>m</i>	$y_{mac_h} \tan(\theta_{di_h})$
$\theta_{di_h}$	dihedral angle	9°	(Cessna Aircraft Company, 1989)
$S_h$	reference area	7.844 <i>m</i> <sup>2</sup>	(Tuzcu, 2001)
$\alpha_{i_h}$	incidence angle	−0.117°	(Cessna Aircraft Company, 1989)

Table C.3: Parameters defining the vertical tail geometry

<b>Symbol</b>	<b>Name</b>	<b>Value</b>	<b>Reference</b>
$b_v$	reference span	2.128 <i>m</i>	(Tuzcu, 2001)
$\bar{c}_v$	MAC	1.952 <i>m</i>	$\frac{2}{3} \left[ \lambda + \frac{1}{\lambda+1} \right] c_{rv}$
$x_{mac_v}$	MAC x position	5.666 <i>m</i>	(Tuzcu, 2001)
$y_{mac_v}$	MAC y position	0.0 <i>m</i>	(Tuzcu, 2001)
$z_{mac_v}$	MAC z position	2.507 <i>m</i>	(Tuzcu, 2001)
$S_v$	reference area	3.945 <i>m</i> <sup>2</sup>	(Tuzcu, 2001)

## APPENDIX D Weight and Balance

Figure D.1 shows the relevant aircraft weight and balance information with respect to the manufacturer's datum and relative to the wing coordinate system. The data was obtained from references (Cessna Aircraft Company, 1989) and (Cessna Aircraft Company, 1988).

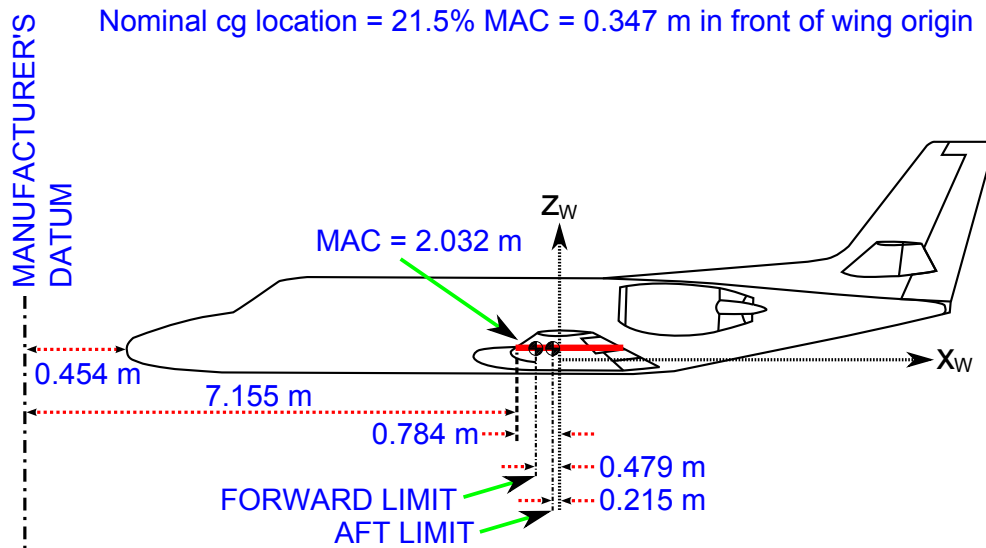


Figure D.1: Side view of the Cessna Citation V showing dimensions used for weight and balance calculations

Table D.1 lists the aircraft mass and nominal CG position in the wing coordinate system. The  $z$  position of the wing MAC is used as the  $z$  position of the CG.

Table D.1: Aircraft weight and balance parameters

<b>Symbol</b>	<b>Description</b>	<b>Nominal value</b>
$m_{land}$	Design maximum landing weight	6895 kg
$x_{cg}$	nominal x position of the CG	21.5% $\bar{c} = -0.347\ m$
$y_{cg}$	nominal y position of the CG	0.0 m
$z_{cg}$	nominal z position of the CG	0.258 m

## APPENDIX E Aerodynamics

The aerodynamics are given by Tuzcu, (2001) in discretized form. They were recombined to yield aerodynamic coefficients for the whole aircraft using Equations (E.1a) to (E.1f).

$$C_L = C_{L_{h fus}} + C_{L_{wing}} + C_{L_{htail}} + C_{L_{engine}} + C_{L_{elevator}} \quad (E.1a)$$

$$C_D = C_{D_{h fus}} + C_{D_{wing}} + C_{D_{htail}} + C_{D_{engine}} + C_{D_{elevator}} + C_{D_{v fus}} + C_{D_{vtail}} + C_{D_{rudder}} \quad (E.1b)$$

$$C_m = C_{m_{h fus}} + C_{m_{wing}} + C_{m_{htail}} + C_{m_{engine}} + C_{m_{elevator}} \quad (E.1c)$$

$$C_Y = C_{Y_{v fus}} + C_{Y_{vtail}} + C_{Y_{rudder}} \quad (E.1d)$$

$$C_\ell = C_{\ell_{v fus}} + C_{\ell_{vtail}} + C_{\ell_{aileron}} + C_{\ell_{rudder}} \quad (E.1e)$$

$$C_n = C_{n_{v fus}} + C_{n_{vtail}} + C_{n_{aileron}} + C_{n_{rudder}} \quad (E.1f)$$

### E.1 Longitudinal Aerodynamics

Figure E.1 shows the geometry involved in the calculation of the longitudinal aerodynamic coefficients.

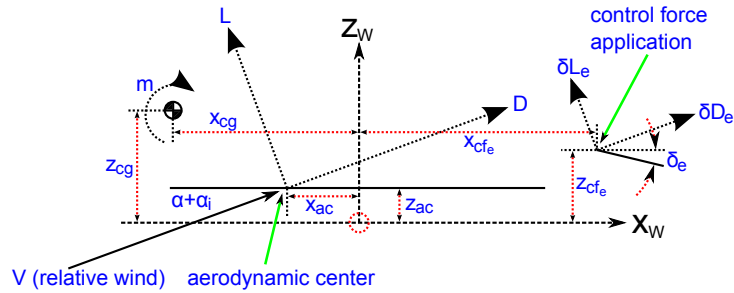


Figure E.1: Aircraft geometry (side view) used for calculation of the aircraft longitudinal aerodynamic coefficients

The lift coefficient of each horizontal lifting surface  $s$  was calculated as follows:

$$C_{L_s} = \frac{1}{S_w} \left[ \sum_s S_p C_{L_{\alpha_p}} (\alpha + \alpha_{ip}) \right] \quad (\text{E.2})$$

where the summation is over all panels making up the lifting surface,  $S_p$  is the area of each individual panel,  $C_{L_{\alpha_p}}$  is the panel lift curve slope,  $\alpha_{ip}$  is the panel angle of incidence and  $S_{ref}$  is the wing reference area.

The change in lift coefficient due to deflection of horizontal control surface  $c$  was calculated as follows:

$$\delta C_{L_c} = \frac{1}{S_w} \left[ \sum_c S_p C_{L_{\delta_p}} \delta \right] \quad (\text{E.3})$$

where the summation is over all the panels making up the control surface,  $S_p$  is the area of the whole panel and not just the control surface part of the panel and  $C_{L_{\delta_p}}$  is the change in lift coefficient as a function of control surface deflection  $\delta$ .

The drag coefficient of each lifting surface  $s$  was calculated as follows:

$$C_{D_s} = C_{D_{0s}} + C_{L_{is}} = C_{D_{0s}} + k C_{L_s}^2 \quad (\text{E.4})$$

where  $C_L$  is replaced with  $C_Y$  for the case of vertical lifting surfaces,  $C_{D_{0s}} = 0.016$  and  $k = 0.04$  (Tuzcu, 2001).

The change in drag coefficient due to deflection of control surface  $c$  was calculated as follows:

$$\delta C_{D_c} = \delta C_{L_{ic}} = k \delta C_{L_c}^2 \quad (\text{E.5})$$

where  $C_L$  is replaced with  $C_Y$  for the case of vertical control surfaces.

The pitching moment coefficient of each horizontal lifting surface  $s$  was calculated as follows:

$$C_{m_s} = \frac{1}{\bar{c}_w} [(C_{L_s} \cos \alpha + C_{D_s} \sin \alpha)(x_{cg} - x_{ac_s}) + (C_{L_s} \sin \alpha - C_{D_s} \cos \alpha)(z_{cg} - z_{ac_s})] \quad (\text{E.6})$$

where  $x_{cg}$  and  $z_{cg}$  are the centre of gravity coordinates,  $x_{ac_s}$  and  $z_{ac_s}$  correspond to the x (0.25%  $\bar{c}$ ) and z coordinates of the surface mean aerodynamic center respectively.

The change in pitching moment coefficient due to deflection of horizontal control surface  $c$  was calculated as follows:

$$\delta C_{m_c} = \frac{1}{\bar{c}_w} [(\delta C_{L_c} \cos \alpha + \delta C_{D_c} \sin \alpha)(x_{cg} - x_{cf_c}) + (\delta C_{L_c} \sin \alpha - \delta C_{D_c} \cos \alpha)(z_{cg} - z_{cf_c})] \quad (\text{E.7})$$

where  $x_{cf_c}$  and  $z_{cf_c}$  correspond to the mean x (0.55%  $\bar{c}$ ) and z coordinates of the control force application point respectively.



## E.2 Lateral Aerodynamics

Figures E.2 and E.3 show the geometry involved in the calculation of the lateral aerodynamic coefficients.

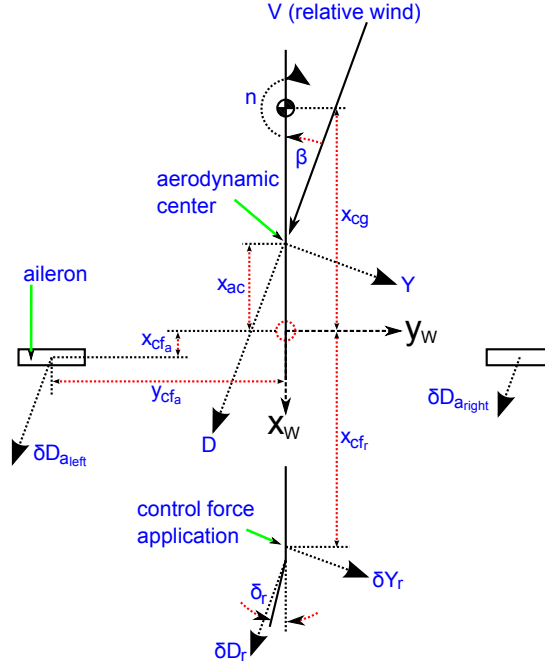


Figure E.2: Aircraft geometry (top view) used for calculation of the aircraft lateral aerodynamic coefficients

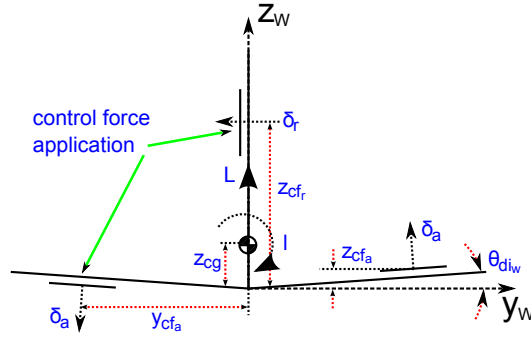


Figure E.3: Aircraft geometry (front view) used for calculation of the aircraft lateral aerodynamic coefficients

The side force coefficient of each vertical lifting surface  $s$  was calculated as follows:

$$C_{Y_s} = \frac{1}{S_w} \left[ \sum_s S_p C_{Y_{\beta_p}} \beta \right] \quad (\text{E.8})$$

where  $C_{Y_{\beta_p}}$  is the panel side force curve slope.

The change in side force coefficient due to deflection of vertical control surface  $c$  was calculated as follows:

$$\delta C_{Y_c} = \frac{1}{S_w} \left[ \sum_c S_p C_{Y_{\delta_p}} \delta \right] \quad (\text{E.9})$$

where  $C_{Y_{\delta_p}}$  is the change in lift coefficient as a function of control surface deflection  $\delta$ .

The rolling moment coefficient of each vertical lifting surface was calculated as follows:

$$C_{\ell_s} = \frac{1}{b_w} [C_{Y_s} \cos \beta - C_{D_s} \sin \beta] (z_{acs} - z_{cg}) \quad (\text{E.10})$$

The change in rolling moment coefficient due to asymmetrical deflection of horizontal control surface  $c$  was calculated as follows:

$$\delta C_{\ell_c} = -\frac{1}{b_w} [\delta C_{L_c} \cos \alpha + \delta C_{D_c} \sin \alpha] (2y_{cf_c}) \quad (\text{E.11})$$

The change in rolling moment coefficient due to deflection of vertical control surface  $c$  was calculated as follows:

$$\delta C_{\ell_c} = \frac{1}{b_w} [\delta C_{Y_c} \cos \beta - \delta C_{D_c} \sin \beta] (z_{cf_s} - z_{cg}) \quad (\text{E.12})$$

The yawing moment coefficient of each vertical lifting surface  $s$  was calculated as follows:

$$C_{n_s} = \frac{1}{b_w} [C_{Y_s} \cos \beta - C_{D_s} \sin \beta] (x_{cg} - x_{acs}) \quad (\text{E.13})$$

The change in yawing moment coefficient due to asymmetrical deflection of horizontal control surface  $c$  was calculated as follows:

$$\delta C_{n_c} = -\frac{1}{b_w} [\delta C_{L_c} \sin \alpha - \delta C_{D_c} \cos \alpha] (2y_{cf_c}) \quad (\text{E.14})$$

The change in yawing moment coefficient due to deflection of vertical control surface  $c$  was calculated as follows:

$$\delta C_{n_c} = \frac{1}{b_w} [\delta C_{Y_c} \cos \beta - \delta C_{D_c} \sin \beta] (x_{cg} - x_{cf_c}) \quad (\text{E.15})$$

## APPENDIX F The RCAM Problem

The RCAM problem defines a mission consisting of the typical approach and landing path illustrated in Figure F.1 (FM(AG08), 1997b) where the coordinates of each segment are listed in Table F.1.

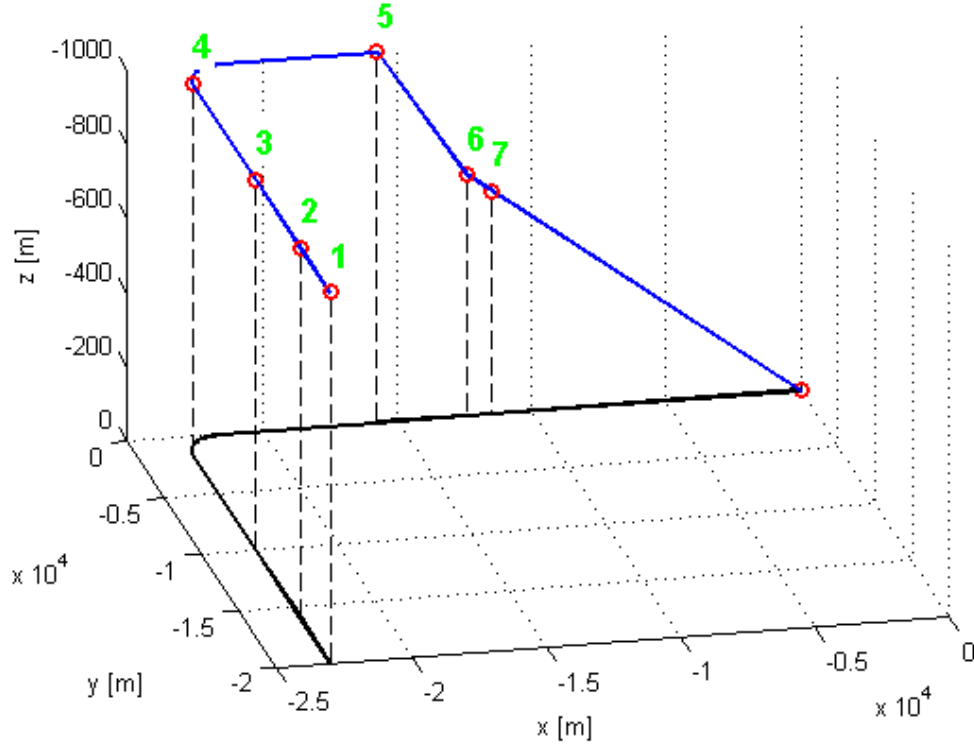


Figure F.1: RCAM approach and landing trajectory

Data from the Citation V Flight Manual (Cessna Aircraft Company, 1988) was obtained for the aircraft in order to determine the speed at which each segment is flown. The aircraft configuration is maximum landing weight, flaps and gear up.

1. Start at point 1 in straight and level flight at an altitude of 1000 m with a track angle of  $\chi = -90^\circ$  and an airspeed of  $V_{APP} = 58 \text{ m/s}$  (with flaps up

Table F.1: Definition of the RCAM trajectory segments

Segment	$x^E$ [m]	$y^E$ [m]	$z^E$ [m]	Description
1	-23000	-20000	-1000	straight and level
2	-23000	-16000	-1000	straight and level, stop port engine
3	-23000	-10000	-1000	straight and level, restart port engine
4	-23000	-1500	-1000	coordinated turn
5	-15734	0	-1000	straight decent with glide slope of $6^\circ$
6	-12404	0	-650	straight decent with glide slope of $3^\circ$
7	-11450	0	-600	straight decent with glide slope of $3^\circ$
8	0	0	-30	flare

and gear up).

2. Investigate the effect of a failed engine by reducing the throttle of the left engine (engine 1) to idle at point 2. The dynamics of the engine are given by the first order transfer function  $G_e(s) = \frac{1}{1+3.3s}$ .
3. Investigate the effect of an in flight engine restart by restarting the failed engine at point 3 (restore the throttle to the same setting as engine 2).
4. Commence a coordinated turn at point 4 with a heading rate of change of  $\dot{\psi} = 3^\circ/s$  while maintaining  $V_{APP} = 58 \text{ m/s}$ , maintaining a bank angle of  $\phi = 30^\circ$  and minimizing lateral acceleration.
5. Commence a descent at point 5 with a glide slope of  $\gamma = 6^\circ$  while maintaining  $V_{APP} = 58 \text{ m/s}$ .
6. At point 6 reduce the glide slope to  $\gamma = 3^\circ$  and reduce the airspeed to  $V_{REF} = 55 \text{ m/s}$  (with flaps down and gear down).
7. Investigate the effect of wind shear by applying it at point 7. The aircraft should not deviate too far from the commanded glide slope and should maintain  $V_{REF} = 55 \text{ m/s}$ .
8. The simulation finishes when the aircraft flares at an altitude 30m above the runway in preparation for touchdown.

## APPENDIX G Longitudinal Results

Figures G.1, G.2 and G.3 show the longitudinal aerodynamic coefficients  $C_L$ ,  $C_{D_i}$  and  $C_m$  respectively as a function of the maximum airfoil camber at the wing tip.

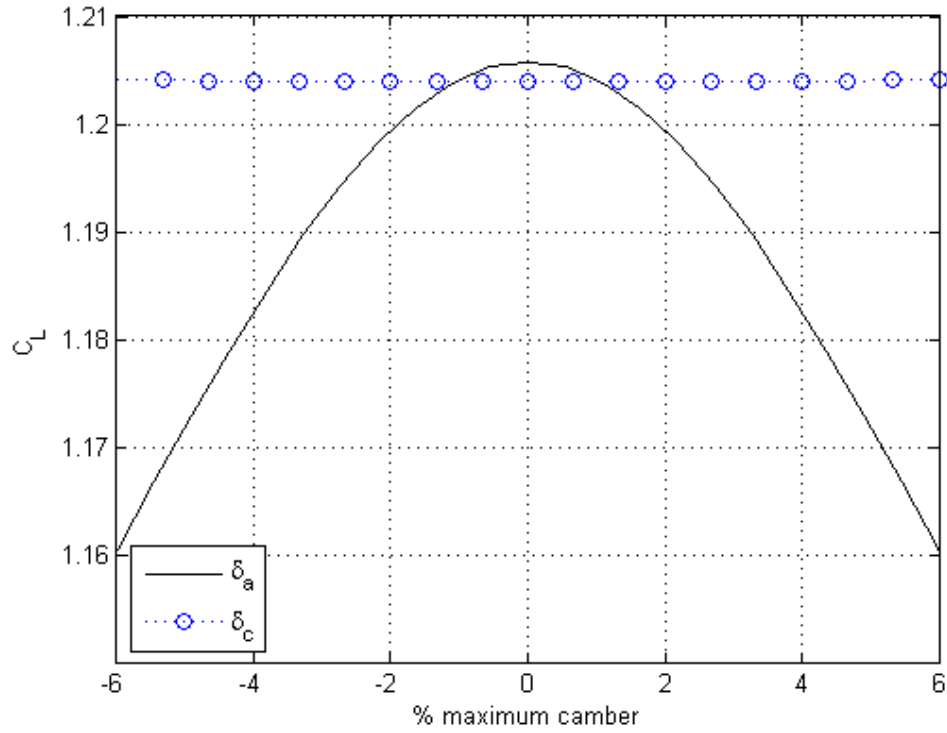


Figure G.1: Comparison between the effects of aileron deflection and variable camber actuation on the aircraft lift coefficient  $C_L$

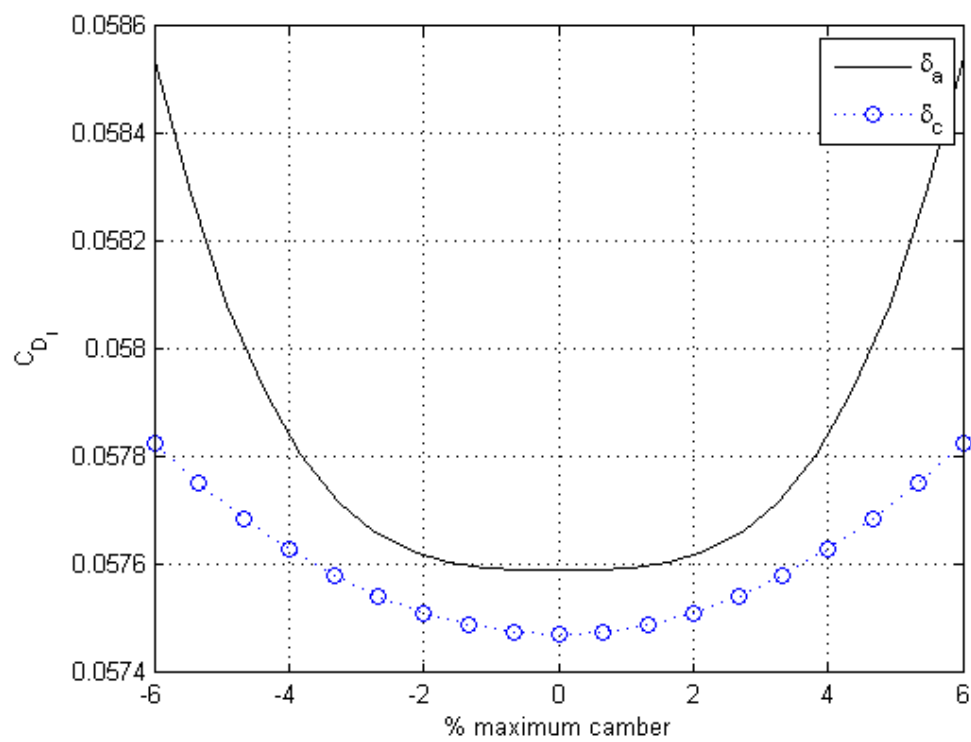


Figure G.2: Comparison between the effects of aileron deflection and variable camber actuation on the aircraft induced drag coefficient  $C_{D_i}$

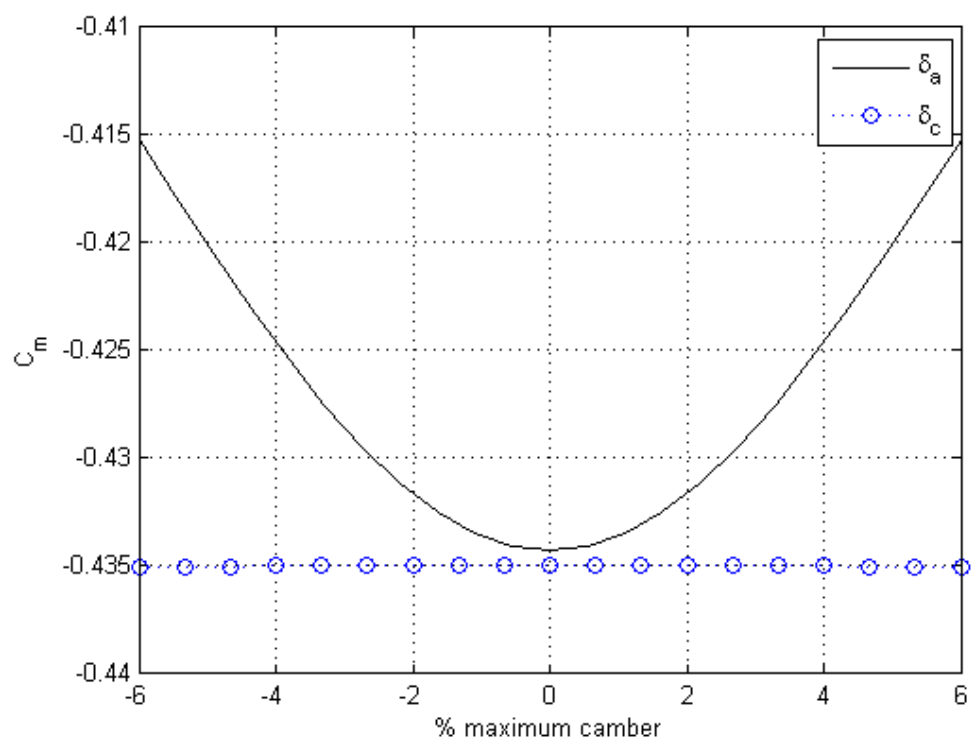


Figure G.3: Comparison between the effects of aileron deflection and variable camber actuation on the aircraft pitching moment coefficient  $C_m$